Measurement of the Cosmic Ray Energy Spectrum between 500 TeV and 100 PeV with IceTop

Abd Al Karim Haj Ismail

Gent University

Academic Year 2014 - 2015

UNIVERSITEIT GENT

Measurement of the Cosmic Ray Energy Spectrum between 500 TeV and 100 PeV with IceTop

Abd Al Karim Haj Ismail

Supervisor: Prof. Dirk Ryckbosch

Thesis submitted to obtain the academic degree of Doctor of Science: Physics

Department of Physics and Astronomy, Faculty of Science

Gent University

Academic Year 2014 - 2015

Members of the examination committee:

Prof. Dirk Ryckbosch (UGent)

Prof. Nick Van Eijndhoven (VUB)

Dr. Serap Tilav (University of Delaware - USA)

Prof. Sven De Rijcke (UGent)

Prof. Philippe Smet (UGent)

Prof. Jan Ryckebusch (UGent)

Dr. Athina Meli (UGent)

In Memory of My Father

Acknowledgment

The completion of this PhD is the most challenging activity in my life. Numerous people, over the last couple of years, have helped and supported me towards the end of this long journey. So; It is time to look back and thank all of them:

I would like to express my deepest thanks to my supervisor Prof. Dirk Ryckbosch for giving me the opportunity to work in a big international collaboration, The IceCube Neutrino Observatory. Thank you Dirk, It has been an honor to be in your group. I appreciate all your encouragement, trust, ideas and the big effort to make this PhD possible.

I would like to thank all members of the Department of Physics and Astronomy. I enjoyed working with all of you. Special thanks for my colleagues in the IceCube group in Gent (Tom, Sam, Mathieu, Matthias, Sander, Ola and Athina) you were part of the story, thank you all.

I would like to thank my office mates Arne, Tom, Sam and Igor for all the discussion and help. I hope you enjoyed my presence in the office, at least I did. Special thanks goes to Tom Feusels for his patient, the long discussion and the enormous help since the beginning of my work. Also, Special thanks goes to Sam De Ridder for reading the very first draft of this thesis, and the daily discussion.

I would like to thank my colleagues in the cosmic ray group and all members of the IceCube collaboration for the great discussion during all collaboration meetings and phone calls.

I would like to thank all members of the exam committee for their guidance, reading and suggestions to improve this thesis.

إِلَى أصدقَائِي و عَائِلتِي:

بدَاية الحمد لِله الَذي بحمده تَتم النعم فلولَا توفيقه عز وجل لمَا استطعت أن أحصل علَى هذه الدرجة.
أود أن أتقدم بخَالص الشكر إِلَى جمِيع أصدقَائِي الذِين كَانوَا خير السند وَالصدِيق فِي غربتِي. و أخص بِالذكر: طرَاد جوَيد، محمد حمشو و محمد الشِهَاب الذِين وقفوَا إِلَى جَانبِي ودعمونِي منذ البدَاِية. لَا يسعنِي ذكر الجمِيع هنَا لأَن الأَسمَاء كثِيرة ولكن لكُم مِنّي جمِيعًا كُلُّ محبة وتقدِير.

أود أن أتقدم بخَالص الشكر إِلَى وَالدِي الغَالِي (أحمد رحمه اللّه) الذِي طَالمَا حلم أن يرَانِي أحصل علَى هذه الدرجة ولكن قدر اللّه ومَا شَاء فعل. الشكر موصول إِلَى وَالدتِي الغَالِية (مريم) التِي تحملت الفرَاق لسنِين. أمي وأَبِي: لقد كنتم رمزَا لِلعطَاء وَالتضحية، اللَهم اغفر لهمَا وَارحمهمَا كمَا ربيَانِي صغيرًا. كمَا أَنَني لَا أنسَى إِخوتِي الأَعزَاء (محمد، مصطفَى، خَالد ودلّة) علَى كل الدعم وَالتقدِير. أسأَل اللَه أن يحقِق آمَالكم لمَا يحبه ويرضَاه. كمَا و أشكر عمر وزوجته صلوح لكونهم من العَائِلة وتحملهم قدرَاً من المسؤُولية.

أود أن أتقدم بخَالص الشكر إِلَى زوجتِي ورفيقة دربِي الغَالِية شمسة و أولَادِي الأَحبَاء (أسمَاء - أَحمد - أَسيل - حنَان)، أنتم كُل حيَاتِي، أود أن أشكركم علَى محبتكم وصبركم وعلَى كل الدعم و الحب الذِي قدمتموه لِي. أتمنَى أن تسَامحونِي لَانشغَالِي الدَائِم عَنكم خلَال فترة درَاستِي كمَا و أتمنَى أن أستطِيع تعوِيضكم عن ذلك فِي المستقبل.

عبد الكريم حَاج اسمَاعيل

Contents

Introduction

Cosmic rays are very energetic charged particles originate in the outer space, travel at nearly the speed of light and strike the Earth from all directions. The main constituents of cosmic rays are the nuclei of atoms. They also include high energy electrons, positrons, and other subatomic particles. They have first been discovered in 1912 by the Austrian physicist Victor Hess. Although their discovery was more than a century ago, a lot of fundamental questions about their origin, propagation and acceleration mechanisms in the universe are not answered yet.

Measurements of the cosmic ray energy spectrum from different cosmic ray experiments showed that it follows a power law with some features. Although we do not have a perfect interpretation of what causes these breaks in the energy spectrum, they may indicate a transition in the composition and provide informations about the production processes and possible sources of these particles. A first change in the spectrum is observed around 4×10^{15} eV, generally called the knee. The knee structure can be explained, in current measurements of the energy spectrum and composition, as a rigidity dependent leakage of cosmic rays from the Galaxy. Another feature called the ankle occurs at around 3×10^{18} eV, where the contribution of extragalactic cosmic particles dominates in this part of the spectrum. A strong suppression in the energy spectrum is observed at energies above 6×10^{19} eV. This effect is called the GZK cutoff. At energies higher than the GZK cutoff, cosmic ray particles lose energy through the interaction with the cosmic ray microwave background.

Cosmic rays are a sample of solar, galactic and extragalactic matter. Solar cosmic particles originate from the sun during solar flares with energies below 10^{10} eV. However, low energy cosmic rays have a strong anti-correlation with solar activity. Up to 4×10^{15} eV (the knee), cosmic rays are certainly from a Galactic origin (e.g. Active Galactic Nuclei) while their origin is assumed to be extra galactic (e.g. Active Galactic Nuclei) for energies higher than 3×10^{18} eV (the ankle). The energy range between the knee and the ankle is not well understood. However, cosmic rays are thought to be originating in our Galaxy.

Primary cosmic particles with energies below 10^{14} eV can be directly measured with satellite and balloon experiments above the atmosphere. However, for energies above 10^{14} eV, the intensity decreases steeply with energy, and very large arrays are needed to detect them. When a high energy primary cosmic ray enters the Earths atmosphere, it interacts with the air molecules and creates a cascade of charged particles called ”Extensive Air Showers, EAS. Therefore, cosmic rays with energies beyond 10^{14} eV can only be studied indirectly by detecting extensive air showers on the earths surface with ground based air shower particle detectors.

The goal of the analysis, presented in this thesis, is to measure the cosmic ray energy spectrum in the energy range between 500 TeV and 100 PeV, using data from the IceTop detector. IceTop, the surface component of the IceCube Neutrino Observatory, is a square kilometer air shower array at the geographic South Pole. IceTop uses ice tanks to detect Cherenkov light produced by secondary cosmic ray particles.

In Chapter 1, a short overview about cosmic rays, extensive air showers and related questions about the origin, propagation and acceleration of cosmic rays in the universe, is introduced. The IceCube and IceTop detectors are presented in Chapter 2. In Chapter 3, the Monte Carlo simulation of extensive air showers is explained. In Chapter 4, a reconstruction procedure for the measured data and the simulation is applied in order to extract the basic quantities of the detected air shower.

In Chapter 5, the event selection process is introduced and the analysis method to reconstruct the primary energy from the shower size is described. The measured energy spectrum in this thesis is presented in Chapter 6. Finally, the results are discussed and compared to spectra from other cosmic ray experiments, in Chapter 7.

Chapter 1

Cosmic Rays

In 1912, Victor Hess discovered the cosmic radiation by measuring the discharging effect of electroscopes during some balloon flights. Since their discovery more than 100 years ago, cosmic rays have been studied by many experiments with different detection methods to explore their properties and origin. However, several questions about the sources, propagation in the universe and the acceleration mechanism are still not fully answered.

In this chapter, a general overview of the observed properties of cosmic rays and the theoretical models that explain their origin and acceleration mechanisms will be introduced.

1.1 The First Century

At the end of the 19^{th} century, physicists found that electroscopes can be discharged even when they are kept in dark and in the absence of radioactive sources. Scientists tried to apply different ideas to discover and understand the origin of the ionizing radiation.

C.T.R. Wilson took his electroscope underground into a dark location, a railway tunnel, and he observed no falloff in the radiation rate [1]. It was later shown by Rutherford that most of the radiation is due to natural radioactivity, either from rocks or contamination of the electroscope.

In 1910, Wulf took an electroscope up the Eiffel Tower and observed a decrease in the ionization rate. If the radiation is originating at the surface of the earth, this radiation should be negligible at the top of the Eiffel Tower. The observed radiation decrease was however much less than theoretical expectations. Wulf concluded that the radioactivity of the air must contribute to the measured ionization [1].

Figure 1.1: V. Hess after one of his successful balloon flights in which he observed an ionization increase with altitude [1].

The big breakthrough came in 1912 by Victor Hess in a series of high altitude balloon flights up to 5 km in the atmosphere. He found that the radiation increased with altitude indicating that the source of the radiation must be above the atmosphere of the earth. This experiment was confirmed by Werner Kolhorster in 1914 with an improved electroscope reaching an altitude of 9 km. The radiation increase was a clear evidence that the high energy radiation has an extraterrestrial origin (Figure 1.2).

Hess made the immediate inference:

"The results of the present observations seem to be most readily explained by the assumption that a radiation of very high penetrating power enters our atmosphere from above, and still produces in the lower layers a part of the ionization observed in closed vessels" [1].

A few years later, in 1936, Hess was awarded the Nobel Prize in physics for this discovery of cosmic rays.

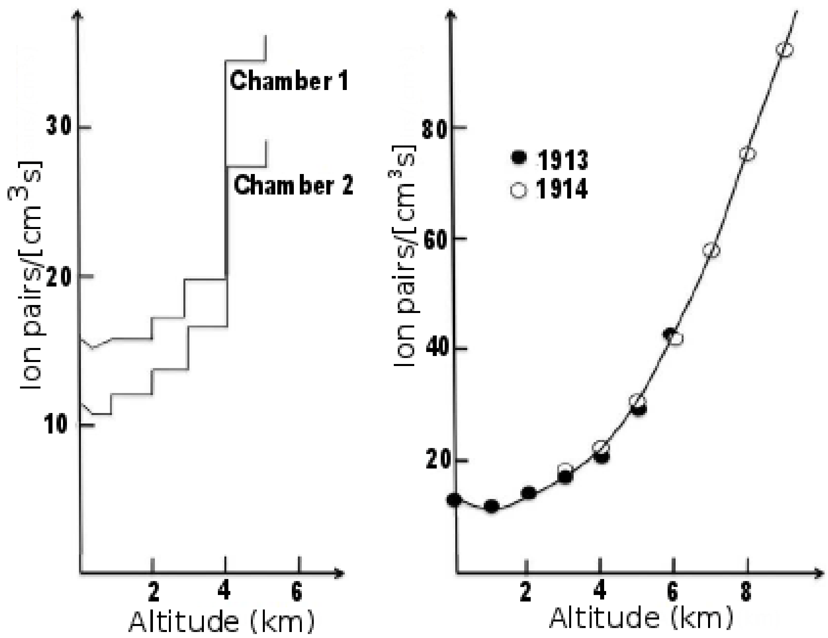

Figure 1.2: The increase of ionization with altitude measured in a series of balloon flights by V. Hess (left) and M. Kolhorster (right).

In 1939, Pierre Auger discovered Extensive Air Showers (EAS). Using Geiger counters separated by a large distance (about 300 m), Auger observed about 10^6 particles covering approximately 10^4 m^2 area, which he deduced to be produced from successive interactions of a single primary cosmic ray in the top of the atmosphere. Auger estimated that the energy of the primary cosmic ray particle was about 10^{15} eV [2].

1.2 Cosmic Ray Physics

1.2.1 Energy Spectrum

Since the discovery of cosmic rays, their energy spectrum has been measured by a variety of cosmic ray experiments. Direct cosmic ray measurements with satellite and balloon experiments reached an energy of $\sim 10^{15}$ eV and they are limited by the detector size and exposure time. Such experiments can directly identify incident particles with excellent charge resolution [3]. Due ti the very low cosmic ray flux at higher energies, the the energy spectrum can not be measured directly. Instead, ground based experiments are used to deduce the energy of the cosmic ray primary from the properties of the detected secondary particles. The ground based experiments use the atmosphere above them as a detection medium. Therefore, the detection area can be increased considerably compared to satellite and balloon experiments.

The energy spectrum can be described by:

$$\frac{\mathrm{d}\,N}{\mathrm{d}\,E} \propto E^{-\gamma}, \qquad \text{with } \gamma = \begin{cases} \gamma \approx 2.7, & E < 4 \text{ PeV} \\ \gamma \approx 3, & 4 \text{ PeV} < \ E < \ 3 \text{ EeV} \\ \gamma \approx 2.6, & E > \ 3 \text{ EeV} \end{cases} \tag{1.1}$$

with γ the spectral index.

The observed energy spectrum approximately follows a power law over many orders of magnitude in energy and with several features (Figure 1.3). The observed spectral features are crucial for understanding the origin of particles, their propagation and acceleration mechanisms.

The knee

The first of these features occurs at an energy around 4 PeV where the spectral index changes from 2.7 to 3.0. This feature is called the ”knee” and was discovered in 1958 [4]. Since then, many models

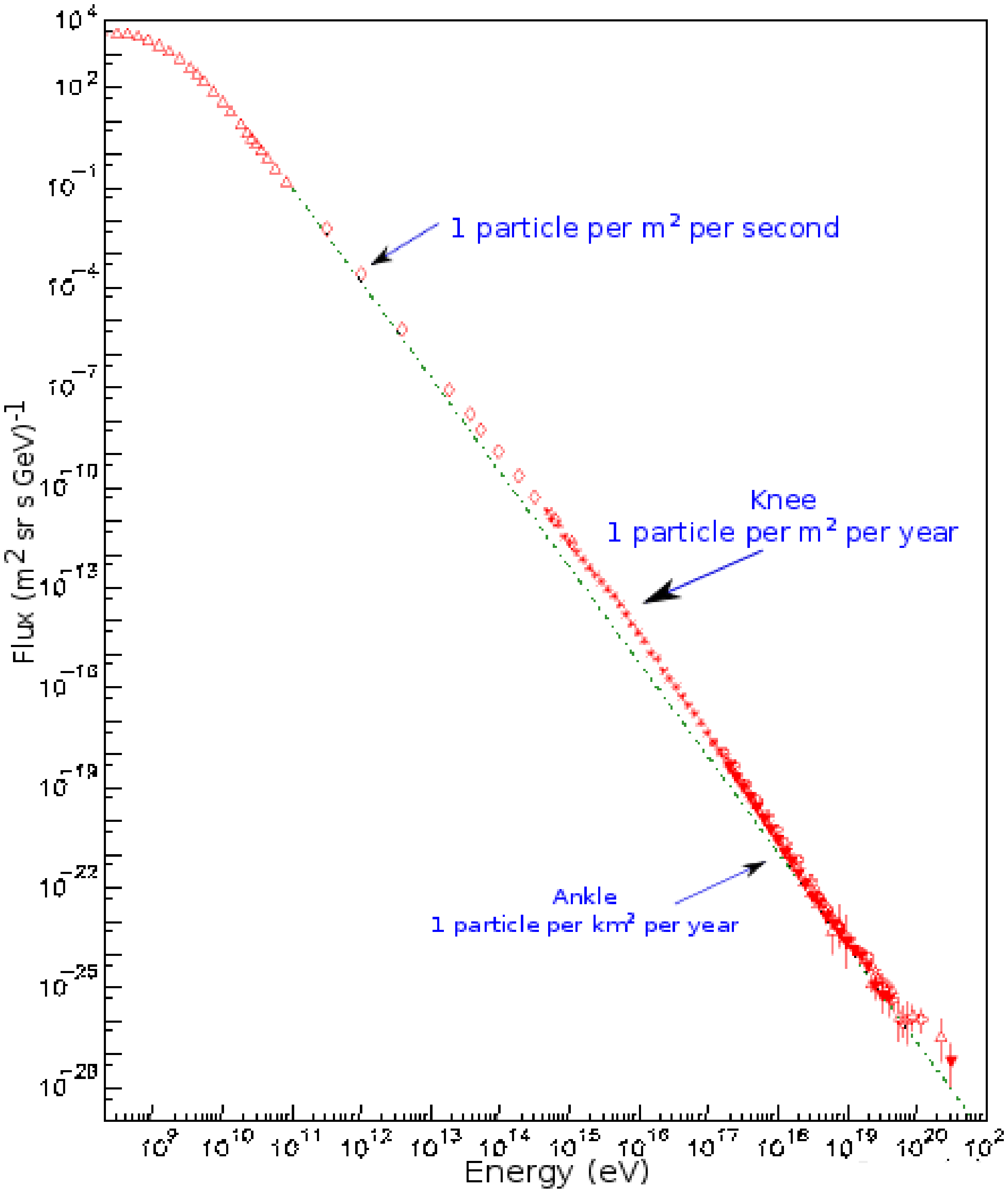

Figure 1.3: The flux of cosmic rays as a function of energy. The dashed line shows a E^{-3} spectrum.

tried to explain the knee structure in different ways. However, there is still no perfect understanding for the reason of this feature.

The diffusive shock acceleration model explains the knee as an effect of the underlying acceleration mechanisms. Cosmic rays are accelerated in the blast waves of the supernova remnant and a rigidity dependent limit is predicted. Therefore, the maximum achievable energy depends on the the charge Z of the cosmic particle ($E = [Z \times 10^{14}$ eV - $Z \times 10^{15}$ eV]). Consequently, the position of the knee depends on the type of the comic particle. This results in various cutoffs in the spectrum while the composition would become heavier [5].

In an alternative explanation, the knee is connected with the leakage of cosmic rays from the Galaxy (called the leaky box model, discussed in Section 1.2.5). This model combines the diffusive shock acceleration with an energy propagation path length. The position of the knee for different elements is proportional to the charge Z of the cosmic particle [5].

The knee is considered in some other theoretical models to be originating from the interactions of cosmic rays with background particles in the Galaxy, or to be related to the shower development in the atmosphere assuming that a new type of interactions transfers energy to a new component that is not yet observed in air shower experiments [6].

At an energy of about 400 PeV, the spectral index changes from $\sim$ 3.0 to $\sim$ 3.3. This feature is called the ”second knee”, and was suggested by some air shower experiments (HiRes-MIA [7], Haverah Park Array [8] and Yakutsk [9]). However, the ”second knee” was not seen by other experiments (AGASA [10] - Akeno [11]).

The ankle

Another feature in the energy spectrum is called the ”ankle”, first observed by the Volcano Ranch experiment [12]. This happens at energy about 3 EeV where the spectral index changes from $\sim$ 3 to

$\sim$ 2.6. There are three theoretical models to describe the origin of the ankle: the ankle model, the dip model and the mixed composition model. They differ from each other by the energy transition from galactic to extragalactic cosmic rays, and the mass composition of the extragalactic component.

The ankle model assumes that the transition from galactic to extra galactic occurs at E$_{tra}$ $\sim$ $(3-10)$ EeV. The transition, based on this model, is described as the intersection between a flat ($\propto$ E^{-2}) extragalactic spectrum and a steep ($\propto$ E$^{-3.1}$) Galactic one. The composition in the Galactic component is represented by heavy nuclei (iron), while the extragalactic component is assumed to be pure proton. the model is in contradiction with results of X_{max} measurements with both HiRes and Auger in the energy range (1 - 5) PeV [13] (Figure 1.4).

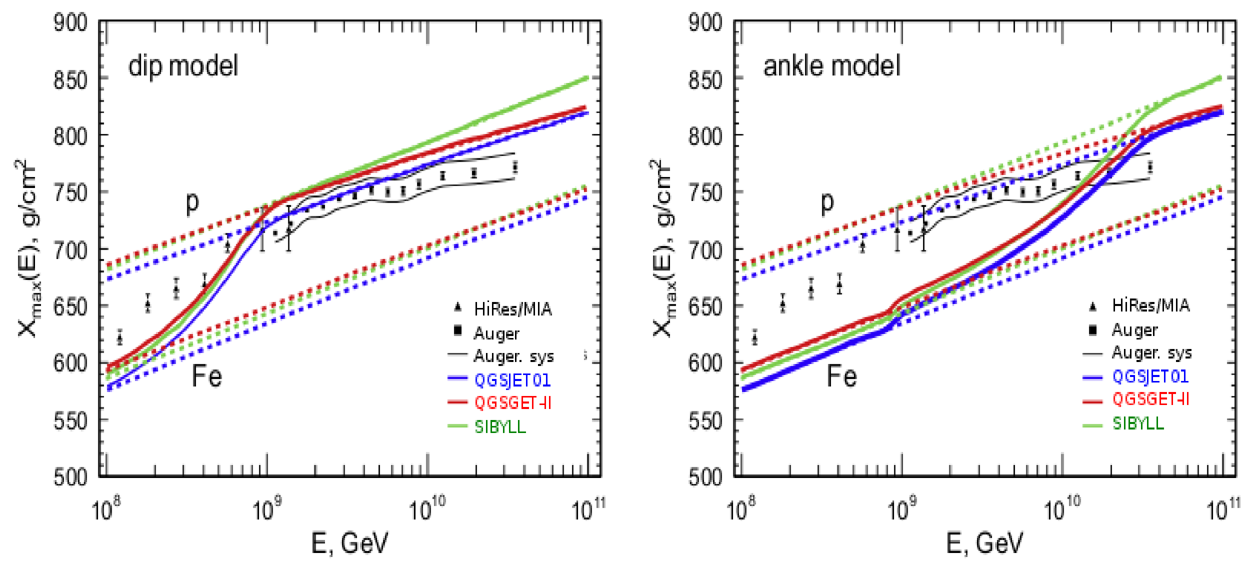

Figure 1.4: The calculated X_{max} as a function of energy for the dip model (left) and ankle model (right). The data points are measurements from the HiRes and Pierre Auger Observatory [14].

In the dip model, the transition occurs as an intersection between a very flat extragalactic spectrum and a steep Galactic iron spectrum. The dip model predicts a pure proton composition above E $\geq$ 1 EeV. This model is in agreement with the HiRes measurements where a strong proton dominance is observed at E $>$ 1EeV, while the model does not agree with Auger measurements of X_{max} and RMS at E $>$ 4 EeV (Figure [13] 1.4).

The mixed composition model is based on the argument that any acceleration mechanism involves different nuclei in the acceleration process. Therefore, it assumes that the Galactic component of cosmic rays above 0.1 EeV is a pure iron while the composition in the extragalactic component has nuclei of various types. However, proton is considered in most mixed composition models to be dominant at the highest energies E $\geq$ 10 EeV. This assumption is in contradiction with Auger measurement at these energies [13].

The GZK mechanism

At high energies E $>10^{19}$ eV, a strong suppression in the flux was independently predicted in 1966 by Greisen [15] and Zatsepin and Kuzmin [16] and called the GZK cutoff. This prediction was based on the assumption that the composition of the extragalactic component of the spectrum is pure proton which interact with the cosmic microwave background photons (CMB) via photo-pion production.

The dominant interactions of protons with the CMB are:

$$
\begin{aligned}
p + \gamma_{CMB} &\rightarrow \Delta^+ \rightarrow n + \pi^+ \\
p + \gamma_{CMB} &\rightarrow \Delta^+ \rightarrow p + \pi^0,
\end{aligned}
\tag{1.2}
$$

Measurements by the AGASA experiment [10] showed no decrease in the energy spectrum for energies above 10^{20} eV indicating no GZK-cutoff. However, the results from HiRes [17] showed a cutoff in the flux at the predicted cutoff energy. This was also supported by the results from the Auger collaboration [18].

1.2.2 Composition

Understanding the chemical composition of cosmic rays is important to reveal their origin and their acceleration mechanism. Below 10^{14} eV, Cosmic rays consist mainly of $\sim$ 86% hydrogen nuclei, $\sim$ 11% helium, $\sim$ 2% heavier nuclei and $\sim$ 1% electrons [19].

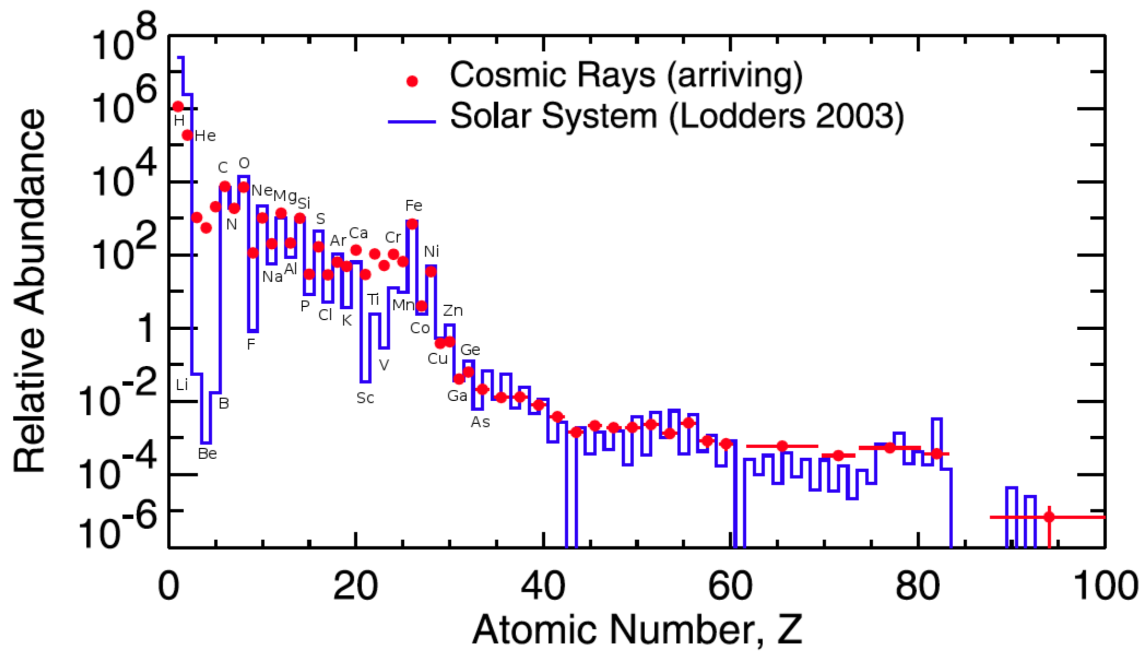

Figure 1.5: The relative chemical abundance of elements in the Galactic cosmic rays (red circles) compared to the abundance of the solar system matter (blue histogram). Data points for H and He are obtained with the BESS balloon experiment [20]. For $3 \geq Z \geq 30$, the data points are from the Cosmic Ray Isotope Spectrometer (CRIS) measurements [21]. For elements with $Z > 30$, results are from the HEAO-C3 and Ariel-VI experiments with a normalization to make them agree with the Fe abundance [22]. Plot is edited from [23].

For energies up to 10^{14} eV, the chemical composition is measured precisely by balloon and satellite experiments. Figure 1.5 shows a comparison between the abundances of elements in Galactic cosmic rays and the solar system abundance. A general similarity of the elemental composition is observed for the elements H, He, C, O, Ne, Mg, Si and Fe dominating both samples. Elements with an even-Z have a predominance over elements with an odd-Z in the range Z=[6-20]. In addition, several peaks are observed in the distribution, $6 \leq Z \leq 8$ (CNO), $Z \simeq 26$ (Fe), $50 \leq Z \leq 56$ (Sn - Ba), and $78 \leq Z \leq 82$ (Pt - Pb). The overabundance of cosmic rays below these peaks is due to the nuclear spallation reactions during the propagation of cosmic rays through the interstellar gas.

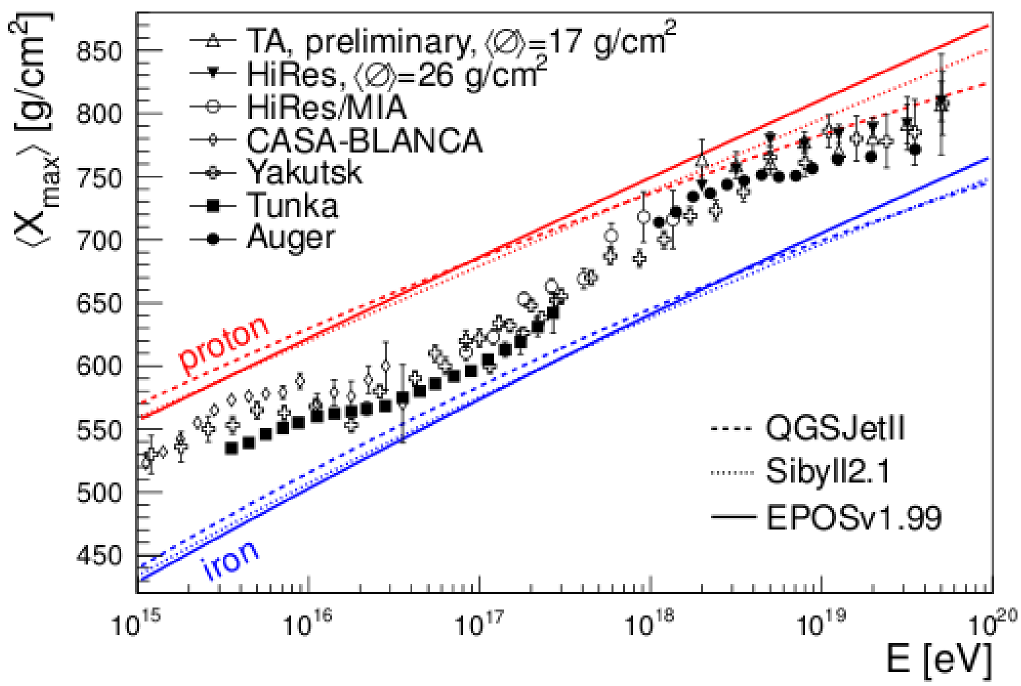

Figure 1.6: Measurements of the shower maximum X_{max} as a function of energy for energies from different EAS experiments. Simulation of proton and iron primaries for different hadronic interaction models are shown in red and blue, respectively [24].

For higher energies, indirect air shower experiments are used to study the properties of the secondary particles and to deduce the primary type and energy of the primary cosmic ray. These measurements rely on the composition sensitivity of EAS observables to the primary cosmic particle (expressed often by the shower maximum X_{max} or the mean logarithmic mass $< \ln A >$). Figure 1.6 shows a comparison of the $< X_{max} >$ as a function of primary energy from different air shower experiments. Up to 10^{17} eV, the measurements indicate a change in the mass towards heavier composition. At higher energies, the absolute values of $< X_{max} >$ increases again towards the prediction of light composition.

1.2.3 Sources

Cosmic rays, as charged particles, are deflected by the magnetic field of the Galaxy and the sun. Therefore, they are uniformly distributed in all directions and do not point back to their origins. Once the gyroradius R_L of a particle exceeds the size of the accelerator, the particle is not contained anymore and will be able to escape from the acceleration region and it is unable to gain more energy. This Hillas criterion [25] sets the limit for the maximum energy:

$$\varepsilon_{max} = qBR, \tag{1.3}$$

where ε is the gained energy, q is the electric charge of the particle, B is the magnetic field and R is the size of the source.

Figure 1.7 is known as the Hillas diagram and shows the relation between the magnetic field of the source B and its size R with various astrophysical sources are plotted. Sources above the upper line can produce protons with energies up to 10^{20} eV, while sources above the bottom line are able to produce iron with energies up to 10^{20} eV. Most astrophysical sources do not reach the the iron confinement, leaving the best candidates for ultra high energy cosmic rays (UHECRs, energy above 10^{18} eV) to Active Galactic Nuclei (AGN), Gamma Ray Bursts (GRBs) and neutron stars.

The observed structures in the cosmic ray energy spectrum may provide valuable information to distinguish between cosmic ray sources. Cosmic rays with energies below 3^{15} (the knee) eV are thought to be originating in our Galaxy. For energies beyond 3×10^{18} eV (the ankle), cosmic rays are assumed to be from an extragalactic origin. The energy region between the knee and the ankle is

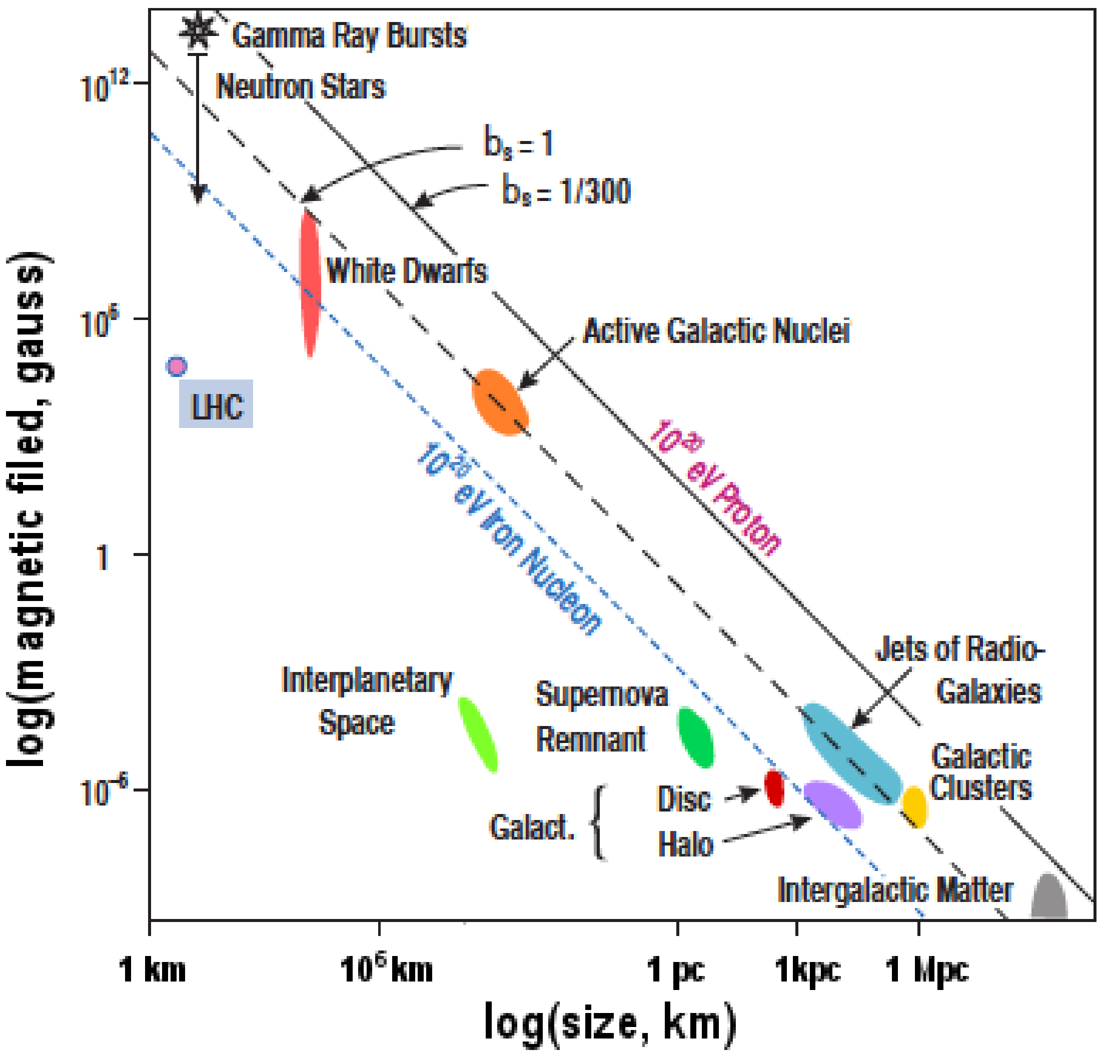

Figure 1.7: Hillas plot: A diagram of the relation between the strength of the magnetic field and the size of the possible source of cosmic rays (plot adapted from [26]).

still unclear [27]. However, theoretical models assumes the transition from Galactic to extragalactic origin of cosmic rays happens in the energy range between 10^{17} eV and 10^{19} eV [13] (as discussed in Section 1.2.1).

Supernova remnants (SNR) were first proposed in 1934 by Baade and Zwicky [28] and usually thought to be a candidate source of galactic cosmic rays at least up to the knee of the energy spectrum.

When a massive star explodes, the ejecta are expelled into the surrounding interstellar medium with a very high speed, carrying the kinetic energy of the explosion, and shock waves are formed. When a particle crosses the shock waves many times and gains enough energy to escape and become a cosmic ray.

Active Galactic Nuclei (AGN) are the most powerful compact objects in the universe and are expected to be a possible source of extragalactic cosmic rays. They are composed of an accretion disk around a supermassive black hole in their center and are sometimes associated with jets terminating in hot sopts. One can classify AGNs into two categories: radio quit AGN with no jets and radio loud AGN presenting jets. Both categories could accelerate particle to very high energies. The Pierre Auger Collaboration [29] observed a correlation between the arrival directions of high energy cosmic rays and the positions of some known AGNs (from the Veron-Cetty & Veron catalog (VCV) [30]) [31].

Gamma Ray Bursts (GRBs), first discovered by the Vela satellite in 1967 [32], are among the most energetic and luminous explosions known in the Universe. The explosion of a GRB leads to the formation of multiple shock regions which are potential acceleration sources for ultra high cosmic rays (UHECRs). Based on the fireball model, neutrinos are produced from the interaction between high energy cosmic rays protons and photons. Recently, searches with the IceCube Neutrino Observatory for neutrino emission from 300 GRBs found none:

"This implies either that GRBs are not the only sources of cosmic rays with energies exceeding 10^{18} *eV or that the efficiency of neutrino production is much lower than has been predicted [33]".*

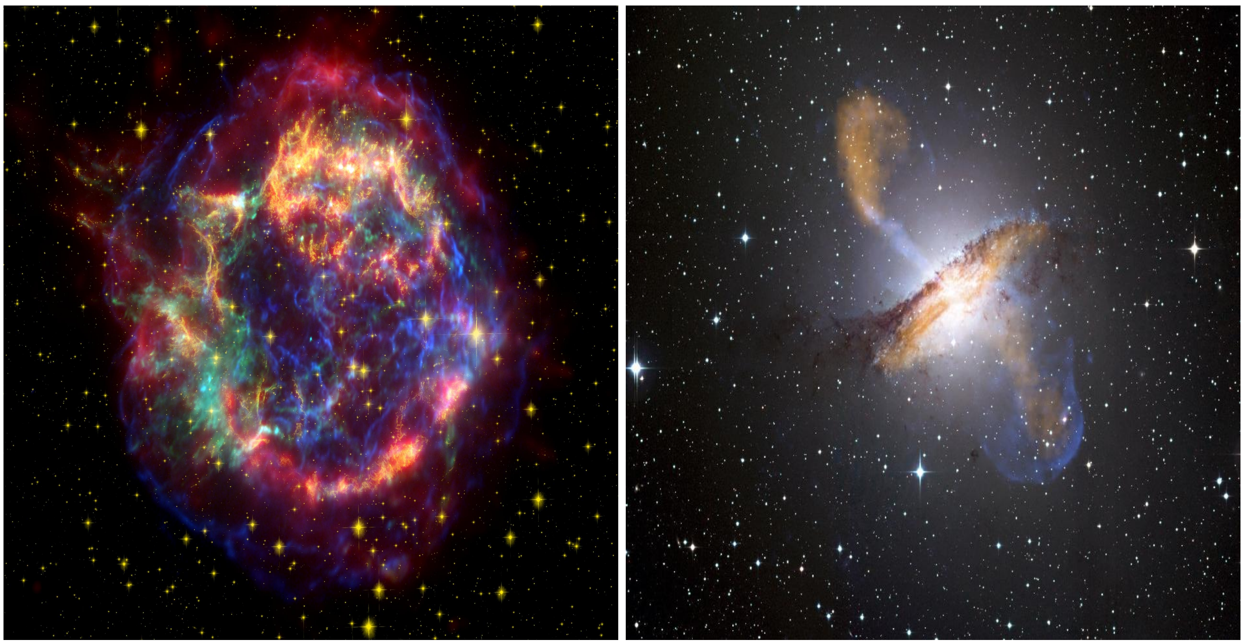

Figure 1.8: Candidate sources of cosmic rays. Left: A composite image of a supernova remnant (Cassiopeia A, 330 yr old) from three of NASA's observatories [34][35][36]. Right: A composite image of the nearest Active Galactic Nuclei, the Centaurus A radio galaxy [37][38]. The scale is different between the two images.

1.2.4 Acceleration

Finding and understanding the process that can accelerate particles to the highest energy observed in cosmic rays is a very important challenge in cosmic ray research. Many theoretical models have been developed to explain the acceleration mechanism. In 1949 Enrico Fermi [39] proposed the so called "Fermi acceleration mechanism" where he assumes that a cosmic ray particle can accelerate and gain more energy by collision with moving magnetic clouds or shockwaves in the interstellar space over a long period of time. Fermi proposed that, although particles can gain or lose energy per acceleration cycle, there will be average energy gain after multiple cycles. Therefore, the energy of the particle is increased significantly:

$$E_n = E_0(1+\xi)^n, \tag{1.4}$$

where E_0 is the initial energy of the particle, ξ is the relative energy gain and n is the number of acceleration cycles "encounters" ($n = \ln(\frac{E}{E_0})/\ln(1+\xi)$). The number of propagated particles with energy higher than E is:

$$N(\geq E) \propto \sum_{m=n}^{\infty}(1-P_{esc})^m = \frac{(1-P_{esp})^n}{P_{esc}} = \frac{1}{P_{esc}}\left(\frac{E}{E_0}\right)^{-\gamma}, \tag{1.5}$$

with P_{esc} the probability to escape from the acceleration region per encounter. The spectral index γ is:

$$\gamma = \frac{\ln\left(\frac{1}{1-P_{esc}}\right)}{\ln(1+\xi)} \approx \frac{P_{esc}}{\xi} = \frac{1}{\xi}\frac{T_{cycle}}{T_{esc}}, \tag{1.6}$$

with T_{cycle} the characteristic time for a single acceleration cycle. T_{esc} is the total time to escape from the acceleration region.

If the acceleration process has been running for a certain time t, the maximum energy becomes:

$$E \leq E_0(1+\xi)^{t/T_{cycle}} \tag{1.7}$$

There are two versions of Fermi acceleration. In the first version, charged particles start to collide with the moving magnetic clouds of plasma and diffuse by scattering on the irregularities in the magnetic fields (Figure 1.9a). If the particle is moving in the direction of the moving magnetic field, the particle loses energy and is reflected in the opposite direction. In a second collision, the particle gains energy and is reflected again in the direction of the magnetic field. The energy gain was found to be proportional to the square of the relative velocity of the cloud to the speed of light:

$$\xi \propto \beta^2, \tag{1.8}$$

where ξ is the energy gain and $\beta = u/c$. This is called the second-order Fermi mechanism because the energy gain depends on β^2. Since the speed of the cloud is very small compared to the speed of light, this mechanism is very slow to provide the observed large energies [1] [40].

In the second version, charged particles are accelerated by strong shockwaves caused by e.g. supernova explosions. Particles start to bounce back and forth in the upstream and downstream regions (illustrated in Figure 1.9b) with a speed much larger than the speed of sound and gain more energy. The energy gain was found to be proportional to the velocity:

$$\xi \propto \beta. \tag{1.9}$$

Thereby, this version is called the first order Fermi mechanism.

This mechanism is regarded as very successful because it naturally predicts a power law of the cosmic ray energy spectrum. One of the main problem in this mechanism is that there is a maximum energy than can be achieved $E_{max} \sim Z \cdot 10^{14}$ EeV, as explained in detail in [41].

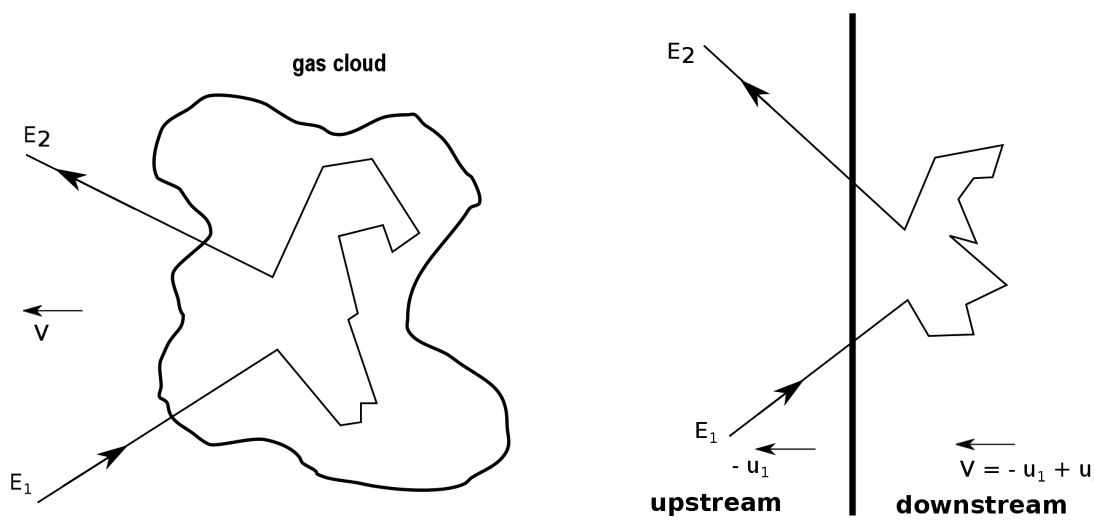

(a) (b)

Figure 1.9: Left: Acceleration across a plane front moving with certain speed in the universe (First order Fermi acceleration). Right: Acceleration by colliding with a magnetic gas cloud (Second order Fermi acceleration).

1.2.5 Propagation

Cosmic rays have to traverse a huge amount of matter in the universe before they are detected with cosmic ray detectors, and they may undergo different interactions on their way from the source to the detector. Therefore, the measured energy spectrum and elemental composition on the earth are not the same as at the source. Several numerical models have been developed to describe the propagation process of cosmic rays in the universe [40][42].

The diffusion model is the most popular model to describe cosmic ray propagation in the Galaxy at energies below about 10^{17} eV. The propagation equation for a certain particle can be written as:

$$\begin{aligned}\frac{\partial \psi(\overrightarrow{r}, p, t)}{\partial t} = \underbrace{q(\overrightarrow{r}, p, t)}_{\text{source}} + \overrightarrow{\nabla} \cdot (\underbrace{D_{xx} \nabla \psi}_{\text{diffusion}} - \underbrace{\overrightarrow{V} \psi}_{\text{convection}}) + \underbrace{\frac{\partial}{\partial p} p^2 D_{pp} \frac{\partial}{\partial p} \frac{1}{p^2} \psi}_{\text{diffusive reacceleration}} \\ - \underbrace{\frac{\partial}{\partial p} [\dot{p}\psi - \frac{p}{3} (\overrightarrow{\nabla} \cdot \overrightarrow{V})]}_{\text{particle loss}} - \underbrace{\frac{1}{\tau_f} \psi}_{\text{spallation}} - \underbrace{\frac{1}{\tau_r} \psi}_{\text{radioactive decay}} ,\end{aligned} \tag{1.10}$$

with $\psi(\overrightarrow{r}, p, t)$ the cosmic ray density per unit of total particle momentum p at a position $\overrightarrow{r}$, D_{xx} is the spatial diffusion coefficient, $\overrightarrow{V}$ is the convection velocity, D_{pp} is the momentum gain or loss rate, τ_f is the time constant for loss by fragmentation and τ_r is the time constant for loss by radioactive decay. The concept of cosmic ray diffusion explains why high energy particles have highly isotropic distributions and are retained in the Galaxy. Cosmic ray sources are assumed to be concentrated near the Galactic disk and to have a radial distribution. Cosmic rays could be transported by the convection of galactic winds. This could also produce adiabatic energy losses as the wind speed increases away from the disk. The spallation part is generally assumed to have the same kinetic energy per nucleon as the progenitor species. More details about Equation 1.10 can be found in [42].

A very simple model to describe cosmic ray confinement is the so called leaky box approximation. In this simplified picture, particles that traverse the Galaxy have a certain probability to escape from it. The diffusion and convection terms are approximated by the leakage term with some characteristic escape time of cosmic ray from the Galaxy. No spatial dependence of cosmic ray distribution, source density, and any other parameters are taken into account. The leaky box model states that cosmic rays accelerated at their sources are transported uniformly through the interstellar medium and their escape from the Galaxy is dependent on the energy of cosmic rays.

By neglecting the energy loss and gain through the propagation, a simplified propagation equation can be written as [40]:

$$\frac{\mathcal{N}_i(E)}{\tau_{esc(E)}} = Q_i(E) - \left(\frac{\beta cp}{\lambda_i} - \frac{1}{\gamma r_i}\right)\mathcal{N}_i(E) + \frac{\beta cp}{m}\sum_{k\geq i}\sigma_{i,k}\mathcal{N}_k(E), \tag{1.11}$$

where $\sigma_{i,k}$ represents the spallation cross section. This equation can be used when the fragmentation process results in the same energy per nucleon for primary and secondary cosmic rays. The energy spectrum for a given primary nucleus i can be written as:

$$\mathcal{N}_i(E) = \frac{Q_i(E)\tau_{esc}(R)}{1 + \lambda_{esc}(R)/\lambda_i}. \tag{1.12}$$

The interaction length $\lambda_i \sim 55$ g.cm^{-2} in the case of proton and $\lambda_{esc} \ll \lambda_i$ for all energies. Therefore, for and observed spectrum ($\mathcal{N} \sim E^{-(\gamma+1)}$), the source spectrum will be:

$$Q(E) \sim E^{-\alpha}, \tag{1.13}$$

with $\alpha \approx 2.1$. The interaction length $\lambda_i \sim 2.3$ g.cm^{-2} and the energy losses are due to interactions rather than to escape at low energies. The iron spectrum is flatter that the proton spectrum up to ~ 1 TeV/nucleon [40].

1.3 Extensive Air Showers

The flux of cosmic rays becomes very low at high energies (above $\sim 10^{14}$ eV) which makes it very difficult to detect them with direct measurements like satellite and balloon experiments, and indirect techniques are used. When a very high energy cosmic ray enters the Earth's atmosphere, it will interact with an air molecule and exchange some of its kinetic energy producing a cascade of particles called air showers, discovered in 1939 by P. Auger [2].

In Figure 1.10, a proton particle collides with the air molecule and a variety of secondary particles is produced. If the energy is high enough, these secondary particles will penetrate the atmosphere to ground level where they can be detected using variety of detection techniques. The first interaction in the atmosphere is not fixed and depends on the primary energy and primary mass of the original cosmic ray particle. This means that light primaries can penetrate deeper in the atmosphere before the first interaction occurs.

The development of extensive air showers in the atmosphere is characterized by the interaction and the decay of particles. Generally, a cosmic ray induced air shower has three components which can be detected on the ground: a hadronic component, an electromagnetic component and a muonic component (EM) [40].

The hadronic component of an air shower is the first generation of particles from the collision of the primary cosmic ray with the air molecules. Pions and kaons are the main particles created in the hadronic interaction. Low energy charged pions and kaons decay to form the muonic component of the air shower. Electrons and photons are produced from the fast decay of neutral pions into photons, forming the electromagnetic component with more than a third of the energy. Nucleons and other high energy hadrons will contribute further to the hadronic cascade.Therefore, the hadronic component is an important component in the development of the air shower, since it directly feeds the electromagnetic and muonic component [40] [43].

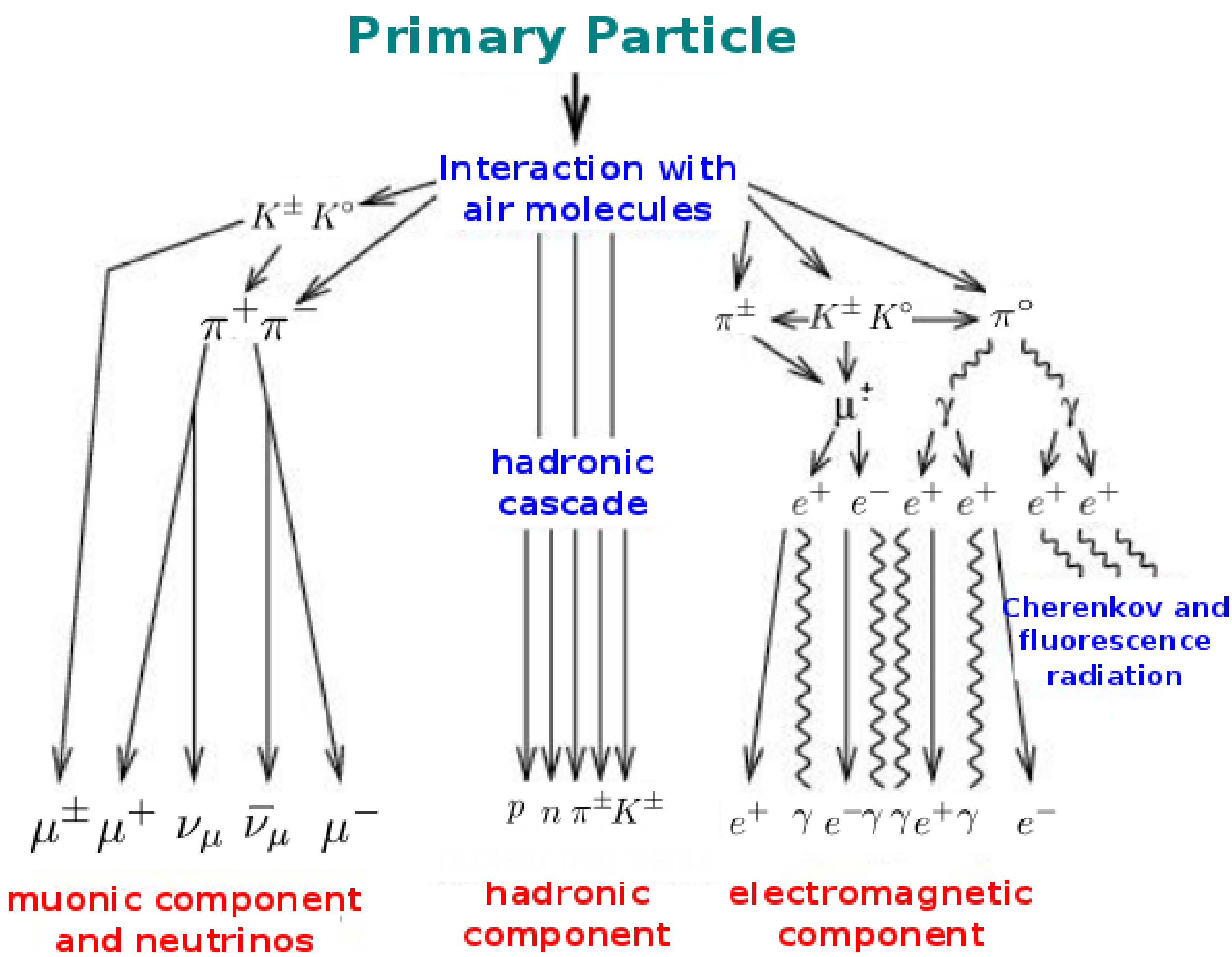

Figure 1.10: A schematic view of the components of an extensive air shower generated when a cosmic ray particle interacts in the atmosphere.

The electromagnetic component is the biggest component of induced air showers and contains electrons, positrons and photons. The EM component is explained in detail by the Heitler model [44] (Figure 1.11) where every particle undergoes a splitting after traveling a certain distance ($d = \lambda_r \ln 2$), where λ_r is the radiation length. Two new particles are created by the interaction and the energy is assumed to be equally divided between them. For each radiation length, the number of particles will be doubled. After n splittings, at an atmospheric depth $X = n\lambda_r \ln 2$, the cascade will

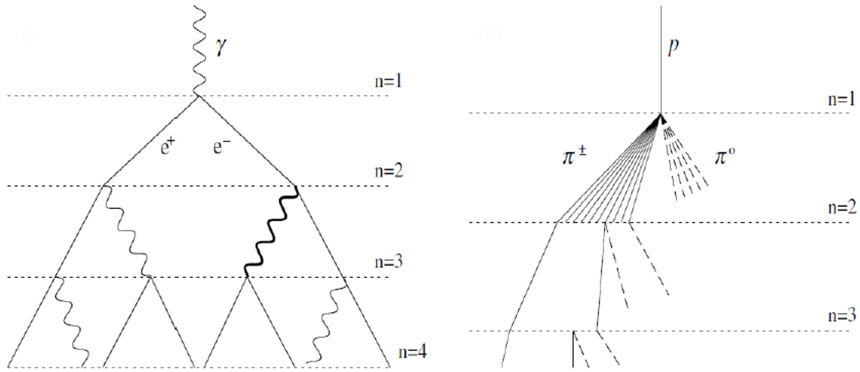

Figure 1.11: Schematic representation of the Heitler model for electromagnetic (left) and hadronic (right) cascade development. In the hadronic shower, not all pion lines are shown after the $n = 2$ level.

consist of $N(X) = 2^{\frac{X}{\lambda_r}}$ with energy $E = \frac{E_0}{2^{\frac{X}{\lambda_r}}}$, with E_0 the initial particle energy. The process will continue until the particle energy is not enough for more interactions and the cascade reaches shower maximum X_{max} [45][46].

The muonic component is generated from the decay of charged pions or kaons. At high altitude, mesons are more likely to decay rather than interact because of the low density of the atmosphere. The number of muons N_μ in a cosmic ray induced air shower as a function of energy is given by [47]:

$$N_\mu(E) = KE^{-\gamma_\mu}, \tag{1.14}$$

with the spectral index of muons $\gamma_\mu =\sim 0.757$ and K is a parameter highly dependent on the primary mass.

1.3.1 Detection of Extensive Air Showers

Several techniques were developed to indirectly detect cosmic rays at high energy by studying the properties of the induced EAS. The most common detection techniques use the Cherenkov, fluorescence and radio emission of the EAS in the atmosphere to determine the cosmic ray primary particle. In the following, some of the detection techniques are introduced based on [48].

Air Cherenkov Detectors

Along their propagation in the atmosphere, air showers emit Cherenkov light proportional to their primary energy. This light is emitted in a cone collimated around the shower axis. This technique can only operates on clear dark nights and in good atmospheric conditions. Small spacing between detectors is required to measure the lateral distribution of the air shower. Therefore, it is not appropriate to use this technique at very high energy ($E > 10^{17}$) eV where the low flux requires a large detection area. An example of such detector is the Tunka experiment [49].

Air Fluorescence Detectors

The passage of EAS in the atmosphere excites nitrogen molecules of air and produces fluorescence light (UV emission). The fluorescence light is produced isotropically, allowing the detection from all directions. The fluorescence detectors can cover a huge volume of the atmosphere, and can directly measure the longitudinal profile of the shower and the shower maximum X_{max}, which can be used to determine the primary mass. Similar to the air Cherenkov detectors, Air fluorescence detectors require a constant monitoring of the atmosphere and can only operate on clear moonless nights.

One of the first measurements using fluorescence light was done by Bunner in 1967 [50]. The current, fluorescence detectors are used to operate in combination with ground based detectors to give a stereo view of the air shower. This technique is used in the Pierre Auger Observatory [29] and the Telescope Array experiment (TA) [51].

Radio Emission Detectors

Radio emission from air showers has first been discovered experimentally in the 1960s.This emission is produced by the deflection of charged air showers in the magnetic field of the Earth, the geosynchrotron effect. The atmospheric conditions and noise from communication devices make it difficult to identify the air shower signature with detectors of the radio frequency. The radio detection technique was applied in the Pierre Auger Observatory [52], and has been investigated as an extension for IceCube and IceTop [53].

Ground Based Detectors

The EAS can also be measured at ground level using an array of scintillators or water Cherenkov tanks, deployed over a large surface area. The arrival time, the shower density and the location of the shower core on the surface can be measured using such experiments. The primary energy could be estimated from the lateral distribution of the signal in the perpendicular plane to the shower axis.

The most common air surface detection methods use water, ice Cherenkov tanks or plastic scintillators. Cherenkov tanks detect the Cherenkov light emitted by air shower particles when they pass through the tanks. This technique is used in the IceTop detector [54] (described extensively in Chapter 2) and in the Pierre Auger Observatory [29]. In the case of scintillation detectors, plastic scintillators are used to detect secondary charged particles at the ground. This technique is used in the KASKADE experiment [55].

Additionally, a combination of two techniques can also be used in one experiment in order to look at different components of air showers. This method is employed in the IceTop-IceCube coincidence analysis [46] and the Pierre Auger Observatory [29].

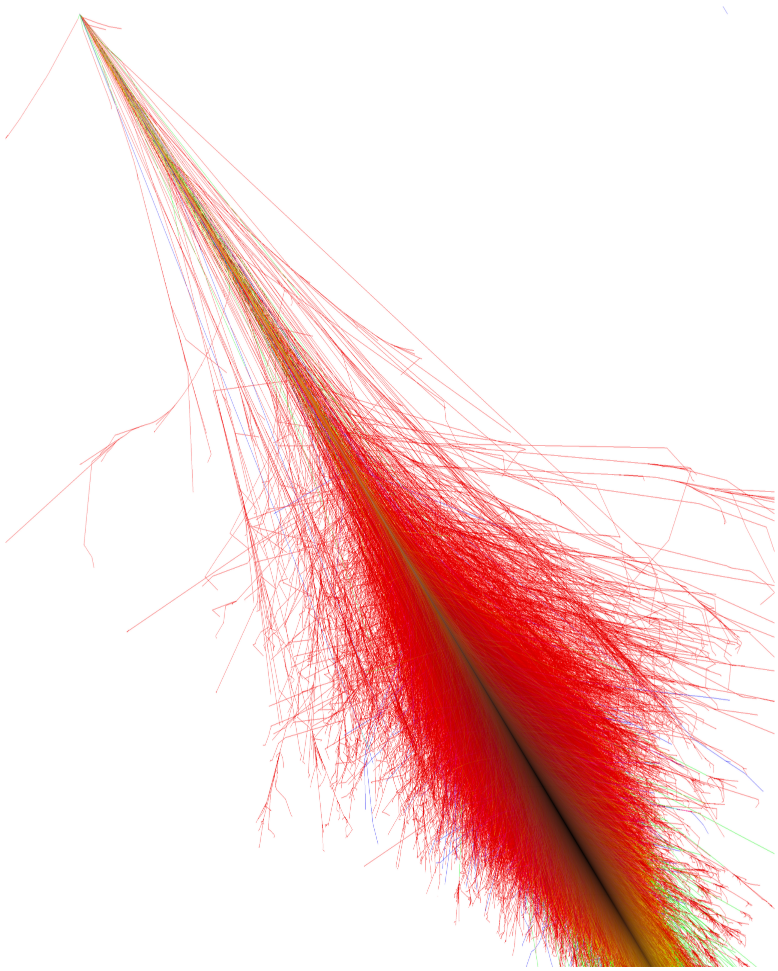

Figure 1.12: An example of a simulated proton induced shower with a primary energy 10^{15} GeV and inclination of 45°, interacting in the atmosphere. The blue color represents the hadronic component of the shower, the muonic component is in green and the EM component in red. Plot is from [56].

1.3.2 Some Recent Experiments

CREAM

The Cosmic Ray Energetics And Mass experiment (CREAM) was designed and constructed to measure the cosmic ray elemental spectra using a series of ultra long duration balloon flights. The goal of CREAM is to measure the cosmic ray elemental spectra in the energy range between $\sim 10^{11}$ and $\sim 10^{15}$ eV. The first flight of CREAM was launched from McMurdo Station, Antarctica in 2004. The balloon flew for 41 days and reached an altitude of 37 - 41 km. CREAM was flown six times between 2004 and 2010 accumulating $\sim$ 161 days of flight time.

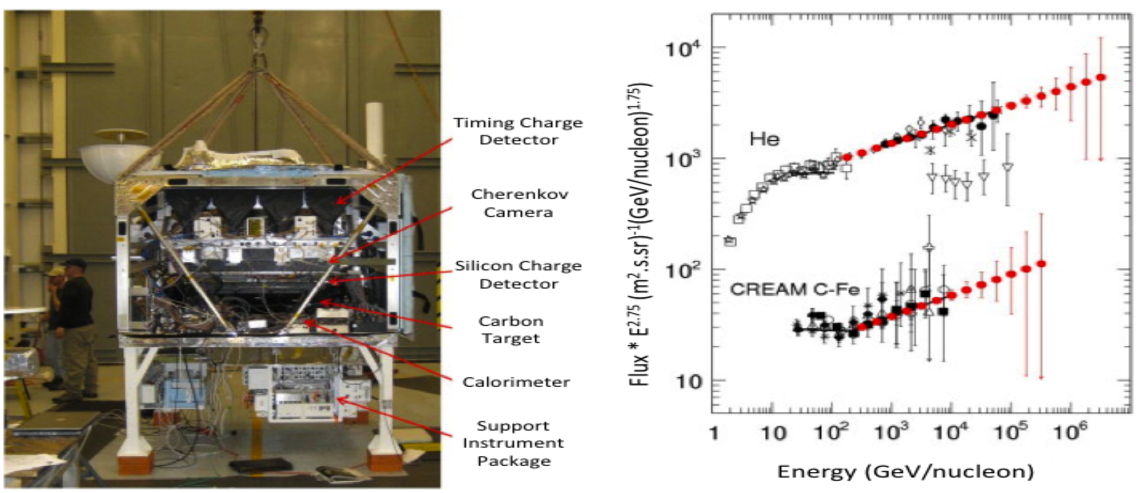

Figure 1.13: Left: A photo of the CREAM instrument. Right: Energy spectra from a nominal ISS-CREAM mission (red circles) and from previous measurements (black symbols). The energy spectra are compared to data from previous experiments, BESS (open squares), ATIC-2 (open diamonds), JACEE (X), and RUNJOB (open inverted triangles). The CREAM heavy nuclei data: Carbon (open circles), Oxygen (filled squares), Neon (open crosses), Magnesium (open triangles), Silicon (filled diamonds), and Iron (asterisks) [57].

The CREAM experiment was able to measure the proton flux from 2.5 TeV to 250 TeV and the helium flux from 630 GeV nucleon^{-1} to 63 TeV nucleon^{-1} at the top of the atmosphere[58]. For nuclei heavier than helium (C, O, Ne, Mg, Si and Fe), a broken power law can be fitted with spectral indices γ_1 = -2.77 $\pm$ 0.03 and γ_2 = -2.56 $\pm$ 0.04, below and above 200 GeV, respectively [57].

KASCADE and KASCADE-Grande

KASCADE is a ground based experiment situated on the site of the former Forschungszentrum Karlsruhe in the valley of the river Rhine in Germany at 110 m above sea level[55]. It uses an array of scintillation counters to measure the electromagnetic component of extensive air showers, the muonic component by scintillators and tracking chambers at four different energy thresholds and the hadronic component in a sampling calorimeter.

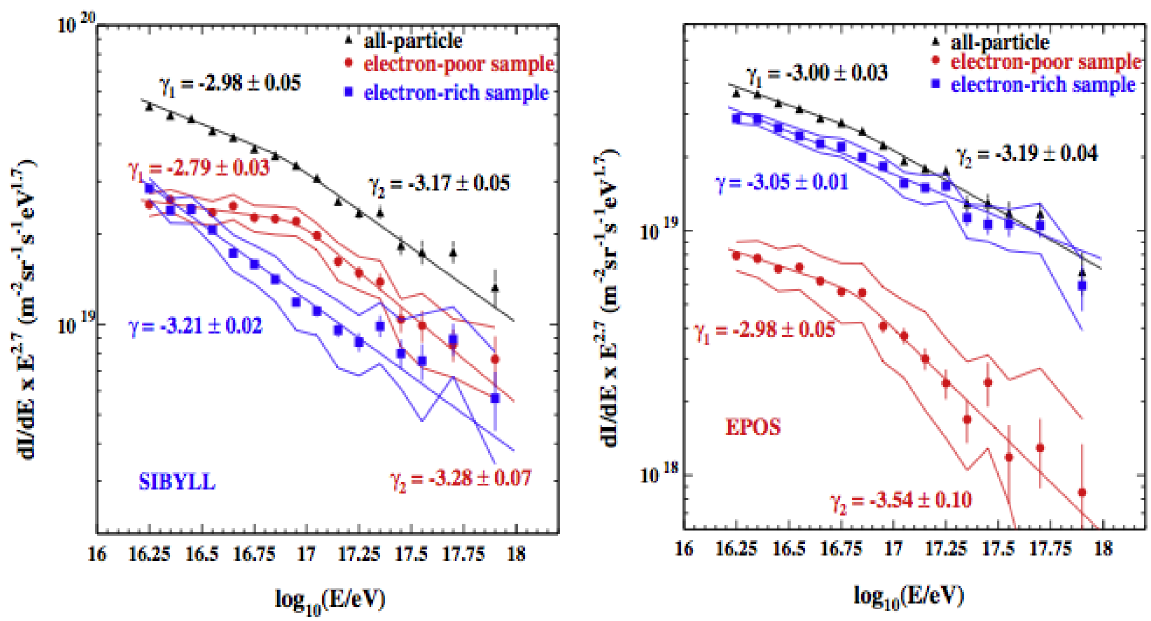

Figure 1.14: Left: The Reconstructed energy spectrum of the heavy and light components together with the all-particle spectrum for the angular range $0° - 40°$ for the SIBYLL hadronic interaction model (left) and the EPOS hadronic interaction model (right) [59].

In 1996, KASCADE-Grande was built as an extension of KASCADE experiment by adding 73 stations of the former EAS-TOP experiment, with an average spacing of 137 m [59]. KASCADE-Grande measured the all-particle energy spectrum in the energy range $10^{16} - 10^{18}$ eV. A hardening in the spectrum was observed at $2 \cdot 10^{16}$ eV and a small break-off at around $8 \cdot 10^{16}$ eV. However, these structures was found to be dependent on the interaction model used in the simulations. A separation of the mass into light and heavy components showed that the knee is caused by a break in the heavy component [59].

Pierre Auger Observatory

The Pierre Auger Observatory is located near Malarge in the province of Mendoza in Argentina, and designed to explore the ultra-high energy cosmic rays (with energies $> 10^{18.5}$eV) through the detection of induced extensive air showers in the atmosphere. The detector was designed as a hybrid detector using a surface array and nitrogen fluorescence detectors. The surface array consists of 1660 water Cherenkov detectors separated by 1.5 km and is used to determine the energy of the incident cosmic ray. It is overlooked by 27 fluorescence detectors to provide a calorimetric view of the shower development through the atmosphere. Using the hybrid technique provides a more complete view of the air showers [60].

Auger was able to measure the known ankle at 4.1 EeV where the spectral index changes from $\alpha = 3.27 \pm 0.02$ to 2.68 ± 0.01. Another feature was observed at 26 EeV where the spectrum becomes steeper. The suppression in the spectrum at the high energies, this can be due to the GZK cutoff [15, 16] or this is due to the maximum energy attained in astrophysical accelerators [61].

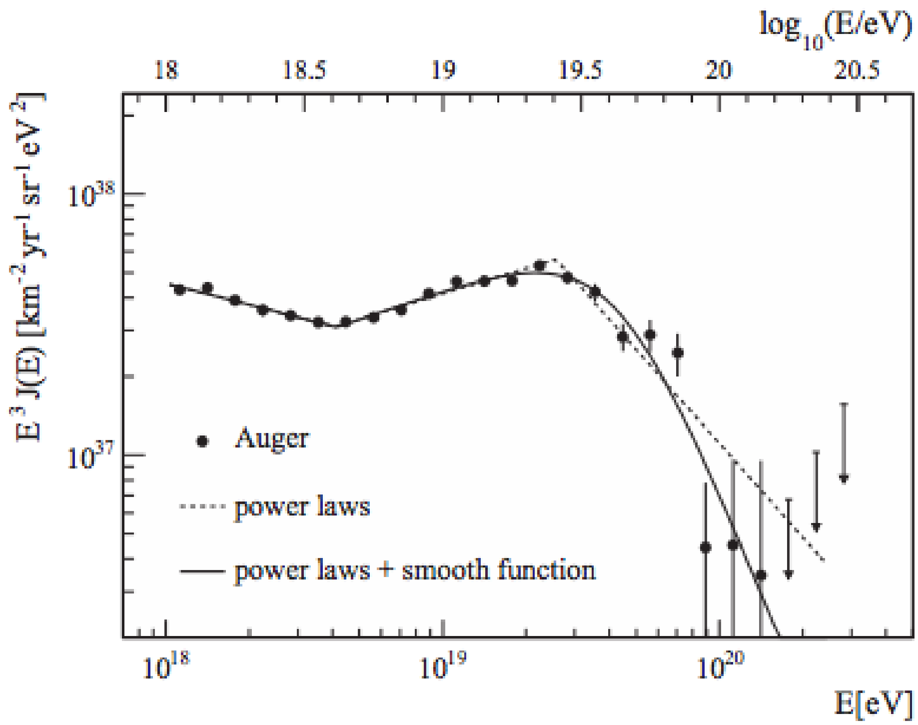

Figure 1.15: The cosmic ray energy spectrum derived from the hybrid data combined with the one obtained with the surface detector in the Pierre Auger Observatory. Error bars represent statistical uncertainties. The systematic uncertainty in the energy scale is 22% [61].

Chapter 2

IceCube and IceTop

The IceCube Neutrino Observatory is a gigantic telescope located at the South Pole in Antarctica. The detector consists of two main parts that can operate independently or as one combined detector. The surface part is the IceTop air shower array and the other part is the IceCube array in the deep underground ice. This analysis will use only the IceTop detector.

2.1 IceCube

The IceCube detector (Figure 2.1) [62] [63] uses 1 km^3 of Antarctic ice to detect Cherenkov light produced by charged particles traversing through the detector volume. The IceCube detector was constructed over seven years (between 2004 and 2011) and it consists of 86 vertical strings with an average horizontal string spacing of 125 m, except for eight strings (called DeepCore [64]) deployed at the center of the detector with a spacing of 10 m. Each string is equipped with 60 Digital Optical Modules (DOMs [65], Section 2.2.2) between 1450 and 2450 m depth. The DeepCore array aims to lower the energy threshold of IceCube by over an order of magnitude, to energies as low as about 10 GeV.

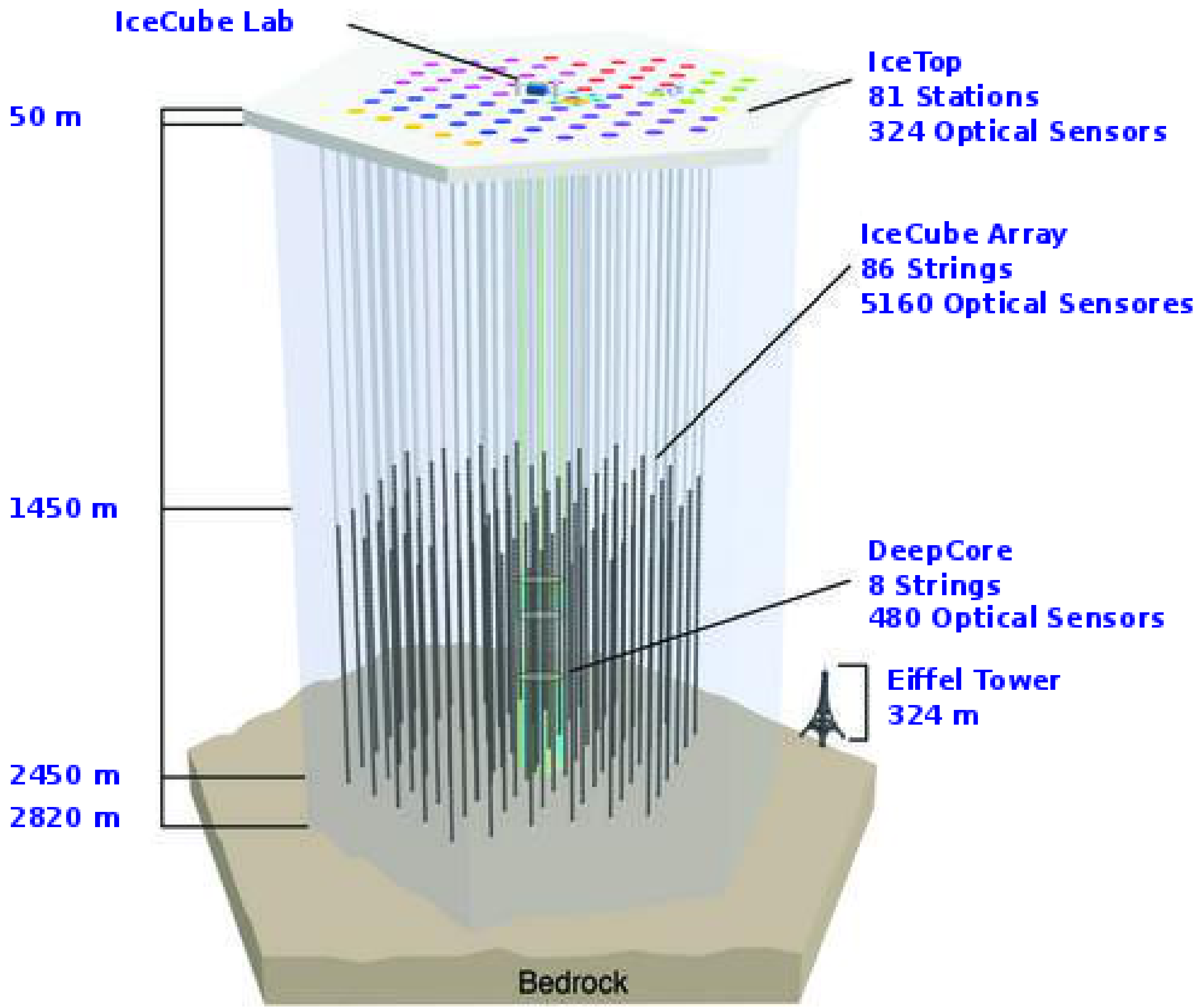

Figure 2.1: A schematic view of the IceCube and IceTop detectors. The vertical lines represent the 86 strings of the IceCube detector. DeepCore is the denser instrumented part of IceCube in the center, mentioned in green vertical lines. IceTop is the surface array where each colored dot represents one station. Different colors for the dots on the surface represent different years of construction. The IceCube Laboratory (ICL) is situated in the center of the array and contains all electronics and computers used to collect and process the data.

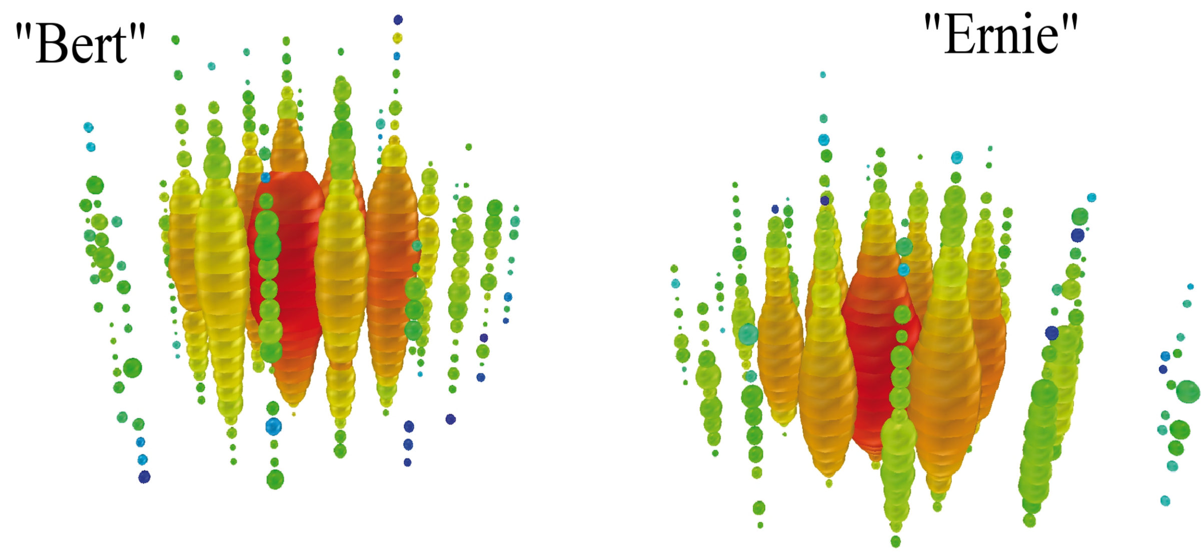

Figure 2.2: The first two interesting high energy neutrinos observed by IceCube. The event of the left is called "Bert" and has an energy around 1.1 PeV. The event of the right is called "Ernie" and has an energy around 1.2 PeV [66]. The two events were detected with data between May 2010 and May 2012. The size of the spheres represents the number of recorded photoelectrons in each DOM and the color represents the time of the signal in the detector.

The primary goal of IceCube is to search for very high energy astrophysical neutrinos via Cherenkov light produced by secondary charged particles created in the neutral current (NC) and charged current (CC) neutrino interactions in the glacial ice. These neutrinos originate when accelerated cosmic ray protons and nuclei interact with gas and light to produce pions and kaons which then decay, emitting neutrinos with energies proportional to the energy of the high energy cosmic ray that produced them. The observation of such very high energy neutrinos will provide insight into the origin and the acceleration mechanisms of high energy cosmic rays. Because of the very low flux and the small cross section with matter, a large effective area is needed. Large Cherenkov detectors like IceCube are able to detect these neutrinos. In July 2012, the IceCube collaboration announced the observation of the first two extremely high energy astrophysical neutrinos ever observed with energies around 1 PeV [66], shown in Figure 2.2.

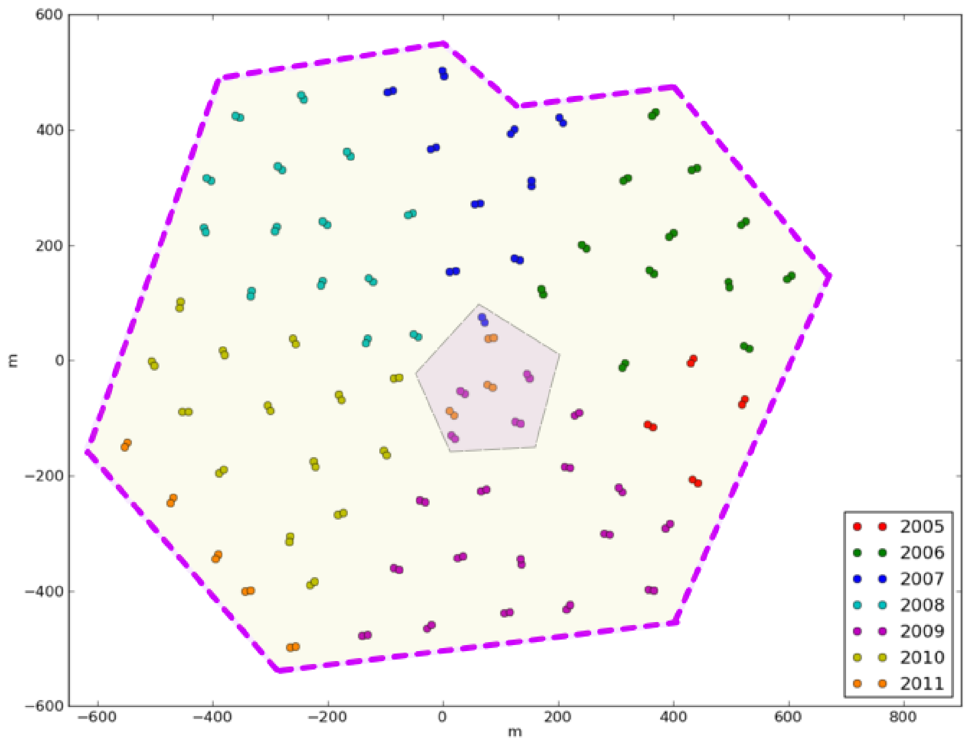

Figure 2.3: A schematic view of the completed IceTop air shower array. The dots on the surface represent IceTop tank. Each station has two tanks 10 m apart from each other and labeled as A and B. Different colors indicate different year of construction. The InFill array is situated at the center of the IceTop detector with smaller spacing between stations and consists of eight stations (26, 27, 36, 37, 46, 79, 80, 81).

2.2 IceTop

The IceTop air shower array is the surface component of the IceCube Observatory at the geographic South Pole covering 1 km^2 area above the IceCube detector. On the top of each IceCube string, one IceTop station is composed of two cylindrical ice-filled tanks separated by 10 m. Each tank is equipped with two Digital Optical Modules (DOMs) as optical sensors to detect Cherenkov light emitted by charged particles in the ice ([65], Section 2.2.2). Figure 2.3 shows the completed IceTop detector with 81 stations and the yearly deployment of the tanks/ stations. At the center of the detector, stations were deployed with smaller distances than other stations to make a denser array called the InFill array, in order to lower the energy threshold of the detector.

The IceTop detector is designed to detect air showers in the energy range between 500 TeV and 1 EeV. The lower limit is determined by the distance between stations, and with the steeply falling spectrum at high energies. A good measurement of the energy spectrum in this energy regime is very important in order to have an overlap with direct measurements at low energy and with experiments like Auger at the high energy.

2.2.1 IceTop Tank

Figure 2.4 shows a cross section view of one IceTop tank. Tanks are made of black, cross-linked polyethylene which is 6 mm thick, 1.1 m heigh and has an inner diameter of 1.82 m. Most of the tanks have a diffusely reflective white liner made of Zirconium dioxide powder in order to increase the light yield at the photomultiplier. Only eight tanks deployed in 2005 and four tanks deployed in 2011 have Tyvek linings instead. The two DOMs are placed at the top of the ice with a separation of 85 cm between their centers. The bottom half of the DOMs contains the photomultiplier tubes and it is submerged in the ice, while the upper half contains all the electronics used for data recording, digitization and transmission. The tanks are similar to the water tanks used in other air shower

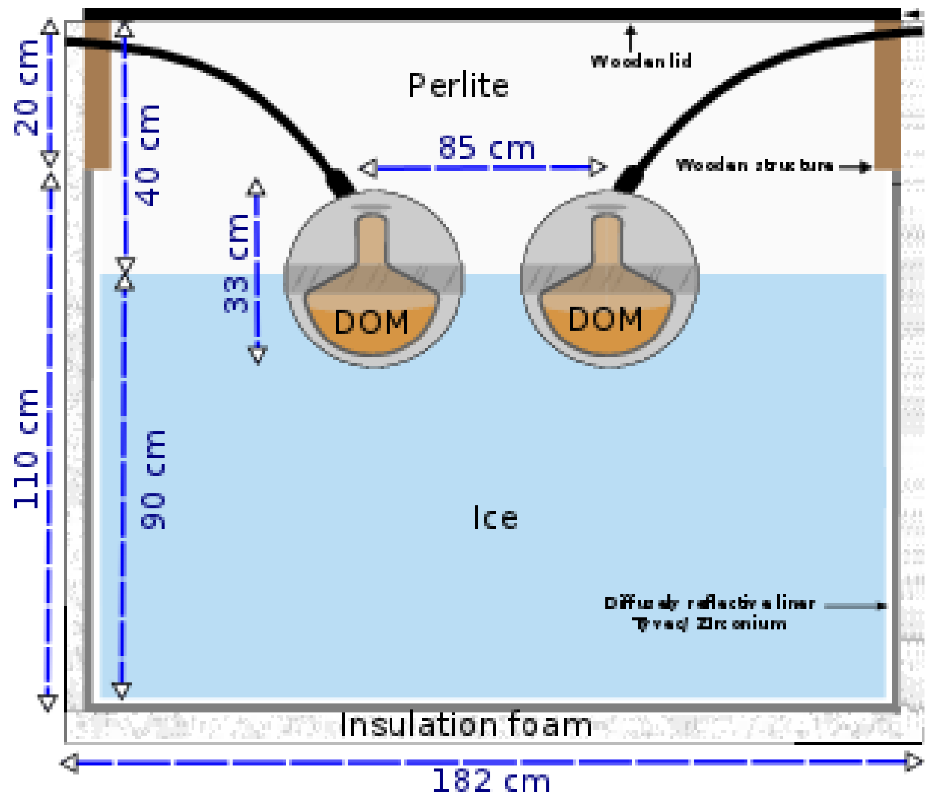

Figure 2.4: A cross section view of the IceTop tank.

experiments such as the Haverah Park experiment [67] and the Pierre Auger Observatory [29].

2.2.2 Digital Optical Module (DOM)

The Digital Optical Modules (DOMs) [65] are the basic component used, in both IceCube and IceTop, to detect Cherenkov light produced by charged particles in the ice. Each DOM consists of a 10″ Hamamatsu photomultiplier tube (PMT [68]), a 2 kV high voltage (HV) power supply for the PMT, the main board (MB), a LED flasher board with six pairs of LEDs, and a 13 mm thick glass sphere, as shown in Figure 2.5. The assembled DOM is filled with dry nitrogen to a pressure of half an atmosphere.

When the Cherenkov photons, created when the air shower particle interacts with the ice, hit the

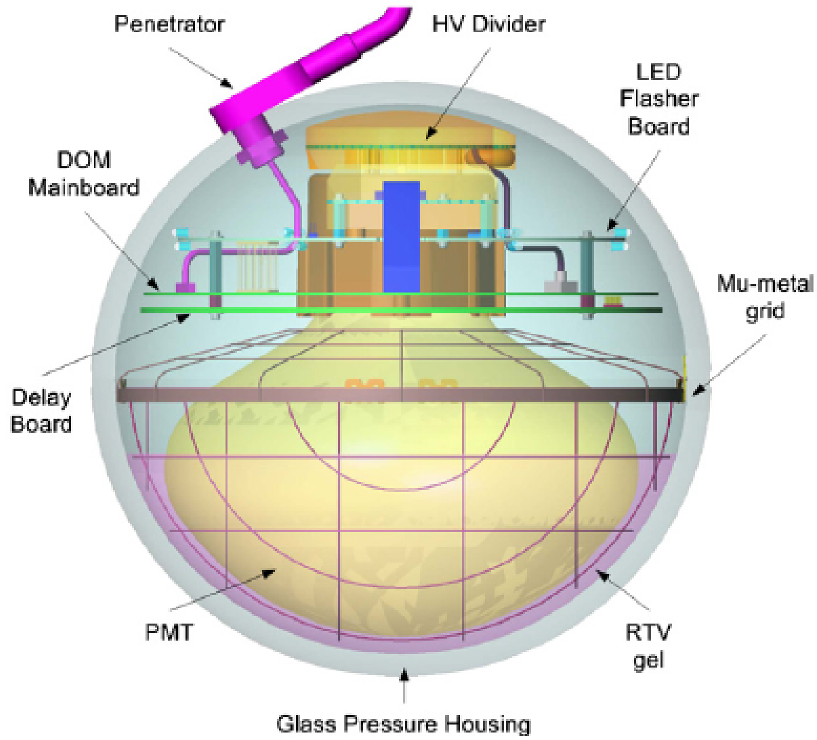

Figure 2.5: A schematic view of the IceCube digital optical module (DOM).

photocathode of the PMT and creates a bunch of photoelectrons (PE). The photoelectrons are accelerated and many secondary electrons are generated in the process (10^5 to 10^7 times more electrons) until they are collected at the anode on the opposite end of the tube.

The FPGA (Field Programmable Gate Array), on the main board of the DOM, performs the triggering, digitization and the communication between the DOM and the data acquisition system on the surface through a single twisted pair cable. The timing of the DOMs uses a 20 MHz oscillator inside the FPGA which is synchronized to a master clock in the IceCube lab.

DOMs are operated at different gains in order to increase the dynamic range of the detector. One DOM is operating in low gain (LG) and the other in high gain (HG). Each DOM has two discriminators, called MPE ″Multiple Photo Electron″ and SPE ″Single Photo Electron″. Both discriminators are used in IceTop for multiple PE thresholds. In high gain DOMs, the MPE discriminators are used for triggering on air showers with thresholds of about 20 mV which corresponds to a charge of a bout 23 PE, while the SPE discriminators are used to record scaler rates at different thresholds (from 0.5 PE to 30 PE). In low gain DOMs, the SPE discriminators are used with a threshold of about 4 mV which corresponds to a 270 PE signal, while the MPE discriminators are not used [54][69].

In addition, each DOM is equipped with a LED flasher board of 12 LEDs (6 horizontal and 6 tilted at 40 degrees). They are used for the calibration of the array geometry and to study the optical properties of the deep ice. They are only used in IceCube DOMs and not for IceTop.

IceTop DOMs have the same hardware as the DOMs deployed in the InIce detector but with some different characteristics of the data acquisition system due to different environmental conditions and physics requirements [54]. IceCube DOMs are numbered from 1 on the top of the IceCube string to 60 on the bottom of the string. The IceTop DOMs are numbered from 61 to 64 in each station, where 61 and 63 are high gain DOMs and 62 and 64 are low gain DOMs.

2.2.3 Deployment

The deployment of the IceTop detector was started with four IceTop stations in 2005 and completed with eight stations in 2011 to a total of 81 stations (Table 2.1). Tanks were set into trenches, then the trenches were filled back with snow in a way that their top surface is at the same level of the surrounding snow to avoid snow drifting and to minimize temperature variations. After the tank is in its position, the two DOMs are inserted with the photocathode of the DOM submerged. Figure 2.6 shows the tank after the water is frozen and the two DOMs are in the ice before the tank is filled with perlite and closed.

A junction box connects the two tanks in the station, the four IceTop DOMs, and the cable of the corresponding IceCube string. The 64 DOMs from each IceCube string and IceTop station were connected to the IceCube lab at the center of the array with a surface cable.

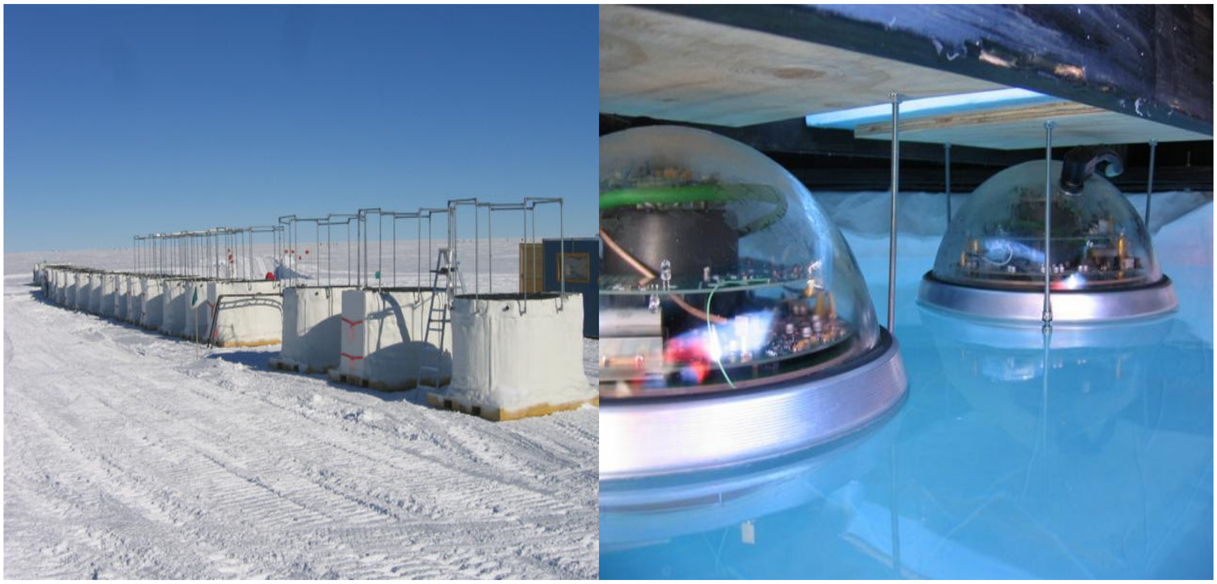

(a) (b)

Figure 2.6: Left: Group of IceTop tanks ready for deployment. Right: inside view of an IceTop tank. The DOM are placed that the lower half containing the photocathode of the PMT is below the ice surface.

Year	Number of IceTop stations	Total
2005	4	4 (IT-4)
2006	12	16 (IT-16)
2007	10	26 (IT-26)
2008	14	40 (IT-40)
2009	19	59 (IT-59)
2010	14	73 (IT-73)
2011	8	81 (IT-81)

Table 2.1: The yearly deployment of IceTop stations from 2005 until its completion in 2011.

(a) (b)

Figure 2.7: Left: An IceTop tank is placed in a trench and a bulldozer is filling the trench back with snow. Right: An IceTop station where the deployment of the two tanks is completed.

After the tank was filled with water to a depth of 90 cm and the DOMs were installed, the water is circulated with a Freeze Control Unit (FCU) in the bottom of the tank to get rid of the dissolved gas and make sure that the ice freezes perfectly clear, so that the Cherenkov light can be measured. The freezing process takes about 50 days until the water in the tank is frozen. Then the tank was opened and filled with 40 cm of expanded perlite, then it was closed again and the trench was back filled with snow to the surface.

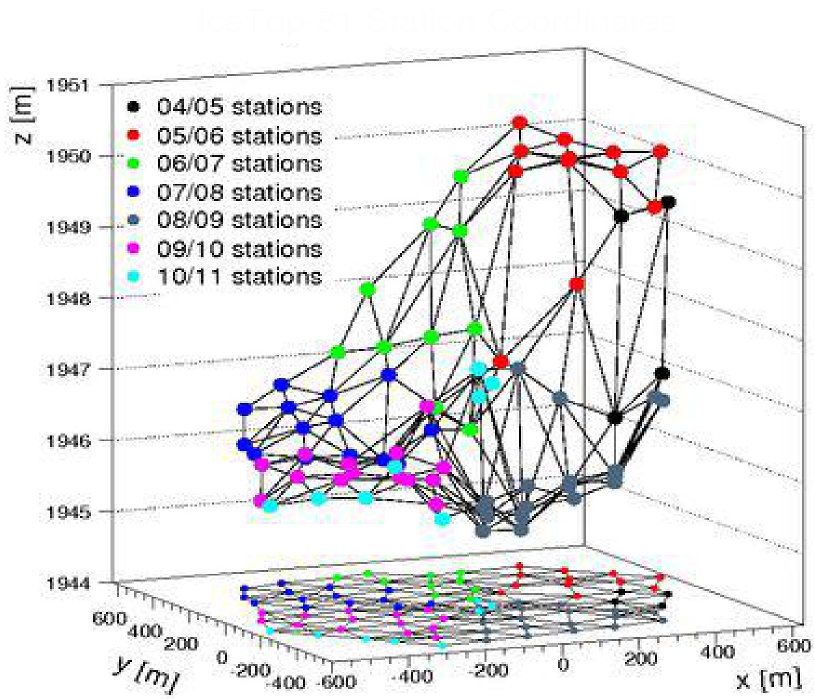

Figure 2.8: The IceTop detector in a 3D view. Different colors represent different years of deployment. A slope of 5 m is inherent in the terrain over 1 km^2 area of the IceTop array.

2.2.4 Data Acquisition

In the case that the signal passed the discriminator threshold the PMT output is sampled by an integrated circuit called ″Analog Transient Waveform Digitizer″ (ATWD) in 128 bins with 3.33 ns width for each bin. This corresponds to a total sampling of 422 ns. Each ATWD has four channels called ATWD0, ATWD1, ATWD2 and ATWD3. The first three channels are used for data taking and the fourth is used for other informations [65]. Each DOM has two ATWD chips which are used alternately to decrease the dead time. The three channels have different gains of 16, 2 and 0.25 respectively [54]. If the DOM is triggered, the FPGA opens the ATWD channels in one chip. Digitization starts for the highest gain channel and the other channels will only be digitized if any bin of the higher gain channel records more than 768 counts.

Pulses are digitized, in parallel, by a commercial 10 bit ″Fast Analog Digital Converter″ (FADC). The data recorded by the FADC are not used (yet) in IceTop analysis.

Triggering

The full waveform informations are only transferred to the IceCube laboratory (ICL) if the DOM receives a local coincidence (LC) from the neighboring DOM in the same station. If a high gain DOM is triggered, a signal is sent to both DOMs in the other tank of the same station. The local coincidence condition is only passed if one of the DOMs in the second tank saw a signal within a time window of 1 μs and the condition is called ″Hard Local Coincidence″ (HLC), Figure 2.9.

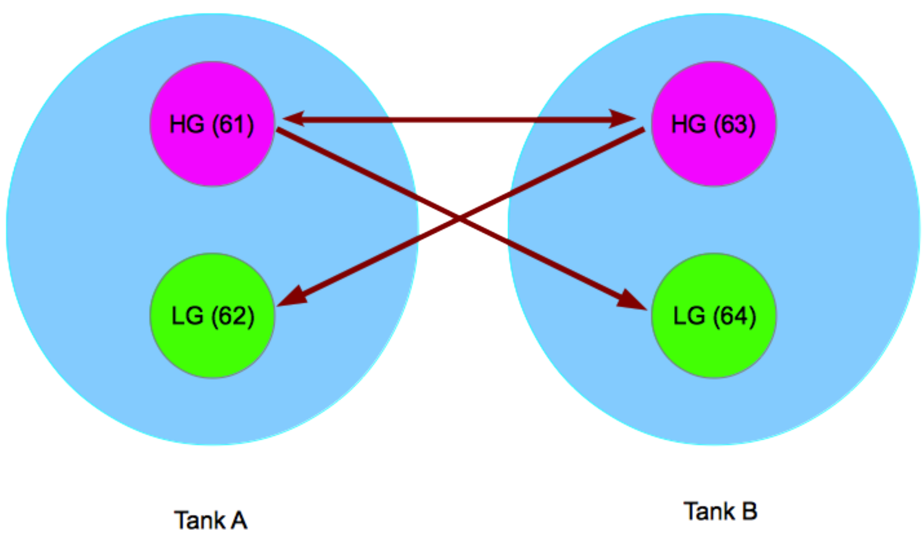

Figure 2.9: A schematic of the Hard Local Coincidence condition (HLC) in IceTop stations.

If the HLC condition is not fulfilled, only information about the charge and timestamp are transmitted, and the condition is called ″Soft Local Coincidence″ (SLC). SLC hits were only introduced in 2009 and can be used to detect single muons from low energy or inclined showers where the electromagnetic component is absorbed, and as a veto for in-ice studies.

Several trigger conditions are required in the IceCube lab before the event is kept permanently. The typical trigger for IceTop is the IceTop Simple Multiplicity Trigger (IceTopSMT) which requires any 6 HLC hits within 6 μs. The readout window starts 10 μs before the trigger window and lasts until 10 μs after the last of the 6 hits. A minimum bias trigger (IceTopMinBias) triggers every 10^4 hits (a prescale factor of 10^4). A calibration trigger (IceTopCalibration) is used for VEM calibration (Section 2.2.4 - calibration). All IceTop triggers are shown in Table 2.2.

Trigger Name	Condition	Readout window	Rate (Hz)
IceTopSMT	# hits $\geq$ 6 HLCs	10μs	30
IceTopMinBias	Prescale = 10^4	10μs	0.3
IceTopCalibration	LC not fulfilled	1μs	30

Table 2.2: List of IceTop triggers. IceTopSMT is the standard trigger used in the analysis.

Filtering

The disk space needed for the daily collected data from IceCube and IceTop is around 1 TB, which is too large to be transmitted via satellites. Therefore, the data were filtered based on the number of triggered stations and on the geometry of the detector according to different physics studies. All IceTop filters are summarized in Table 2.3.

The IceTopSMT trigger has to be passed for most of the filter classes. The most important filters, which will be used in this analysis, are the IceTopSTA3 and the IceTop_InFill_STA3 filters. The IceTopSTA3 filter requires at least 3 triggered stations. Events which pass the IceTopSTA3 filter and have less than 8 stations were pre-scaled for satellite transmission by transmitting only the third event, and the rest is transmitted without pre-scaling. Therefore, events with less than 8 stations have to be weighted by 3 before using them in the analysis. The IceTop_InFill_STA3 filter requires 3 triggered stations from the InFill array and aims to select low energy events (around 100 TeV).

An additional IceTop filter, called InIceSMT_IceTopCoin [54], was implemented to veto inclined high energy cosmic ray showers and to test and calibrate the entire IceCube detector. This filter requires the InIceSMT trigger to be fulfilled and to trigger at least one IceTop station.

Filter Name	Condition	Prescale
IceTopSTA3_11	IceTopSMT, # stations $>=$ 3	3
IceTopSTA8_11	IceTopSMT, # stations $>=$ 8	1
IceTop_InFill_STA3_11	IceTopSMT, # InFill stations $>=$ 3	1
InIceSMT_IceTopCoin_11	InIceSMT, # HLC hits $>=$ 1	100

Table 2.3: List of IceTop filters. IceTopSTA3 and IceTop_InFill_STA3 filters are used in the analysis.

Calibration

The calibration process of the signal is done by calibrating the PMT and the electronics of the DOM in order to obtain the charge in units of photoelectron and a time reference. Then the charge of the tank is calibrated with the ″Vertical Equivalent Muon″ unit (VEM) (shown in Figure 2.10) which is the signal produced by one single muon penetrating the tank vertically. The identification of the signal produced by muons is also important for air shower composition analyses. The electronic component of the DOM and the PMT gain are calibrated in a special calibration run with software called ″DOMCal″.

The time calibration is done by synchronizing the local 20 MHz oscillator of each DOM with a GPS controlled clock in the IceCube lab called ″Master Clock″, and the procedure is called ”Reciprocal Active Pulsing Calibration” (RAPcal). That was done by exchanging pulses between the IceCube lab and individual DOMs, which requires a certain time delay. The precision of the time calibration was found to be better than 1μs. More details can be found in [54].

The detected charge by a DOM in a certain tank at the same energy is not comparable between different tanks because of different optical properties of the tanks and DOM efficiencies. Therefore, the tank signals are calibrated by the signal from a vertical muon, and the tank signal is expressed in ″Vertical Equivalent Muon″ (VEM). Since 2009 a single muon calibration trigger is running together with the normal data taking. The muon calibration spectrum of DOM 19-61 is shown in Figure 2.10. The charge distribution can be expressed as a muonic signal and an electromagnetic signal. The muonic signal is fitted by a combination of a normalized Landau function to describe vertical muons and a Fermi function for non vertical muons ”edge-clipping muons” which enter and exit the tank through the side walls and do not go through the top and the bottom of the tank:

$$f(x,\mu) = p_0\left(L(x;p_1,p_2) + \frac{1.85}{p_1}.\frac{1}{exp(\frac{x-p_1}{p_2})+1}\right), \tag{2.1}$$

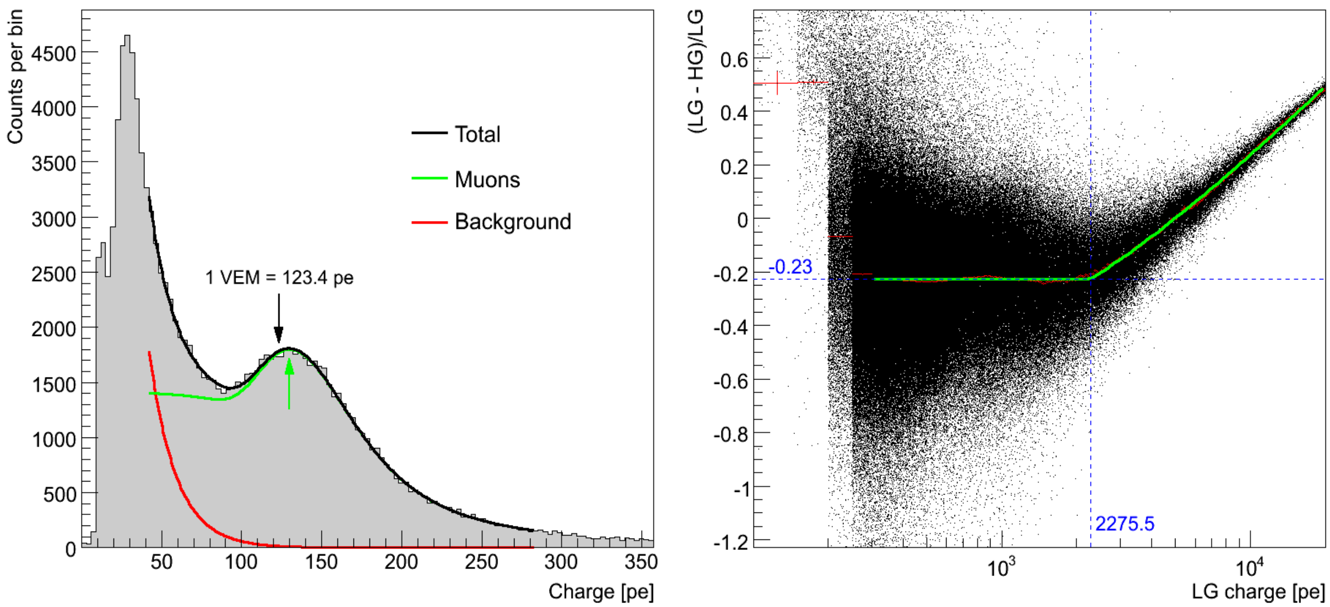

(a) (b)

Figure 2.10: Left: The VEM calibration spectrum for one single tank (19A), taken from [54]. The green fitting function is for the muonic component and the red for the electromagnetic component. Right: The relative charge difference as a function of the low gain charge.

where the first term $L(x; p_1, p_2)$ is a Landau distribution [70] and describes muons which are going through the tank, p_0 represents the number of vertical muons. The second term is the Fermi function which describes the edge-clipping muons, and p_1, p_2 are the location and the width of the Landau function. The factor 1.85 p_0 is obtained from geometrical considerations and was also verified with a toy simulation study.

The electromagnetic background signal can be fitted with a simple exponential with two free parameters,

$$f(x, EM) = p_3.exp(p_4.x), \tag{2.2}$$

The VEM unit is then defined as the charge at 95% of the muon peak position. This corresponds to about 120 PEs. The 5% offset of the muon peak was obtained from measurements of vertical muons with a zenith angle less than 17 degrees, measured with scintillation detectors. Measurements were done in 2005 and 2006 on tanks deployed one year earlier. The variation of the tank response to the vertical muon tagged with the scintillation detector was then investigated [71].

The muon spectra are only fitted for the high gain DOMs. Since the recorded charges should be the same in both high and low gain DOMs, a cross calibration for the low gain DOMs is applied (Figure 2.10b). The average charge difference between high and low gain for each tank as a function of the low gain charge is fitted with the function,

$$f(x) = \begin{cases} p_0 & x < p_3 \\ p_0 + p_1.log_{10}\left(1 + p_2.(x - p_3)\right) & x \geq p_3 \end{cases} \tag{2.3}$$

with p_0, p_1 and p_3 are the fit parameters, and $x = p_3$ is the crossing point between the two functions. The deviation from horizontal line above 2300 PE is due to the PMT saturation of the high gain DOM. The offset from zero below 2300 PE corresponds to the relative differences in efficiency of both DOMs which are higher for high gain DOMs [54].

2.3 Physics Goals of IceTop

IceTop, as a 1 km^2 air shower array on the surface, and IceCube as a 1 km^3 detector in the deep ice, can make a 3-dimensional air shower detector. There are several interesting physics topics that IceTop can study, either alone or in combination with the in-ice array. The main goal of this 3-D detector is to measure the energy spectrum of cosmic rays and determine their primary mass. The present analysis will only use the IceTop surface array to measure the energy spectrum of cosmic rays.

2.3.1 Energy Spectrum and Chemical Composition

The IceTop detector can detect air showers with energies around the ″knee″ (500 TeV until 1 EeV). The InFill array at the center of the detector, with a smaller distances between stations, will extend the energy range of the detector down to 100 TeV. At higher energies, the number of events will be very small for an accurate measurement. An energy spectrum measurement with IceTop is very important for several reasons:

- The detector is sensitive to a very interesting wide energy range which will provide an overlap with direct measurements (balloons, satellites) at low energy, and the spectrum at very high energy measured with other experiments (Auger, Telescope Array (TA)).

- At these energies, the transition from galactic to extra-galactic sources of cosmic rays is expected. The large amount of statistics will allow us to zoom in on the features of the energy spectrum and lead to a more precise measurement.

- IceCube can be regarded as a three dimensional cosmic ray detector with the electromagnetic component determined with surface IceTop detector and the high energy muon bundle, originating from the first interaction in the atmosphere, measured with deep underground detector (coincident events) [46]. Such measurement provides a powerful tool to measure the cosmic ray composition in the energy range between 500 TeV and 1 EeV.

- IceTop is located at a height of 2835 m above sea level which is equivalent to an atmospheric depth of about 680 g/cm^2 [54] which is very close to the shower maximum for this energy range (Figure 2.11). Air showers around this atmospheric depth are in their maximum size, this increases the amount of detected particles with the detector and reduces the shower fluctuations.

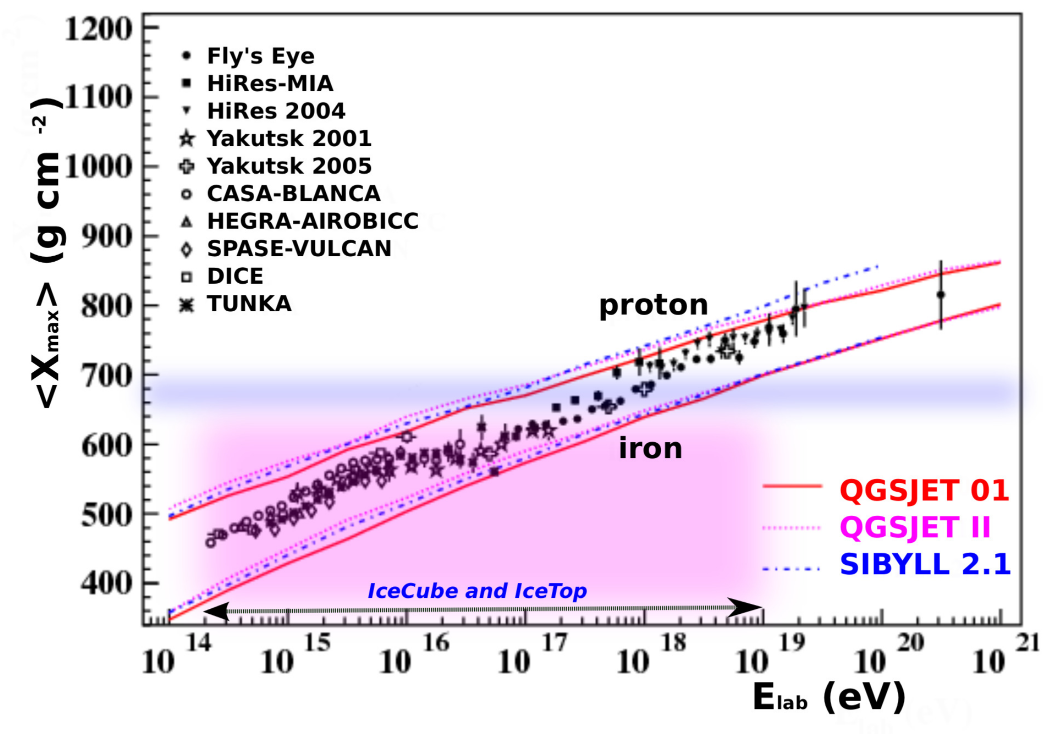

Figure 2.11: The shower maximum as a function of energy for proton and iron induced showers with different interaction models, and data from different experiments. The blue horizontal band represents the atmospheric depth at the surface including atmospheric variations. IceTop is sensitive to showers in the energy range shown in the magenta band.

2.3.2 Solar Physics with IceTop

The solar flares are intense flashes of extreme radiation emitted from the sun. Due to the high altitude and the nearly zero geomagnetic cutoff at the South Pole, secondary particle spectra at ground level retain a significant amount of information on the spectra of the primary particles. These particles are not able to trigger the IceTop detector but some of them still reach the surface and trigger individual DOMs with high rates. IceTop can detect these particles by using the increasing scaler rates in IceTop DOMs.

The SPE discriminators of the high gain DOMs are working at different thresholds (from 0.5 PE to 30 PE) and are used to study the rates of solar flares. By simulating the response of IceTop, the energy spectrum of these particle can also be determined in the energy range between 0.6 and 7.6 GeV [72].

2.3.3 Vetoing IceCube Events

Cosmic rays are the main background for the high energy neutrino detection with IceCube from the southern sky. IceTop can play an important role in acting as a veto for coincident muons generated by cosmic ray air showers [73].

2.3.4 High pT Muons

Muons with high transverse momentum ($\leq$1 GeV) are produced early in the shower development and can therefore be a probe of the initial interaction. These muons are produced from the decay of pions and kaons (conventional muons) or from the decay of heavy quarks , mostly charm (prompt muons). Prompt muons are expected to dominate beyond 100 TeV. Analysis of data from IC59 configuration showed that IceCube can measure the lateral separation of muons [74]. A study to use the reconstructed energy from IceTop to measure the composition of high energy cosmic rays is ongoing [75].

2.4 Environment Effects

Since the primary energy and primary mass are calculated by reconstructing air shower particles and not directly, any effect in the interaction medium has to be considered. The variations in the South Pole atmosphere and the snow accumulation on top of IceTop tanks have an influence on the number of detected particles and their energies.

2.4.1 Atmosphere

The South Pole atmosphere has a pronounced annual cycle. The atmosphere during the winter season at South Pole (from May to October) is cold and dense, therefore, particles are more likely to have early interactions with atoms and molecules in the atmosphere and produce secondary particles which will be later detected with IceTop. On the other hand, the atmosphere is warmer and less dense during the summer season. Therefore, particles are able to travel further and have more time to decay into muons to be detected with IceCube.

In addition, the sun, winds and clouds cause daily variations. These variations result in a change in the surface pressure. In Figure 2.12, we clearly see that the variation in the surface temperature is much larger in winter than in summer. In the summer season, the atmosphere has a nearly constant temperature (-20 to -30 degrees). In winter, by contrast, clouds and winds are changing the temperature significantly. The pressure varies with the temperature and density of the atmosphere. The average barometric pressure at South Pole is 680 hPa, and changes between 660 hPa and 710 hPa during the data taking period for the analysis.

The effect of South Pole atmosphere on cosmic ray detection with IceCube has been studied in [76]. The study showed that the atmospheric variations have a large effect on the muon multiplicity used in the coincidence analysis, while the effect is rather small on IceTop variables.

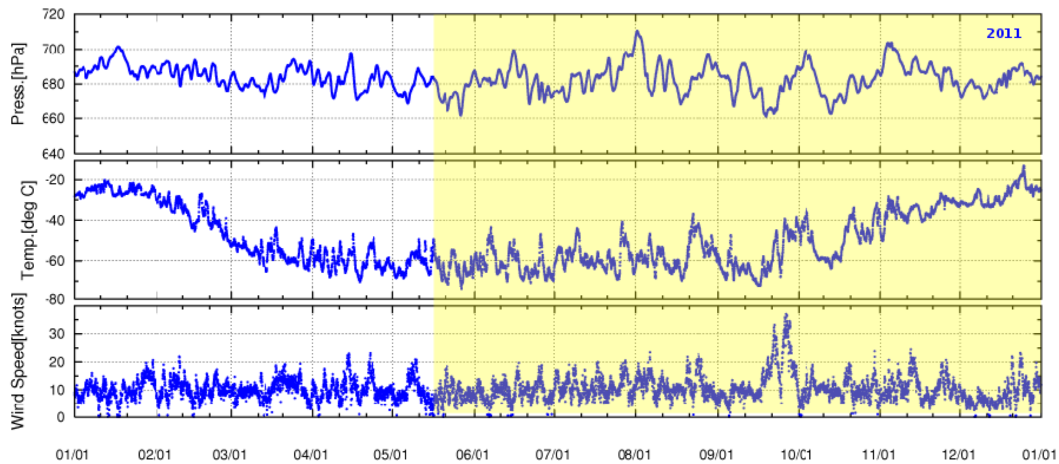

(a)

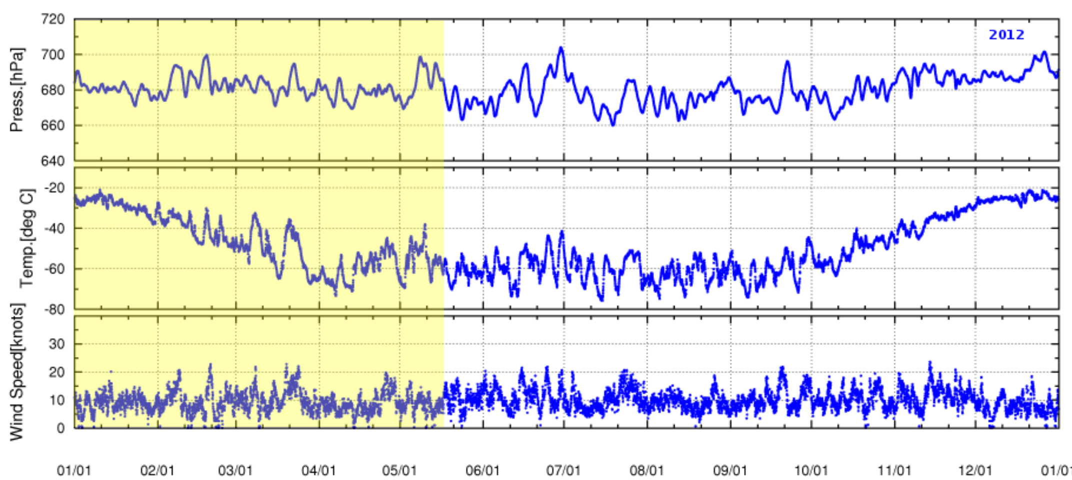

(b)

Figure 2.12: The South Pole surface pressure, temperature and wind speed variations over the entire 2011 (a) and 2012 (b) years. The yellow area shows the variations during the period of the data used for this analysis. The data points used here are obtained from [77].

2.4.2 Snow

At deployment, IceTop tanks were buried into the snow in such a way that their top surface is leveled with the surrounding snow level. Snow accumulation (about 25 cm per year) over time forms a layer of matter on top of the IceTop tanks which attenuates air shower particles. This attenuation depends on the particle type, its energy, direction and distance from the shower core.

The snow is not accumulated uniformly on the surface. Tanks from early deployment have more snow than tanks from the last season. Moreover, the accumulation depends on snow drifting caused by the blow of winds against buildings and sloped terrain. Figure 2.13 shows the snow accumulation on the array in October 2011. The distribution of snow varies from $\approx$ 2 m in the part from earlier seasons to a small amount on the latest deployed stations.

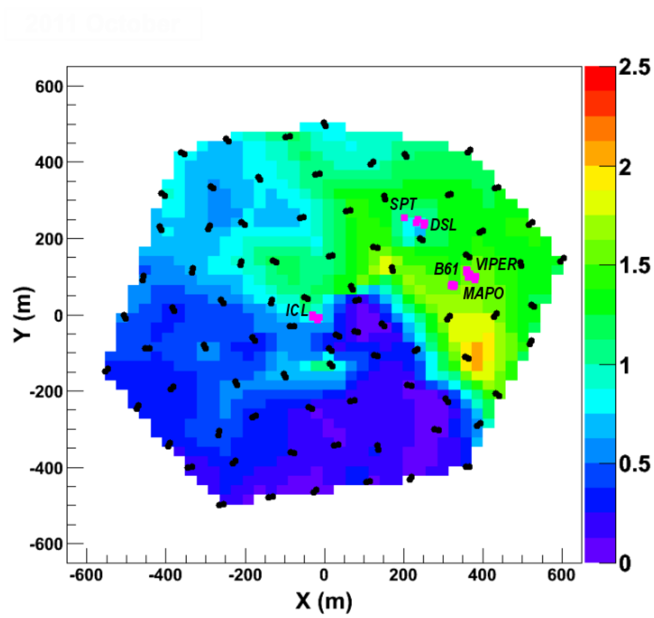

Figure 2.13: The IceTop array covered with accumulated snow in October 2011. Black dots represent IceTop tanks. The magenta squares are buildings and telescopes on the surface.

Snow heights on top of the IceTop tanks are measured by IceTop physicist during the summer season at South Pole and we rely on VEM calibrations (section 2.2.4 calibration) for the winter period on a weekly basis. The snow attenuate the electromagnetic component more than the muonic component where muons are more likely to penetrate the tank. Therefore, the change in the ratio of the muon signal f_μ Eq. 2.1 to the electromagnetic background f_{EM} Eq. 2.2 (Figure 2.10) is used to estimate the snow height:

$$\frac{S_\mu}{B_{EM}} = \frac{\int_{0.3}^{2.0} f_\mu \,\mathrm{d}\, S}{\int_{0.3}^{2.0} f_{EM} \,\mathrm{d}\, S}, \tag{2.4}$$

Figure 2.14a shows the correlation between the ratio S_μ/B_{EM} and the measured snow heights. An estimation of the snow heights is obtained by fitting the data point by the following function:

$$h_s^{est} = a \cdot \log(\frac{S_\mu}{B_{EM}} + b) \tag{2.5}$$

with typical parameters a≈1.37 and b≈1.75 from [54]. The obtained values are compared to the real measured snow heights 2.14b.

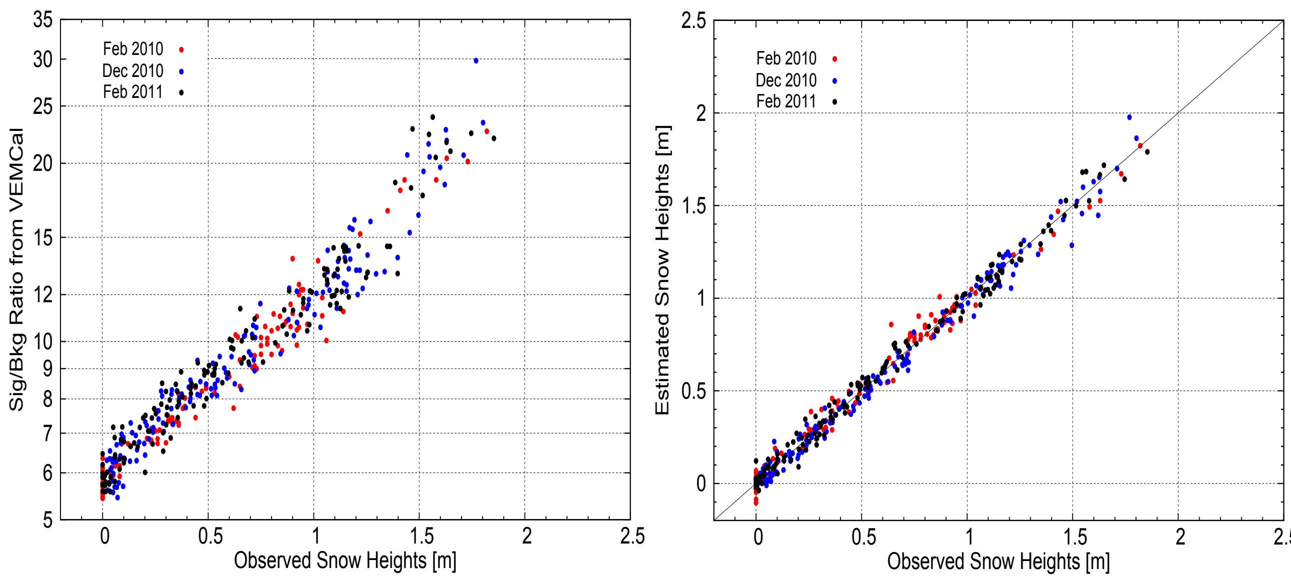

(a) (b)

Figure 2.14: (a): Correlation between the ratio of the muon signal to the electromagnetic background and the measured snow heights. (b): Snow heights determined from VEM calibration as a function of the measured snow heights. The measured snow height points are from February 2010, December 2010 and February 2011.

.

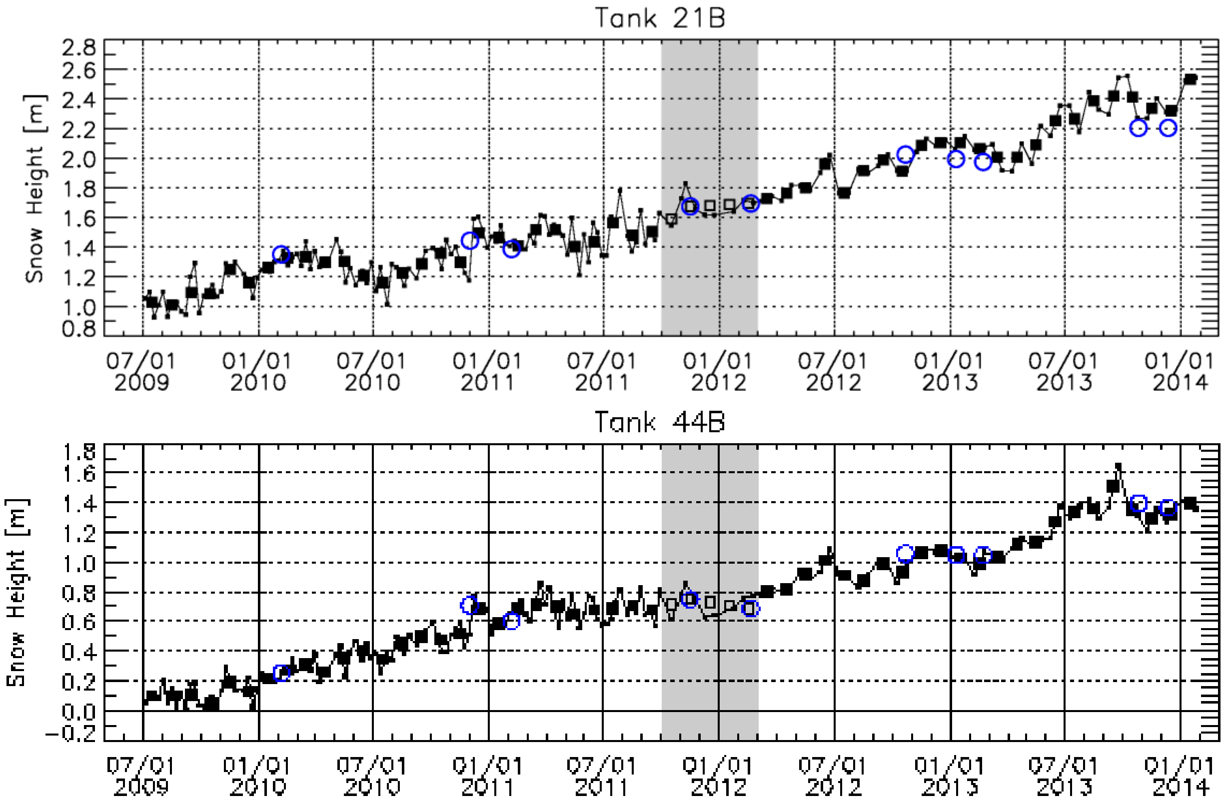

Figure 2.15: An example of the snow accumulation on top of IceTop tanks and the snow height estimation. The blue circles shows the measured snow height twice a year, the black line shows the estimated snow height from VEMCal, and the black squares represent the monthly average of estimated snow height.

Chapter 3

Simulation

In order to study the cosmic ray energy spectrum at high energies and over a wide energy range (100 TeV to 100 PeV) , one needs to use Monte Carlo simulations to have an accurate determination of the detector efficiency and to relate the measured parameters to the properties of the primary cosmic ray particle.

The IceTop simulation chain consists of two parts. First: simulating the development of the cosmic ray particle from the first interaction in the atmosphere to the ground level. Second: Simulating the detector response.

3.1 CORSIKA

CORSIKA ”Cosmic Ray Simulation for KASCADE” is a program to describe the evolution and properties of extensive air showers produced by high energy cosmic ray particles in the atmosphere. CORSIKA was originally designed in 1989 to simulate air showers for the KASCADE experiment [55] and then for its upgrade KASCADE-Grande [59], before is now developed as the standard simulation software used for most experiments dealing with air shower. Protons, light nuclei up to iron, photons, and many other particles can be used as a primary cosmic ray particle. CORSIKA can track the decay and interactions of particles in the atmosphere up to energies about 10^{20} eV and give the type, energy, location and the arrival direction of the created secondary particles.

Hadronic interaction models are the most uncertain part of CORSIKA and they are based on different theoretical frameworks. IceCube and IceTop use SYBILL 2.1 [78] as the the standard interaction model at high energy (E $>$ 80 GeV), and use FLUKA [79] for lower energies. The electromagnetic processes are described by the EGS4 [80] code.

The computing time and disk space needed to simulate very high energy showers (above 10^{16} eV) are huge, which sets a limitation on the amount of statistics at such energies. A thinning procedure [81] is introduced in CORSIKA to simulate those high energy showers. If the sum energy of secondary particles exceeds the thinning energy threshold, only one of these particles is tracked and an appropriate weight is given to it. Showers with energy more than 100 PeV are not used for this analysis, so the thinning procedure is not applied (It was used for energy spectrum and composition analysis with IceCube and IceTop [46]).

The atmospheric model used in CORSIKA was modeled according to the MSIS-90-E parametrization of the South Pole atmosphere in July 1, 1997 [82] which has a ground pressure of 692.2 g/cm^2.

CORSIKA version 73500 was used in IceTop simulations. [83]. The configurations used in the CORSIKA production are shown in the steering file in Appendix A.

3.2 Hadronic interaction models

The description of the high energy hadronic interactions plays an important role in the interpretation of the extensive air showers measurements. In particular, in the energy range which exceed the energy provided by man-made accelerators, the hadronic interaction properties have to be extrapolated. The highest energy available from particle accelerators comes from the Large Hadron Collider (LHC) at

CERN [84] with energies about $3 \cdot 10^{17}$ eV.

Many models have been used in EAS experiments. Here I will discuss briefly only the most used hadronic interaction models in EAS experiments which are implemented in CORSIKA.

SIBYLL 2.1 [78] is a hadronic interaction model based on the dual parton model (DPM) [85], the Lund Monte Carlo algorithms [86] and the mini jet model [87]. It accounts for the hadron-hadron and hadron-nucleus interactions and uses a semi-superposition model to determine the first interaction point in the nucleus-nucleus interaction. It can be used for very high energy air showers up to 10^{11} GeV. SIBYLL is widely used in air shower experiments and will be used as the high energy interaction model for this analysis.

QGSJET01 (Quark Gluon String model with JETs) [88] is based on the Gribov Reggeon Theory (GRT) [89]. It accounts for mini-jet production and operates up to energies about 10^{12} GeV. The cross section is tuned with LHC data in the most recent version.

VENUS (Very Energetic NUclear Scattering) [90] is also based on the GRT theory but does not accounts for the mini jet production. The model is valid up to 10^{7} GeV.

NEXUS (NEXt generation of Unified Scattering approach) [91] is a combination of VENUS and QGSJET with an extrapolation to higher energies.

EPOS (Energy conserving quantum mechanical multi-scattering approach based on Partons, Off-shell remnants and Splitting Parton Ladder) [92] is a second generation of the NEXUS model where several technical problems have been solved and a better agreement with the RHIC data has been observed. [1]

[1] All models are now ongoing through major updates with the latest data from LHC.

3.3 Mass production

Air showers were simulated in a wide energy range from 100 TeV to 100 PeV with CORSIKA 73500 [83]. Proton and iron showers are considered as the two extreme cases for primary mass assumption. Masses heavier than iron could not be simulated with CORSIKA and have anyway a small contribution in the spectrum. The measured data is expected to be in between the predictions of the two extreme assumptions. We generated 2000 showers per energy bin (energy bin is 0.1 in $\log_{10}\mathrm{E_{prim}}$) according to an E^{-1} spectrum to ensure enough statistics. The events are generated over a 360° azimuth angle and in a zenith range between $0°$ and $65°$ Table 3.1. The spectrum will be re-weighted to an $\mathrm{E}^{-2.7}$ spectrum before the knee and E^{-3} above the knee.

Mass	Energy range ($\log_{10}$E/GeV)	Number of showers	Zenith angle range °
H	5 - 8	60000	0 - 65
Fe	5 - 8	60000	0 - 65

Table 3.1: Simulation datasets used in the analysis.

In order to have a better description of the cosmic ray composition between the two extreme cases in future, more mass groups between proton and iron will be simulated.

3.3.1 Resampling

Simulating the shower development in the atmosphere with CORSIKA takes much longer than simulating the particle propagation in the detector. An oversampling procedure is used in order to increase the statistics and for a better understanding of the detector response. This means that each generated CORSIKA shower was used several times with an energy dependent radius to insure the shower will trigger the detector.

The resampling number was chosen for each energy bin (0.1 in $\log_{10}$E) such that every CORSIKA shower is used at least once. The resampling radius was optimized to be large enough that all events that can trigger the detector will be contained in the resampling area. It was found that the resampling radius is energy dependent [46]. The chosen resampling numbers and radii are shown in Table 3.2.

Figure 3.1 shows the distribution of the distance between the shower core and the center of the IceTop detector in three energy decades (5 - 6, 6 - 7 and 7 - 8), and without any cut.

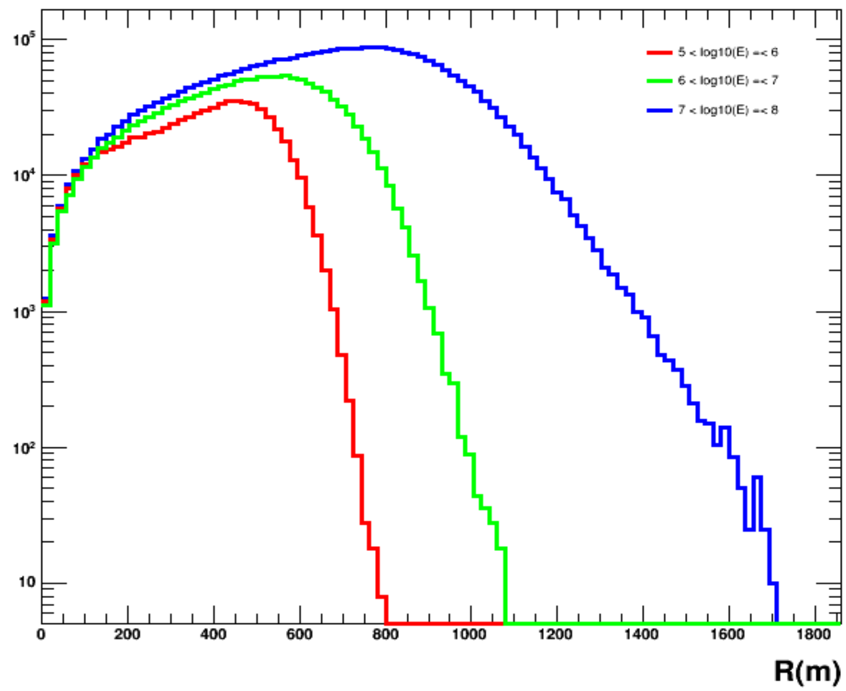

Figure 3.1: The distance between the core position and the center of the detector in three energy intervals for proton air showers.

Energy range ($\log_{10}$E/GeV)	Number of showers per energy bin	Number of resamples	Resampling radius
5 - 6	2000	100	800
6 - 7	2000	100	1100
7 - 8	2000	100	1700

Table 3.2: Resample radii and number of resampling per energy bin used for both proton and iron datasets.

3.4 Detector simulation

The output file produced by CORSIKA contains informations about the properties of the particle (type, position, momentum and the number of generated secondary particles). The injection and propagation of these particles into the IceTop tanks are simulated with the Geant4 toolkit [93], which is a program used to simulate the propagation of particles through matter. The Geant4 program takes all information of the particles from the CORSIKA output, and simulate the amount of light produced in the ice inside the tank and detected in the PMT.

The Cherenkov light produced when the particle interacts with the ice in the IceTop tank, the geometrical dimensions and reflectivity of the tank, and the amount of snow on top of each tank are simulated with in the Geant4 program. The propagation of Cherenkov photons in the ice takes a big amount of CPU time. Therefore, Cherenkov photos are not tracked through the ice and only the number of emitted photons is considered.

The PMT and the DOM are simulated with a software called PMTSimulator and DOMSimulator. The simulated PMT signal was obtained by superimposing Gaussian single photoelectron (SPE) waveforms and the charge was calculated according to the measured SPE distribution [68]. The DOMSimulator module simulates the electronics of the DOM starting from the PMT response [94]. Next the discriminators and local coincidence conditions are simulated. The trigger simulation is done using TriggerSim software and carefully checked by applying the trigger simulation software to real data [46].

The signal is calibrated with the VEM calibration procedure in the same way as for real tanks. The VEM unit is assumed to have the same number of Cherenkov photons for all tanks. The number of Cherenkov photons is converted first to VEM, then the number of photoelectrons at each DOM is obtained from the VEM calibration of a typical tank (Section. 2.2.4) [54].

Chapter 4

Air Shower Reconstruction

The energy of the primary particle is not obtained directly because IceTop can only observe secondary particles. The arrival time and the amount of light recorded for each event are used in reconstructing the properties of the air shower. These are the shower core position, shower direction and the size of the shower. From these quantities, an estimation on the energy of the primary cosmic ray particle can be made.

This chapter describes the shower reconstruction procedure that has been used in this thesis.

4.1 Reconstruction Tools

IceTop reconstruction is an extraction process for the basic quantities of the detected air shower. The main reconstructed parameters by IceTop are the shower core position (x, y), shower direction (θ, ϕ) and the shower size S_{exp}. These are obtained by fitting the recorded charges with a lateral distribution function and the signal times with a function to describe the shower front. First guess approximations for the core position and the direction of the air shower are made and used as a seed for an advanced likelihood logarithm in the next reconstruction steps.

4.1.1 Shower COG

A simple approximation method to estimate the core position of the air shower is to calculate the center of gravity (COG) of the position of the tanks with the highest signals weighted with the square root of the signal size.

$$\mathbf{r_{COG}} = \frac{\sum_{\mathbf{i}} \mathbf{r_i} \cdot \sqrt{\mathbf{Q_i}}}{\sum_{\mathbf{i}} \sqrt{\mathbf{Q_i}}}, \tag{4.1}$$

where $\mathbf{r_i}$ the position and Q_i is the recorded charge (in VEM) of the tank i.

For a better estimate of the core position, only seven tanks with the highest signals are used.

4.1.2 Plane Fit

The arrival times of tank signals are used to estimate the shower direction. The shower front is assumed to be a simple plane perpendicular to the shower axis propagating approximately with the speed of light. The direction of the shower is $\mathbf{n} = (n_x, n_y, -\sqrt{1 - n_x^2 - n_y^2})$ with $\mathbf{n} = \mathbf{1}$, and is calculated from the following χ^2 minimization:

$$\chi^2 = \sum_i \frac{(t_i^{\mathrm{m}} - t_i^{\mathrm{plane}})^2}{\sigma_i^2} \tag{4.2}$$

$$= \sum_i \frac{(t_i^{\mathrm{m}} - (t_0 + \frac{(\mathbf{n_x x_i + n_y y_i})}{c}))^2}{\sigma_i^2}, \tag{4.3}$$

where t_i^{m} are the times of the measured signal, t_0 is the arrival time of the plane, ($\mathbf{x_i}$, $\mathbf{y_i}$) are the tank coordinates, $\mathbf{n_x}$=$\sin(\theta)\cos(\phi)$, $\mathbf{n_y}$=$\sin(\theta)\sin(\phi)$ with θ and ϕ are the zenith and azimuth angles, respectively, and the time uncertainty is assumed to be constant for all tanks σ_i = 5 ns for all tanks. The height for all tanks is assumed to be the same. This assumption will be taken into account in the second iteration of the reconstruction.

The two first guesses for the core position (COG) and the shower direction (n_x, n_y) are used as inputs for a maximum likelihood fitting procedure to fit a lateral distribution function (LDF) to the recorded signals, explained in the next paragraph.

4.1.3 Lateral Distribution Function (LDF)

The signal measured in an IceTop tank is a combination of an electromagnetic and a muonic component of the extensive air shower. The electromagnetic component can be fitted with the so-called NKG function [45], but this is not appropriate for the muonic component or a combination of both components. Therefore, the signal charge expectation as a function of the distance to the shower axis was studied with Monte Carlo simulations [95] and was parametrized as:

$$S(\mathrm{r}) = S_{\mathrm{ref}} \cdot \left(\frac{r}{R_{ref}}\right)^{-\beta-\kappa\log_{10}(\frac{r}{R_{ref}})}, \tag{4.4}$$

where S_{ref} is the expectation value of the signal (in VEM) at a reference distance R_{ref} (m) from the shower axis. β is the slope of the lateral distribution function at R_{ref} which depends on the core position and direction . κ was fixed from simulation to 0.303 [54].

The logarithm of the signal $\log_{10}$(S/VEM) is:

$$\log_{10}(S(\mathrm{r})) = \log_{10}(S_{\mathrm{ref}}) - \beta \cdot \log_{10}\left(\frac{r}{R_{ref}}\right) - \kappa \cdot \log^2_{10}\left(\frac{r}{R_{ref}}\right), \tag{4.5}$$

and the function is called a ”Double Logarithmic Parabola function” (DLP function). An example of two IceTop events fitted with the LDF is shown in Figure 4.2.

Studies are ongoing to find a composite lateral distribution function to describe the muonic and the EM components separately [96].

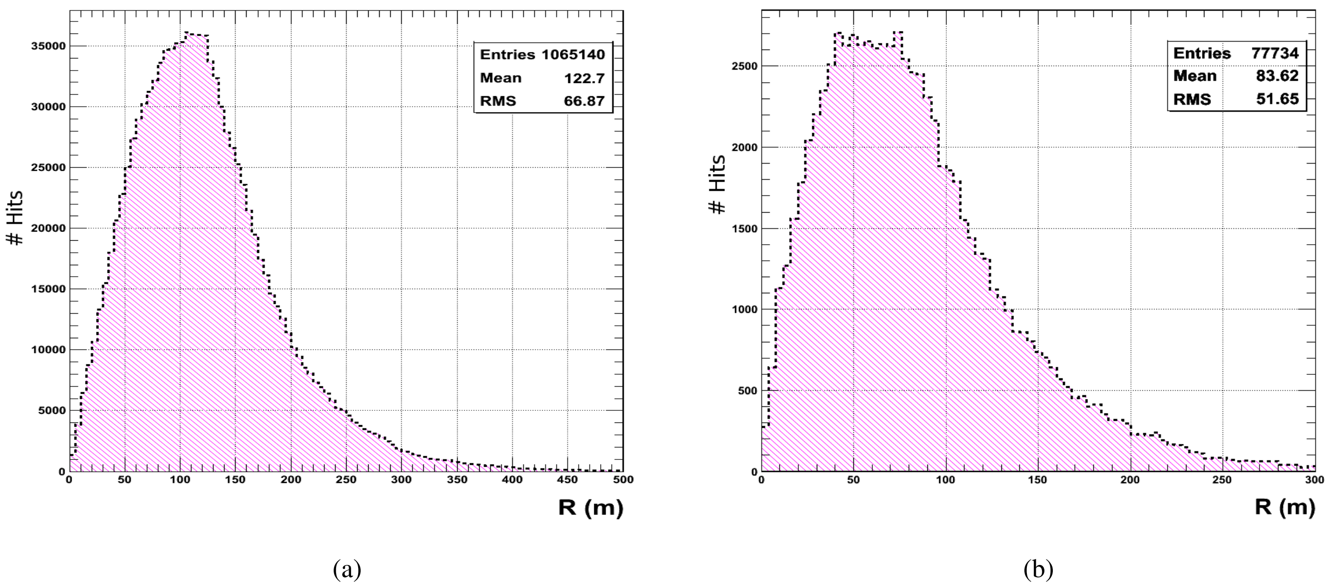

Figure 4.1: Distance between the shower core and the triggered stations for events with more than ten stations (a), and for small showers (b).

Reference Distance (R_{ref})

The measured signals in the IceTop tanks are used for the estimation of primary energy. Therefore, the accuracy in the determination of the parameters that could have an influence on this estimator is very important. The reference radius R_{ref} was chosen to be the best distance for evaluating the LDF, and is taken as the mean value of the distribution of the distance between the shower core position and the triggered stations. For showers that can trigger more than ten stations (Standard Showers Section. 5.1.1), this distance was found to be 125 m (Figure 4.1.(a)). It was also found that the signal fluctuation and the correlation between the S_{ref} and β [97] are minimal at 125 m. On the other hand, for showers that can trigger the InFill array and have less than ten stations (Small Showers Section. 5.1.1), R_{ref} was found to be 80 m (Figure 4.1(b)). The shower size is named S_{125} and S_{80} for standard and small showers, respectively.

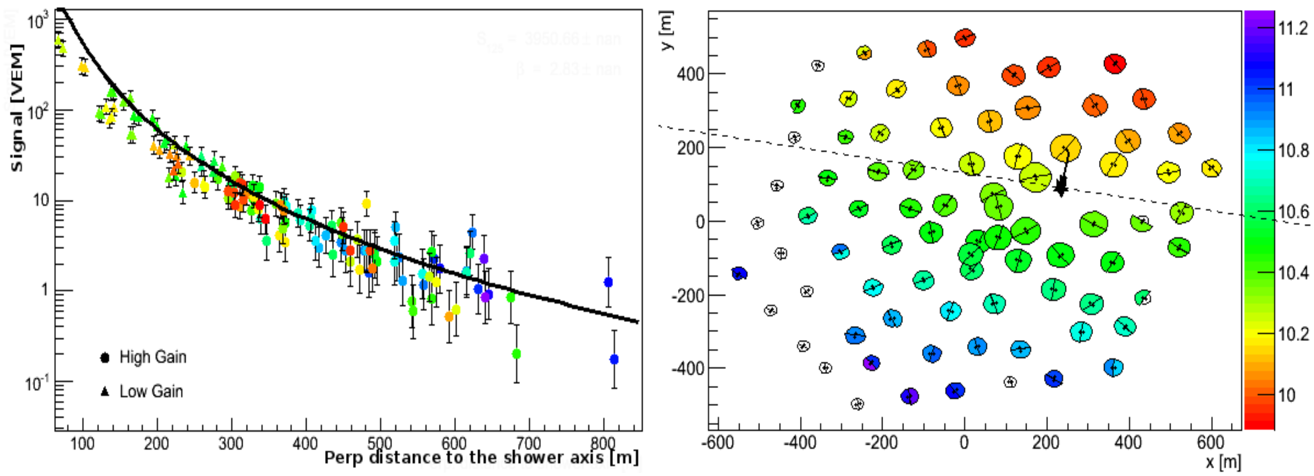

(a)

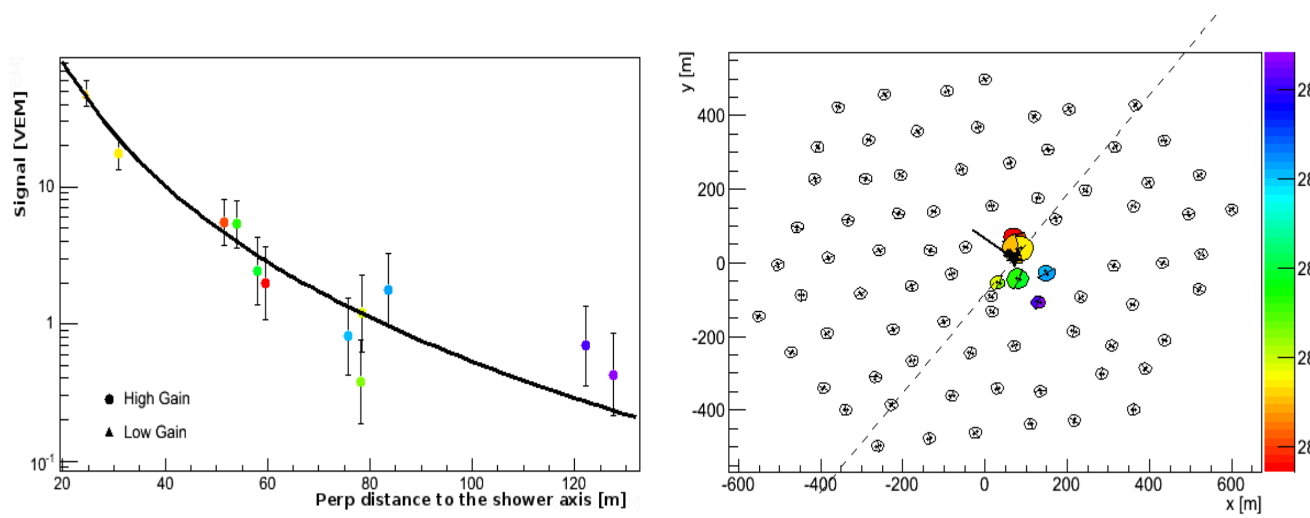

(b)

Figure 4.2: An example of two IceTop events. (a) shows an event that triggers more than ten stations, and (b) is for an event which triggers less than ten stations and triggers the InFill filter. On the left, the LDF function is shown where each data point corresponds to the tank signal measured in VEM. The footprint of both events on the IceTop detector is shown on the right. The dotted lines show the direction of the shower (azimuth) and the size of the arrow is proportional to the zenith angle. The color code represents the arrival times. The half circles are proportional to the signal detected in the tank. A reference radius of 125 m is used to evaluate the LDF in (a) and 80 m is used for (b) (see Section. 4.1.3).

Likelihood Fit

The likelihood fit is used to achieve the best determination of the shower core position x_c, y_c, the time t_0, the direction of the shower plane θ, ϕ, the strength of the signal at a certain distance from the shower axis S_{ref} and the slope of the fit β. In addition, the likelihood function accounts also for stations that did not have hits and for saturated tanks. So the likelihood function consists of four terms,

$$\mathcal{L} = \mathcal{L}_s + \mathcal{L}_t + \mathcal{L}_0 + \mathcal{L}_{sat}, \tag{4.6}$$

where $\mathcal{L}_s$ is the signal size likelihood, $\mathcal{L}_t$ describes the timing likelihood for the signal arrival time, $\mathcal{L}_0$ accounts for stations that do not trigger, $\mathcal{L}_{sat}$ is a saturation likelihood.

The signal size likelihood $\mathcal{L}_s$ represents the probability to measure a signal S in a tank i given the expectation values S_i^{fit} from Eq. 4.4,

$$\log \mathcal{L}_s = -\sum_i \frac{(\log_{10} S_i - \log_{10} S_i^{fit})}{2\sigma_s^2(S_i^{fit})} - \sum_i \ln(\sigma_s(S_i^{fit})), \tag{4.7}$$

The sum runs over all triggered unsaturated tanks. The second term of the likelihood represents the charge fluctuations. To account for the charge fluctuations, the measured charge in both tanks of a station were compared. The charges were found to be log-normal distributed around their expectation values [98].

$$\log_{10}(\sigma_s(S_i^{fit})) = \begin{cases} -0.5519 - 0.078\log_{10}(S) & \log_{10}(S) < 0.340\ \text{VEM} \\ -0.373 - 0.658\log_{10}(S) + 0.158\log_{10}^2(S) & 0.340\ \text{VEM} \le \log_{10}(S) < 2.077\ \text{VEM} \\ -1.0581 & 2.077\ \text{VEM} \le \log_{10}(S) \end{cases} \tag{4.8}$$

The timing likelihood $\mathcal{L}_t$ represents the probability to measure the arrival time of the signals on a curved shower front, taking into account the signal time fluctuation. The shower front curvature is fitted to improve the reconstruction of the shower direction.

The shower front curvature (Figure 4.3) is parametrized as:

$$\Delta t(R_i) = aR_i^2 + b\left(1 - e^{-(\frac{R_i}{\sqrt{2}\sigma_{curv}})^2}\right), \tag{4.9}$$

with the constants: $a = 4.823 \times 10^{-4}$ ns/m^2, $b = 19.41$ ns and $\sigma = 83.5$ m from [54].

The arrival time fluctuations depend on the distance of the tank from the shower axis and found from experimental data [54]:

$$\sigma_t(R_i) = 2.92\text{ns} + 3.77 \cdot 10^{-4}\text{ns} \cdot (R_i/\text{m})^2. \tag{4.10}$$

The resulting timing likelihood is described as:

$$\log \mathcal{L}_t = -\sum_i \left(\frac{t_i - t_i^{plane}}{2\sigma_t^2} - \ln(\sigma_t(R_i)/ns)\right), \tag{4.11}$$

where t_i is the measured signal time, t_i^{plane} is the expected time from Equation 4.2 and $\sigma_t(R_i)$ represent a radius dependent time fluctuation from Equation4.10.

When one tank in the station does not trigger, the station will be counted as a no-hit station. Therefore, the LC condition is not passed (Section 2.2.4) and the other triggered tank in the station will be counted as SLC hit. This is not included int the reconstruction yet because a discrepancy in the number of SLC hits between data and MC is not yet completely understood. The no-hit likelihood $\mathcal{L}_0$ accounts for stations that do not trigger,

$$\mathcal{L}_0 = \sum_i \left(\ln(1 - (P_i^{hit})^2)\right), \tag{4.12}$$

with $(P_i^{hit})^2)$ is the probability that one tank in the station has a signal at a given charge expectation,

$$P_i^{hit} = \frac{1}{\sqrt{2\pi}\sigma_{log_{10}S}S_i^{fit}} \int\limits_{\log_{10} S_{\text{thr}}}^{\infty} \exp\left(-\frac{(\log_{10} S_i - \log_{10} S_i^{fit})^2}{2\sigma_s^2(S_i^{fit})}\right) d\log_{10} S_i, \tag{4.13}$$

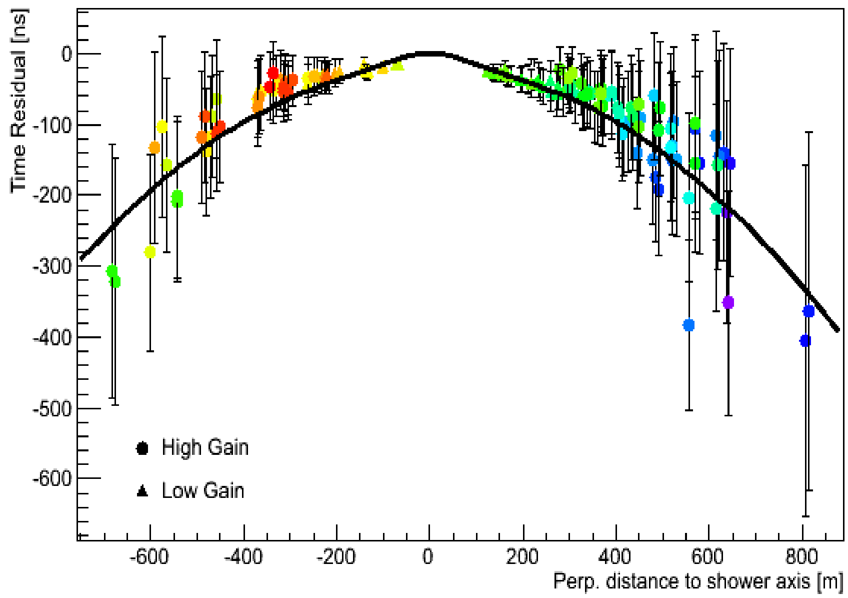

Figure 4.3: The time residual of the tank signals as a function of the distance to the shower axis. The distance is negative for hits that happened before the shower front crosses the core position.

S_i^{thr} is the charge threshold of the tank, S_i^{fit} is obtained at the center of a line joining the center of the two tanks in the station.

When the signal exceeds the saturation threshold of a tank (Section 2.2), the measured charge will be an underestimation of the real value. A saturation likelihood $\mathcal{L}_{sat}$ is introduced [46] to treat the saturated tanks separately,

$$\mathcal{L}_{sat} = \prod_i \int\limits_{\log_{10} S_{\mathrm{sat},i}}^{+\infty} \frac{1}{\sqrt{2\pi}\sigma_{q,i}} \exp\left(- \left(\frac{\log_{10} S_i - \log_{10} S_{\mathrm{exp},i}}{\sqrt{2}\sigma_{q,i}} \right)^2 \right) \mathrm{d} \log_{10} S_i, \tag{4.14}$$

where the product runs over all saturated tanks. This term has been studied in detail in [46].

In the case of standard showers, the likelihood function is seeded with the two first guesses for the core and direction reconstruction, then the likelihood minimization was done in several iterations to improve the stability of the fit. In the first iteration, the shower direction is fixed and the shower core, S_{ref} and β are used as free parameters. In the second iteration, the direction is released to fit the shower front curvature. In the last iteration, the direction is fixed again and the fit is repeated.

The number of stations is small in the case of the small showers and might not have enough degrees of freedom for the LDF fit with a curved shower front. Therefore, the shower direction information was fixed and used directly from the first guess reconstruction, and the likelihood minimization was done in only one step.

4.2 Snow Correction

Although the deployed level of IceTop tanks is the same as the snow surface, snowdrift, caused by prevailing wind, buries IceTop tanks over-time under a snow layer which attenuates the electromagnetic signal of the air shower. Moreover, tanks deployed in earlier years have more snow than those deployed in the last season. Therefore, the amount of accumulated snow on top of IceTop tanks is different from tank to tank (Section 2.4.2). The charge of the detected particles in the IceTop tank will be affected by the accumulated layer of snow and this will directly affect the reconstructed parameters of the air shower. The expected signal measured by IceTop S_{exp} is the main parameter used by various IceTop analyses [46] [99] [97] and will be used to reconstruct the energy of the primary particle for this analysis. Therefore, a snow correction procedure for the electromagnetic component is introduced to correct the expected signal S_{exp} [99]. The correction uses the snow height on top of the tanks and the attenuation length in snow to compensate for the attenuation on the measured signal,

$$S_{corr} = S_{meas} \cdot \exp\left(\frac{d_{snow} \sec\theta}{\lambda_{eff}}\right), \tag{4.15}$$

with S_{corr} is the corrected signal, S_{meas} is the measured signal, d_{snow} is the monthly snow height measured for 2011 data and λ_{eff} is the effective attenuation length in the snow.

The strategy of the snow correction is based on dividing the IceTop array into two parts. The first part contains all stations deployed before 2009, up to IC59, and will be called ″old array″. The

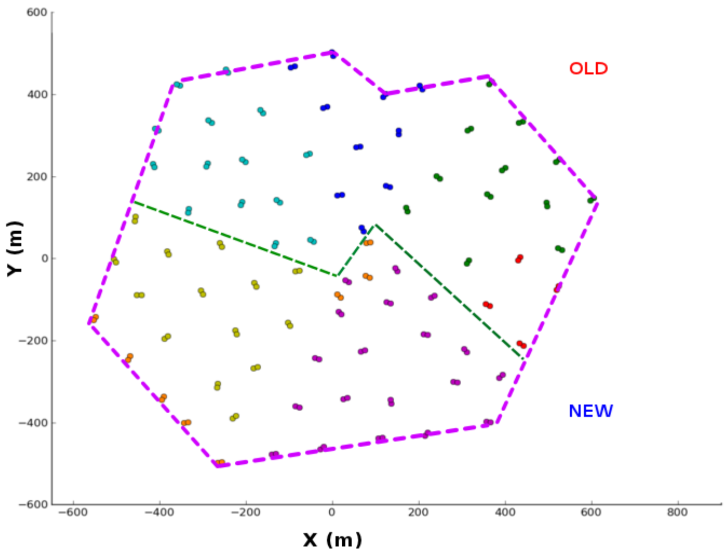

Figure 4.4: The IceTop detector is divided into two parts with the green dashed line. The old array includes all stations deployed before 2009 and the new array includes the remaining stations.

second part includes the stations deployed later than 2009 and will be called ″new array″. Because IceTop tanks in the old array are deployed earlier, a larger amount of snow is on top of the tanks in the old array than the new array (Section 2.4.2). Therefore, without the snow correction, the expected signal in the old part will be more attenuated than the signal in the new part, and this results in two different S_{exp} spectra. After applying snow correction with the correct snow attenuation length, the expected signal should agree between both arrays.

Figure 4.5a shows the expected signal spectrum obtained from the old and new arrays without snow correction. The shower size in the old array is more attenuated compared to the expected signal from the new array and the ratio between old and new spectra differs from one. After applying the snow correction (Figure 4.5b) with $\lambda_{eff} = 2.2$ m, a good agreement between the two shower size spectra is achieved (ratio plot around 1). A discrepancy is still observed at low energy ($\log_{10}(S_{exp}) < 0$). This is due to the high trigger efficiencies for showers in the old array. Moreover, events in the low energy part of the spectrum will be dominated by showers with the small shower selection (Section 5.1.1) which are more likely to be in the new part of the detector.

Close to the shower core, the detected signal is mainly produced by the electromagnetic component of the air shower, while the muonic component becomes dominant far away from the shower core. This dependence on the distance from the shower core is not taken into account in this correction. A more complicated correction accounting for the muonic component and the zenith dependance is still ongoing [100].

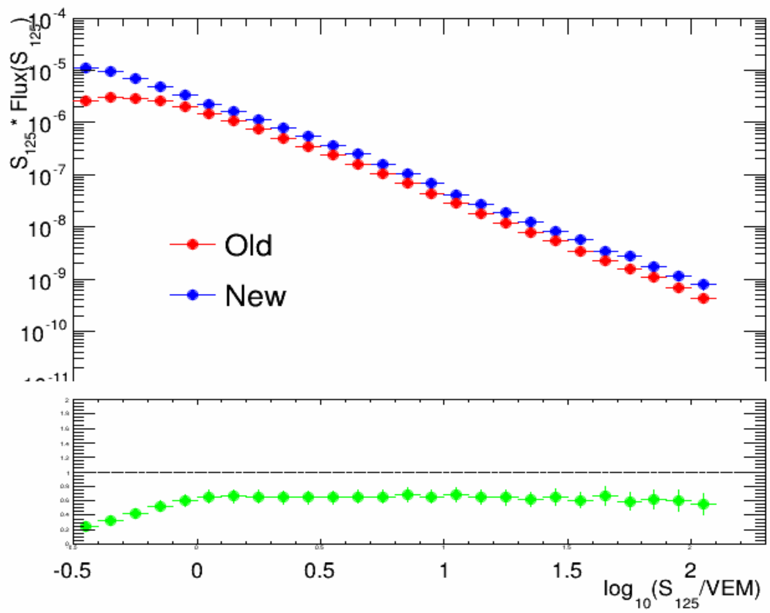

(a)

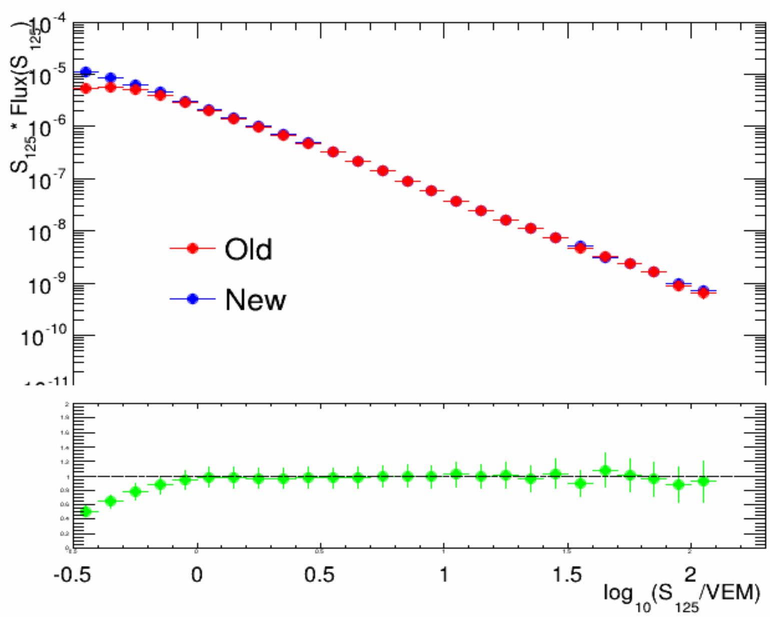

(b)

Figure 4.5: The shower size spectrum obtained from the old array compared to the one from the and new array. The lower plots represent the signal ratio of the old and new part. (a): The showers size spectrum before applying the snow correction. (b): The shower size spectra after snow correction with λ = 2.2 m.

Chapter 5

Event Selection and Energy Estimation

In this chapter, the method for event selection, the determination of primary energy, and the effective area will be discussed.

5.1 Event Selection

The data used in this analysis were taken in the period between May 13, 2011 and May 15, 2012, when the IceTop detector was running with its first year of 81 stations configuration, giving a detector livetime of about 331 days. The event selection process is based on the expected energy of the triggered events and the reconstruction performance. The goal of this analysis is to study the energy spectrum around the knee and to focus on the low energy part of the spectrum. Therefore, the event selection process ensures that we keep low energy events and that the selected events are likely to be well reconstructed.

5.1.1 Level 1

The level 1 selection was optimized to select events based on triggering and the geometry of the detector. Different selections are applied for low-energy and high-energy showers.

1. Low-energy showers:

    - InFill filter (IceTop_InFill_STA3): This filter is mainly designed to look at the 8 stations at the center of the detector (InFill stations) where the distance between stations is less than other IceTop stations in the rest of the IceTop array (See Section 2.2). Events which trigger a minimum of three InFill stations pass the InFill filter and are kept.
    - Events which pass the InFill filter with less than five InFill stations are required to have the triggered stations close to each other, because it can happen that the three stations required for the InFill filter are far away from each other. Such events are most likely to be noise and they will be badly reconstructed.
    - Events which pass the InFill filter with more than ten stations are also rejected because they are most likely to be high-energy events which can trigger the InFill filter and the STA3 filter and these events are kept in the next selection.

2. High-energy showers:

    - High-energy showers are defined as showers which do not pass the low-energy shower selection and pass the IceTop_STA3 filter. The IceTop_STA3 filter requires at least three IceTop stations to be triggered.

Events that pass the low-energy condition have energies less than few PeVs and are called later ″small showers″. Events which pass the high-energy condition are in the same energy range as detected showers with IceTop in previous seasons (without the InFill array). Therefore, they are called ″standard showers″.

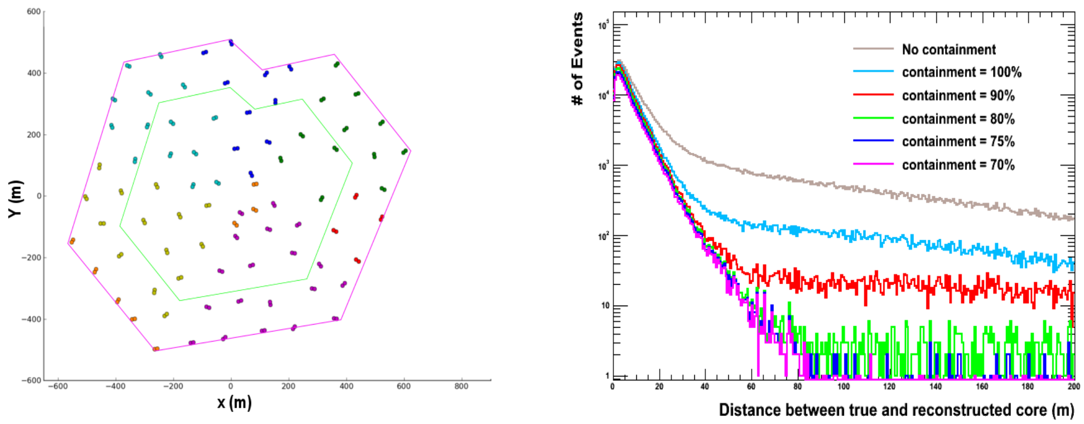

Figure 5.1: Left: The IceTop detector. The magenta line is a polygon connecting the outer stations and centered on the center of the detector. The green line represents 75 % of the polygon centered with the center of the center of the detector. Each dot on the surface represents one IceTop tank and different colors indicate different year of deployment. Right: Distance between the true and the reconstructed core position selected with different containment cuts, using simulation of proton shwers.

5.1.2 Level 2

This level is applied to ensure the good quality of the reconstruction. Cuts were optimized using simulations, then applied to check the experimental data.

1. IceTop containment: The containment cut is defined as a polygon (Figure 5.1) of 75% of the surface area of the IceTop detector and centered on its center. The reconstructed shower core is required to be included in the polygon area (green line in Figure 5.1). Events with the reconstructed shower core outside the detector can still trigger some stations on the outer boundary of the IceTop array. As a consequence, those events have the largest signal close to the reconstructed core position outside the IceTop array. Contained events have a much better core position reconstruction (Figure 5.1.right). Therefore, 25% of the surface area was

removed from the boundary of the IceTop array to exclude events with the reconstructed shower core on the edge or outside the detector. A study to include the uncontained showers in the reconstruction process is currently ongoing.

2. Successful fit: This means that the minimizer of the lateral fit found a converging point. Otherwise, the reconstruction fails and the event is excluded.

3. Direction: In order to include the zenith dependence in the analysis, events are selected, based on their arrival direction, in two zenith bands:
   Ω_1: 0.9 $<\cos(\theta) \leq$ 1.0 , which corresponds to a zenith angle $[0° - 26.8°]$.
   Ω_2: 0.8 $<\cos(\theta) \leq$ 0.9 , which corresponds to a zenith angle $[26.8° - 36.9°]$.
   This makes the studied zenith angle between 0° and 37°. Air showers with larger angles will not be included in the analysis because of the bad angular and core resolution. A study to improve the reconstruction for inclined showers can be found in [96].

4. The slope β: The slope of the lateral fit has to be between 1.6 and 4.5, because most events with a slope outside this range are not well reconstructed.

5.2 Effective Area

The effective area is an important variable to describe the efficiency of the detector for detecting air showers. It is calculated from Monte Carlo simulations for proton and iron showers after applying the event selection and the quality cuts:

$$A_{eff} = \frac{N_{rec}}{N_{gen}}.A_{gen} \tag{5.1}$$

where N_{rec} is the number of reconstructed events which remain in the final sample after all cuts, N_{gen} is the number of generated events in simulations, and A_{gen} is the generation area.

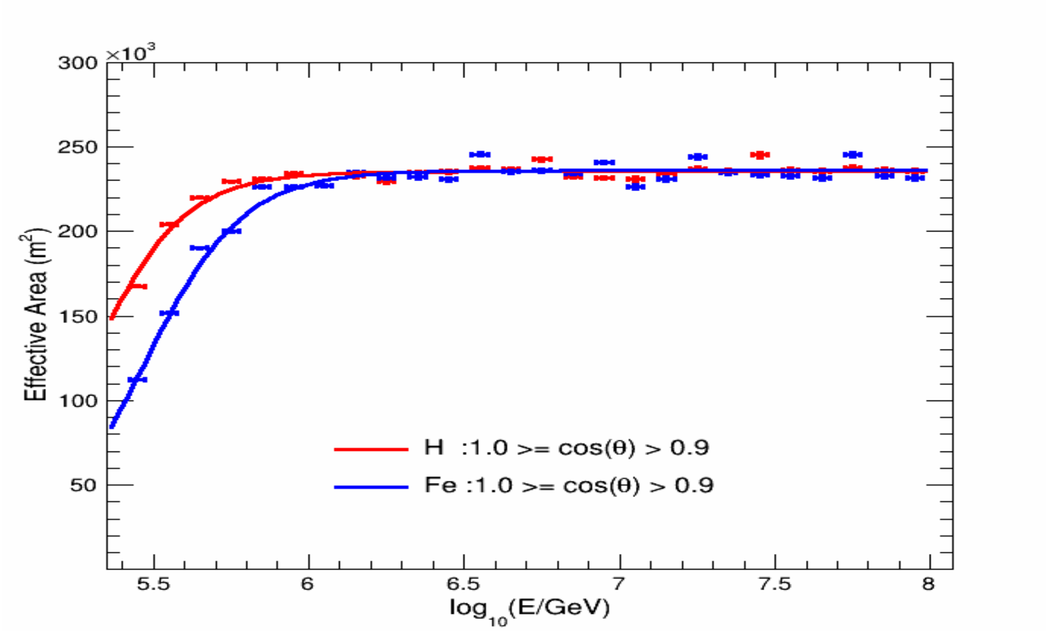

(a)

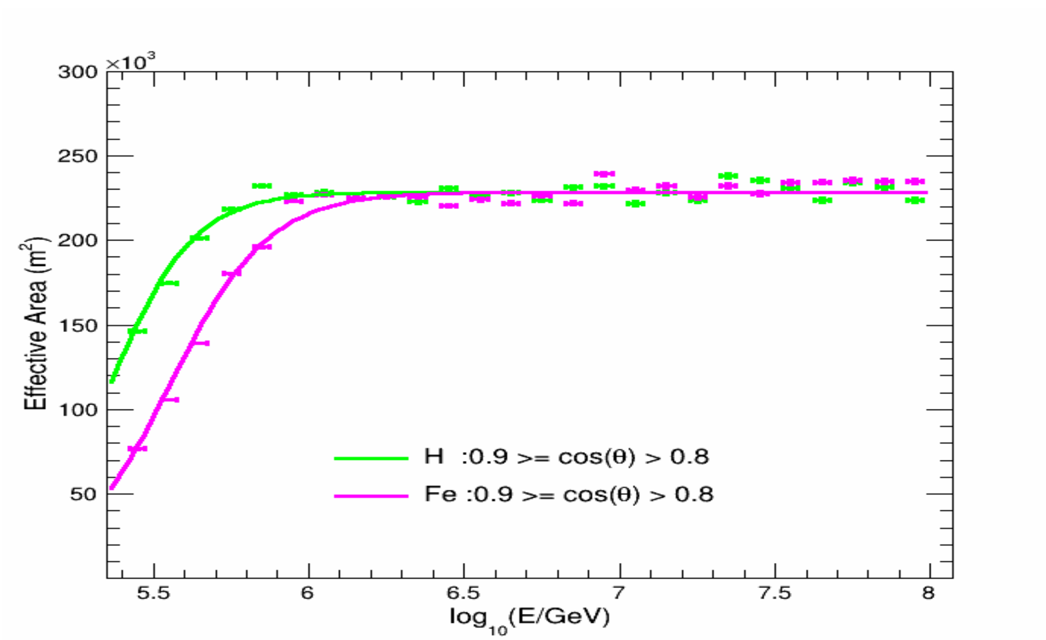

(b)

Figure 5.2: The effective area as a function of energy for proton and iron induced showers after all cuts. Proton is in red and iron in blue for Ω_1 while proton is in green and iron in pink for Ω_2. All curves are fitted with a sigmoid function 5.2.

Figure 5.2 shows the effective area for proton and iron induced air showers as a function of energy. For energies lower than 100 PeV, the effective area increases rapidly with energy before it becomes constant at higher energies. The energy threshold is higher for iron shower than for proton showers. This is due to the different interaction point in the atmosphere for different primaries. Iron showers start interacting higher in the atmosphere and showers are in a different stage of development at the detector level. This makes the probability for showers to reach the detector level and trigger at low energy to be smaller for iron than for proton showers. Therefore, the effective area is at maximum and flat starting from 500 TeV for proton showers and from 1 PeV for iron showers. The effective area is fitted with a sigmoid function for each primary:

$$A_{eff} = \frac{p_0}{(1 + exp(-p_1 \log_{10} E + p_2))}, \tag{5.2}$$

with p_1, p_2 and p_3 the fit parameters shown in Table 5.1. They will be used for the energy spectrum calculations.

Event Selection	Proton		Iron	
	Ω_1	Ω_2	Ω_1	Ω_2
p_0	(2.35 ±0.003) · 10^5	(2.29 ±0.002) · 10^5	(2.36 ±0.003) · 10^5	(2.29 ±0.003) · 10^5
p_1	6.6 ± 0.41	7.34 ± 0.37	6.19 ± 0.22	6.29 ± 0.29
p_2	34.9 ± 2.2	39.5 ± 2.0	33.8 ± 1.2	35.0 ± 1.6

Table 5.1: Parameters of the sigmoid fit for proton and iron primaries, and the two zenith bands Ω_1 and Ω_2.

Figure 5.3 shows the effective area in two zenith bands for proton and iron induced air showers. For more inclined showers, the amount of atmosphere that showers need to traverse before arriving at the detector is larger than for more vertical showers. Therefore, inclined showers will be more attenuated in the atmosphere and this results in a lower effective area and a higher energy threshold for inclined showers than vertical showers.

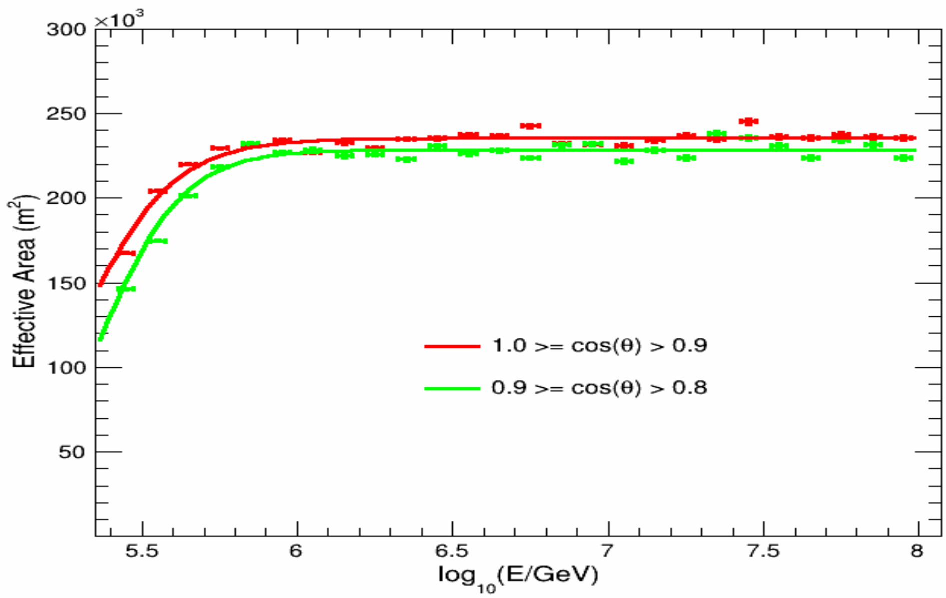

(a) Proton

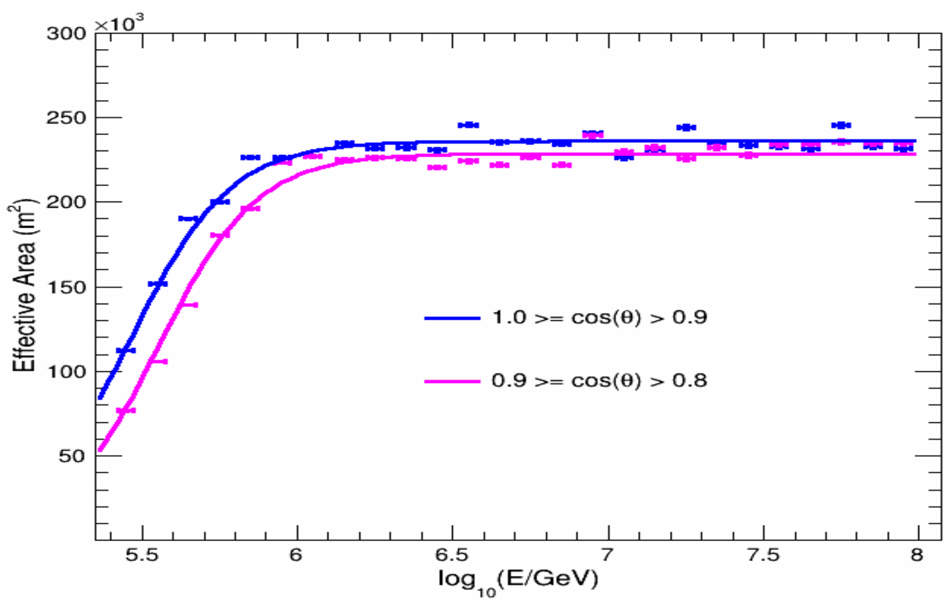

(b) Iron

Figure 5.3: The effective area as a function of energy for proton (a) and iron (b) induced showers in the two studied zenith bands. Proton is shown in red and green while iron is shown in blue and pink, for Ω_1 and Ω_2 respectively.

5.3 Performance

To check the quality of the reconstructed variables, the core and angular resolution for proton and iron induced showers are studied (Figure 5.4). It is expected that the resolution gets worse at low energy (below 6.5 in $\log_{10}$ E), because of the small number of triggered stations at low energy which makes it harder to precisely reconstruct the core and the direction of the air shower [101].

The core resolution is defined as 68% of the cumulative distribution of the distance between the reconstructed track and the true track on the surface. As it can be seen in Figure 5.4a, the core resolution is about 20 m in the worst case at low energy. This value improves significantly for energies above 3 PeV ($\approx$ 6.5 in $\log_{10}$E) where the core resolution is always less than 10 m (6 m at the highest energy bins). Due to their early interaction in the atmosphere, iron showers will be more attenuated and less stations will be triggered at the same energy. This results in a worse core resolution for iron showers than for proton showers. A core resolution between 6 and 22 m is achieved over the entire energy range.

The angular resolution is defined as 68% of the cumulative distribution of the angle between the reconstructed track direction and the true track direction. The angular resolution achieved is better than $0.5°$ at energies $E > 3$ PeV while it gets worse at low energies (around $1.4°$). The worse resolution at low energy is expected since the reconstructed direction is used from the first guess reconstruction (see Section 4.1.2). An angular resolution between $0.5°$ and $1.4°$ is obtained for the studied energy range.

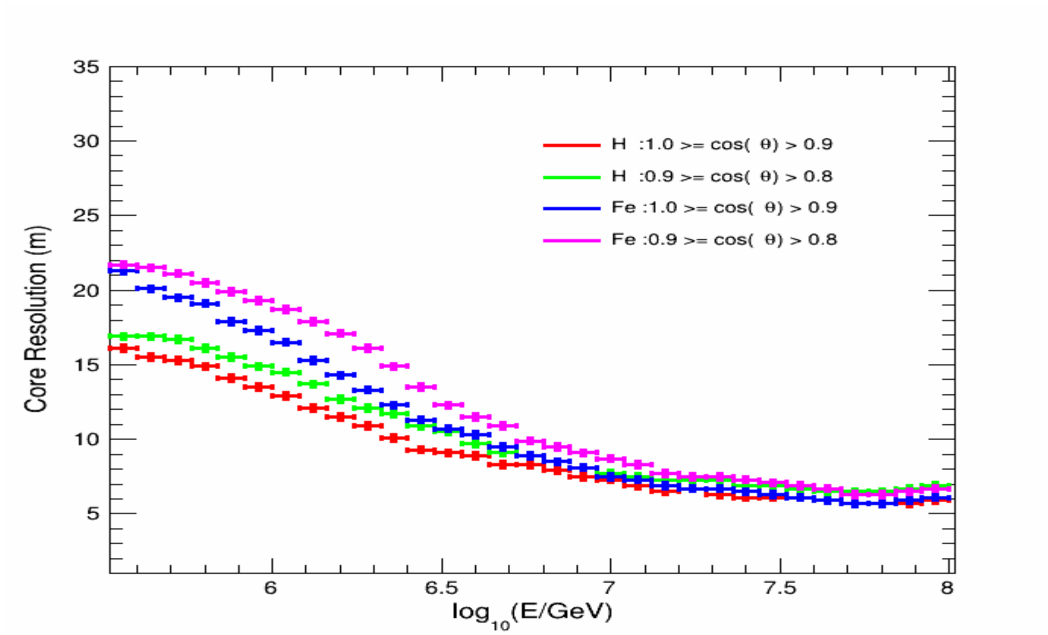

(a)

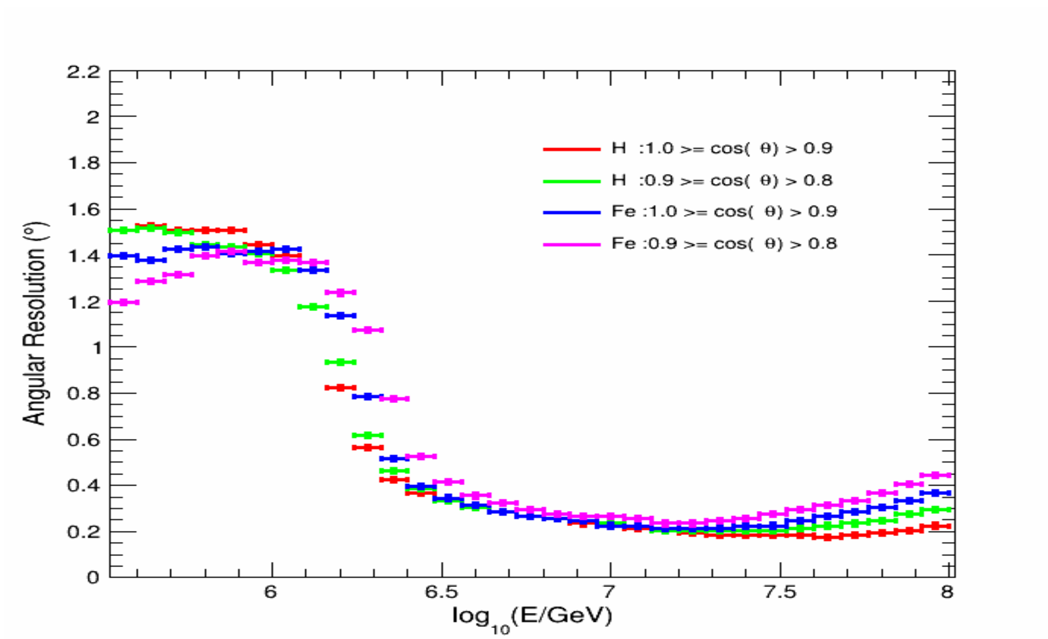

(b)

Figure 5.4: The core (a) and angular (b) resolutions as a function of energy for proton and iron induced showers in the two studied zenith bands (Ω_1 in red and blue, and Ω_2 in green and pink).

5.3.1 Data MC Comparison

Before the variables obtained from the Monte Carlo simulations can be used to reconstruct the energy, they have to be verified with experimental data to be sure that they are well describing the data. Here I will show a comparison between the most important variables that have been used in the analysis, for proton and iron simulations and experimental data. Distributions are scaled to 1 because the number of events between data and simulation is different.

Shower Size S_{exp}:

The shower size S_{exp} is an important parameter for the analysis since it is used for estimating the energy of the primary cosmic ray particle. Simulated and measured shower sizes in the zenith range of the analysis (0.8 $<\cos\theta$ $<$1.0) are shown in Figure 5.5. Distributions of the shower size for showers selected with the standard showers selection ($\log_{10}(S_{125})$ in Figure 5.5a) and with the small showers selection ($\log_{10}(S_{80})$ in Figure 5.5b) show a good shower size agreement between data and Monte Carlo.

The Slope β:

Figure 5.6 shows the distribution of the slope of the lateral fit β. The parameter β was limited to a range 1.6 $<\beta<$4.5 in order to exclude badly reconstructed events on the borders of the distribution. β behaves differently for proton and iron primaries because it depends on the longitudinal development of the shower. However, the data fall between proton and iron induced simulated showers. Since β was not used as a parameter for primary energy or primary mass, it was not studied any further.

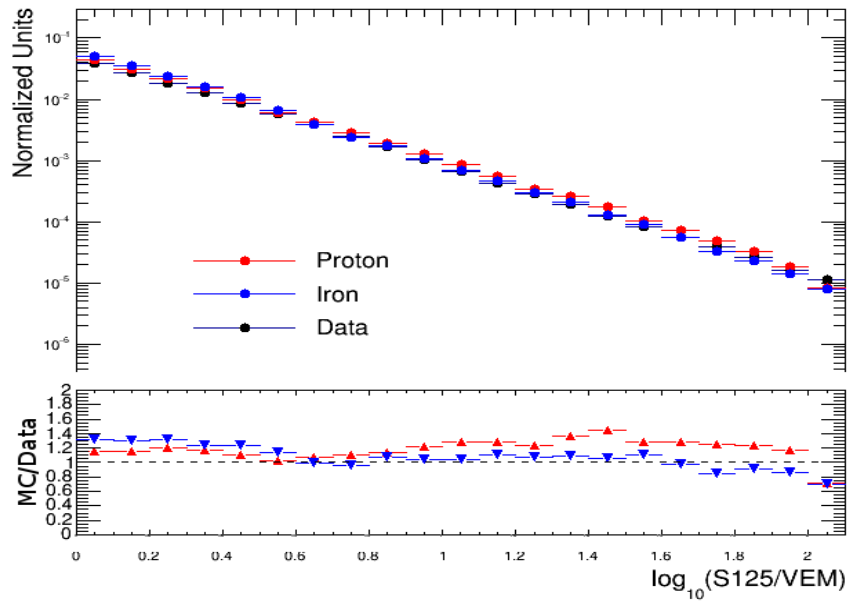

(a)

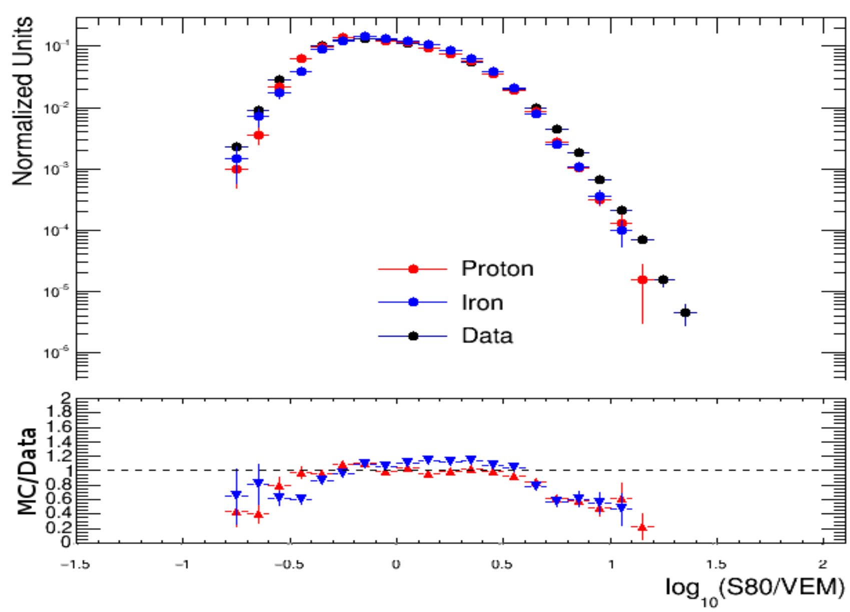

(b)

Figure 5.5: The measured and simulated distributions of the shower size in data and Monte Carlo. For standard showers (a) and for small showers (b).

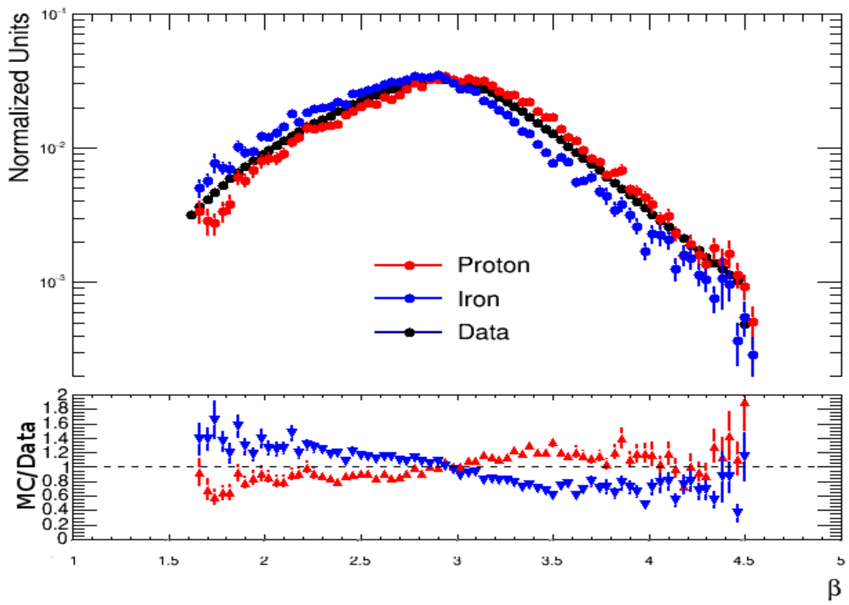

Figure 5.6: The distribution of the lateral fit slope β in data and simulations.

Zenith and Azimuth:

The reconstructed zenith distribution from data, proton, and iron showers is shown in Figure 5.7a. The distribution of experimental data lies in between the two extreme masses within statistical uncertainties. Figure 5.7b shows a comparison for the reconstructed azimuth angle distribution in data and simulations. The variation in the proton and iron distributions is due to the low amount of statistics compared to the data, but the distributions are flat and the ratios always around one.

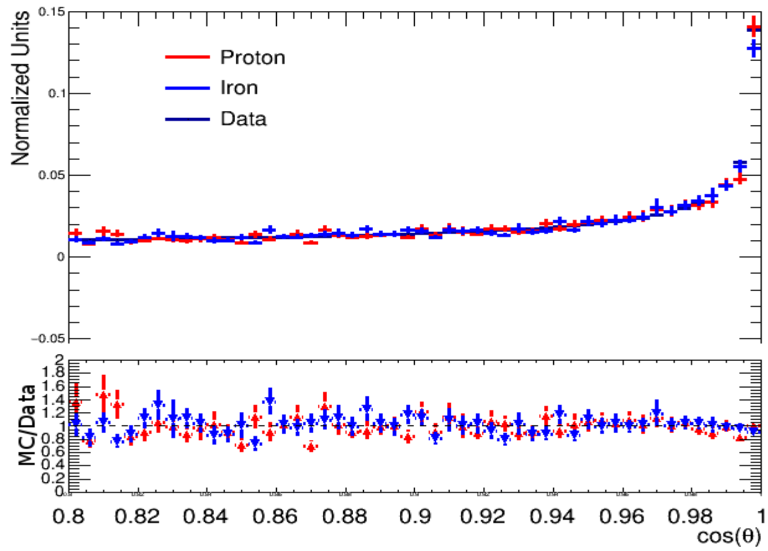

(a)

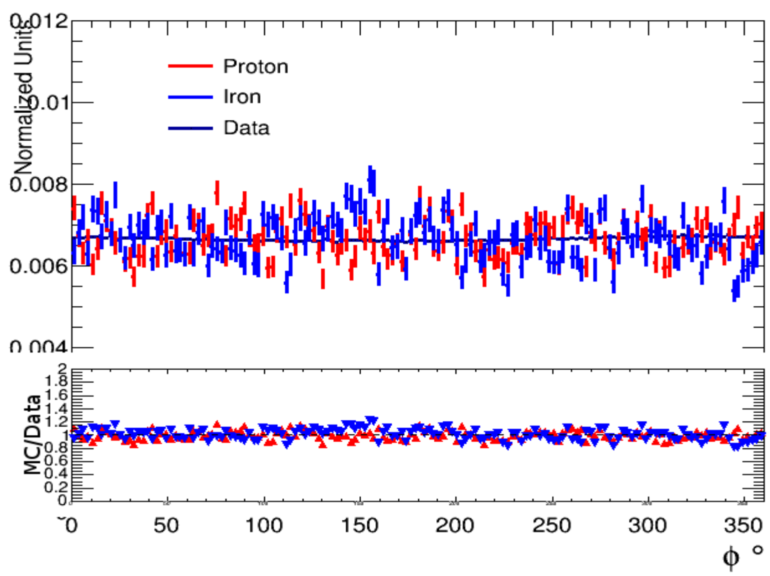

(b)

Figure 5.7: The distribution of the cosine reconstructed zenith angle (a) and the reconstructed azimuth angle (b) from data and Monte Carlo simulations.

Number of Stations:

The number of triggered stations depends on the primary energy and composition of the primary cosmic ray particle. Figure 5.8 shows the number of HLC stations participating in IceTop events for data and simulations. The data lies in between Proton and Iron as expected. .

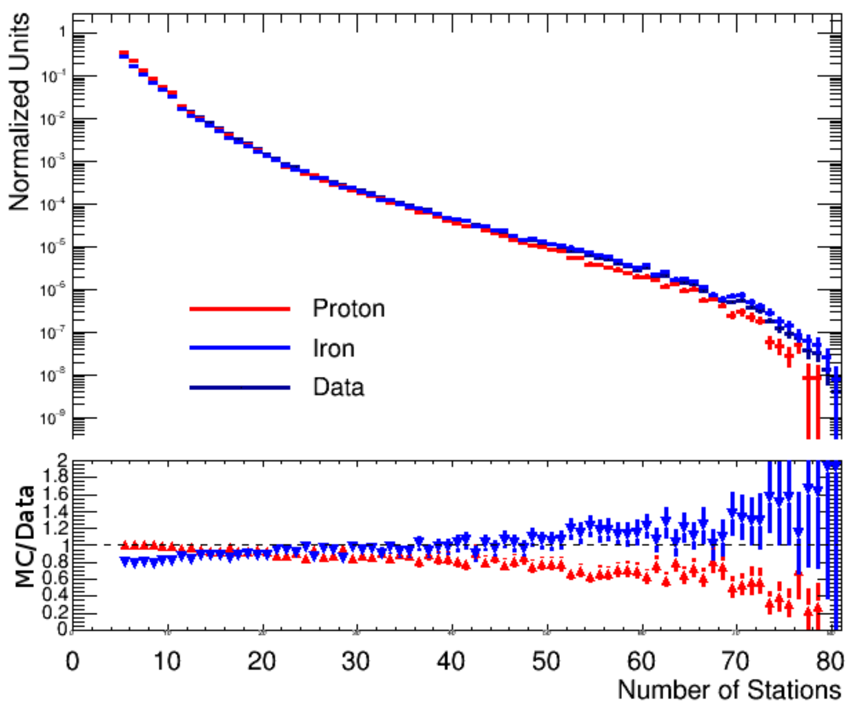

Figure 5.8: The number of HLC stations that participate in IceTop events for data and simulations.

5.4 Determination of the Primary Energy

The relation between the expected signal and the true primary energy from simulation is used to estimate the energy of the primary cosmic ray particle. Since the expected signal depends not only on the energy but also on the mass of the primary particle and the zenith angle θ of the air shower, the energy conversion is determined using proton and iron simulations in two zenith bands. Figure 5.9 and Figure 5.10 are two examples of expected signal as a function of the true primary energy for proton and iron simulations in the zenith band $0.9 < \cos(\theta) < 1.0$. Simulated proton and iron showers, in a given zenith band, were binned in $\Delta \log_{10}(S_{exp}) = 0.1$. For each interval, the distribution of the logarithm of the simulated primary energies $\log_{10}(E_{true})$ was fitted with a Gaussian. The mean of the Gaussian is taken as an energy estimate for showers in the respective $\log_{10}(S_{exp})$ interval. Examples of some of these energy distributions in several expected signal intervals are shown in Figure 5.11 for proton and iron showers and all distributions can be found in Appendix B .

The relationship between $\log_{10}(S_{exp})$ and $\log_{10}(E_{true})$ is fitted with a parabola:

$$\log_{10} E_{true} = p_0 + p_1 \log_{10} S_{exp} + p_2(\log_{10} S_{exp})^2. \tag{5.3}$$

The parameters p_0, p_1 and p_2 are the fit parameters and they depend on the zenith angle and the primary mass. This function is fitted separately to both distributions of $\log_{10}(S_{exp})$ vs $\log_{10}(E_{true})$ for proton and iron simulations and in the two studied zenith bands. A set of parameters, shown in Table 5.2 were obtained for each composition assumption and each zenith band for standard and small showers. These parameters were used to reconstruct the energy with the corresponding assumed composition.

Figure 5.12 shows the relation between the shower size and the primary energy for simulated proton and iron showers with a zenith angle $0.9 < \cos(\theta) < 1.0$ fitted with Equation. 5.3. This relation shows a clear dependence on the primary mass and it becomes less sensitive to the composition

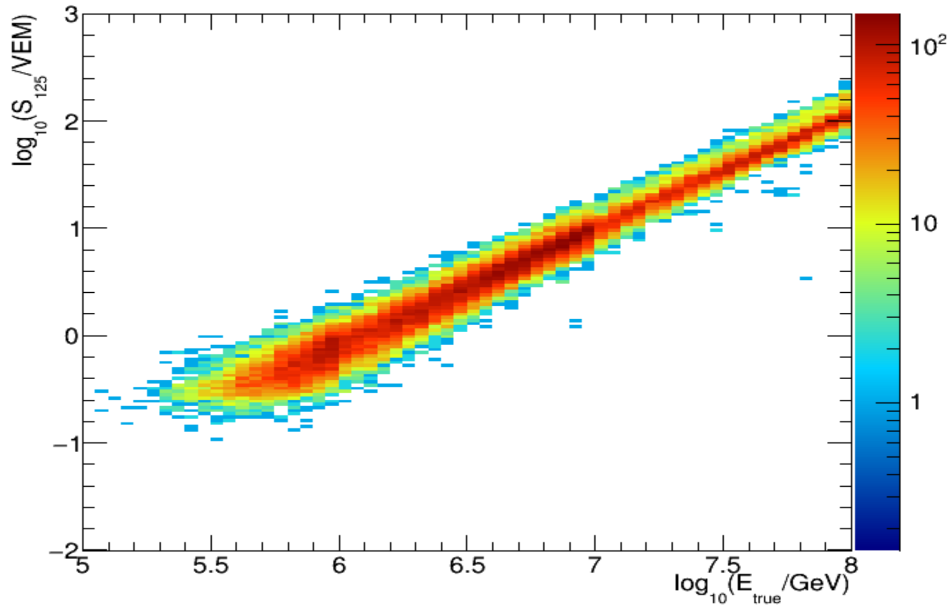

(a)

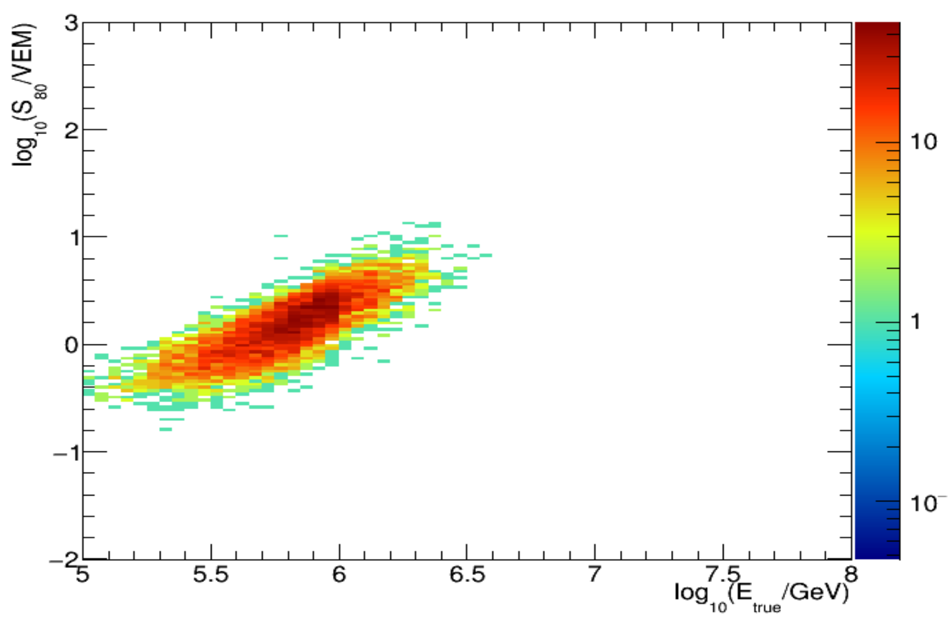

(b)

Figure 5.9: Distribution of the shower size S_{exp} as a function of true primary energy for proton showers with 0.9 $<\cos\theta<$1.0. The distribution from standard showers is shown in the top and from small showers in the bottom.

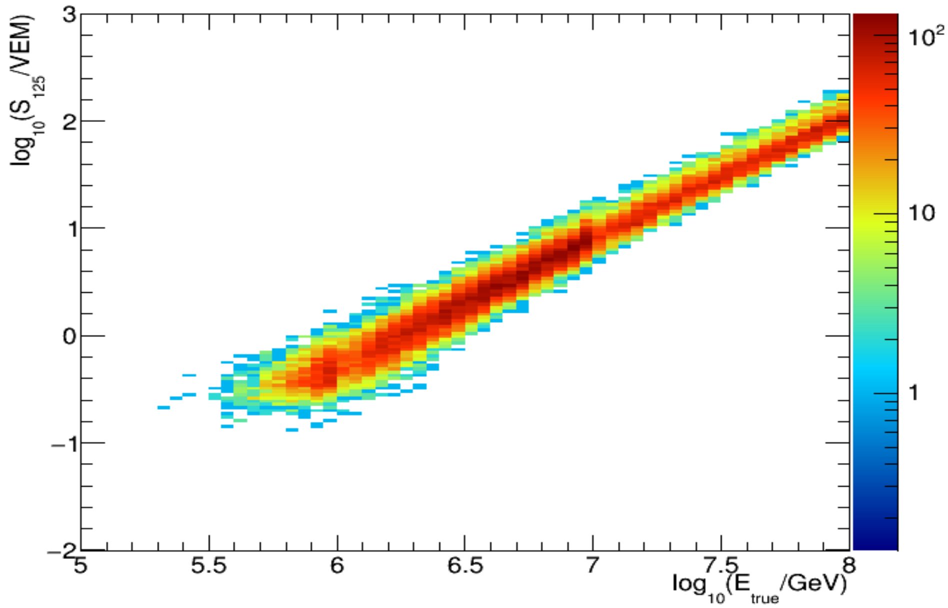

(a)

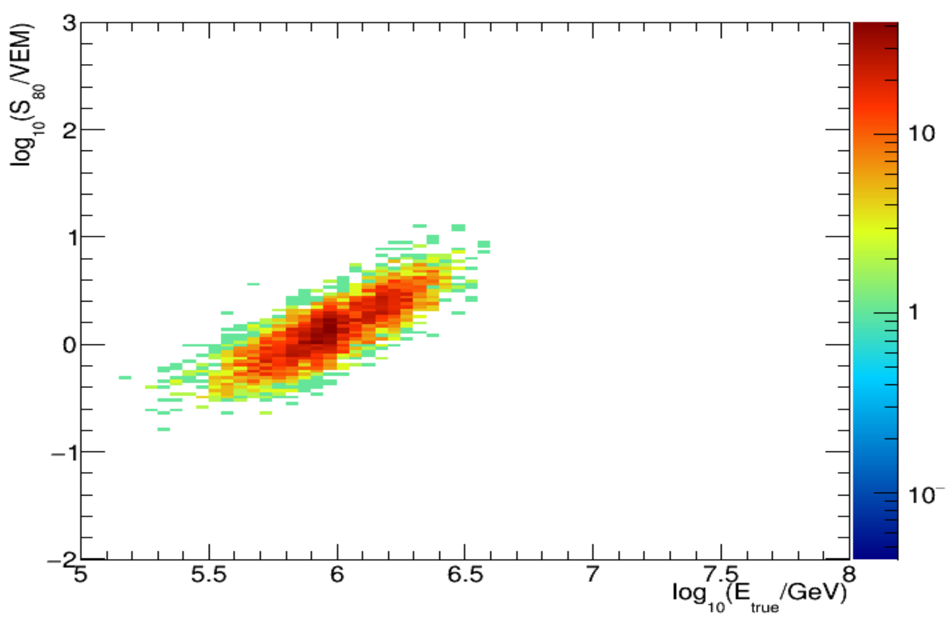

(b)

Figure 5.10: Distribution of the shower size S_{exp} as a function of true primary energy for iron showers with 0.9 $<\cos\theta<$1.0. The distribution from standard showers is shown in the top and from small showers in the bottom.

Event Selection	Standard Showers				Small Showers			
	Proton		Iron		Proton		Iron	
	Ω_1	Ω_2	Ω_1	Ω_2	Ω_1	Ω_2	Ω_1	Ω_2
p_0	$6.014 \pm 4.4 \cdot 10^{-4}$	$6.137 \pm 4.6 \cdot 10^{-4}$	$6.108 \pm 5.2 \cdot 10^{-4}$	$6.282 \pm 5.8 \cdot 10^{-4}$	$5.575 \pm 1.2 \cdot 10^{-3}$	$5.748 \pm 1.1 \cdot 10^{-3}$	$5.689 \pm 1.3 \cdot 10^{-3}$	$5.898 \pm 1.3 \cdot 10^{-3}$
p_1	$0.884 \pm 1.1 \cdot 10^{-3}$	$0.797 \pm 1.1 \cdot 10^{-3}$	$0.862 \pm 1.3 \cdot 10^{-3}$	$0.772 \pm 1.5 \cdot 10^{-3}$	$0.775 \pm 5.8 \cdot 10^{-3}$	$0.628 \pm 5.6 \cdot 10^{-3}$	$0.691 \pm 5.7 \cdot 10^{-3}$	$0.680 \pm 5.4 \cdot 10^{-3}$
p_2	$0.029 \pm 7.2 \cdot 10^{-4}$	$0.041 \pm 6.8 \cdot 10^{-4}$	$0.026 \pm 8.1 \cdot 10^{-4}$	$0.040 \pm 9.3 \cdot 10^{-4}$	$-0.114 \pm 8.9 \cdot 10^{-3}$	$-0.018 \pm 9.8 \cdot 10^{-3}$	$-0.048 \pm 1.1 \cdot 10^{-3}$	$-0.021 \pm 1.1 \cdot 10^{-3}$

Table 5.2: Parameters of the parabolic fit for proton and iron primaries, and the two zenith bands (Ω_1 and Ω_2).

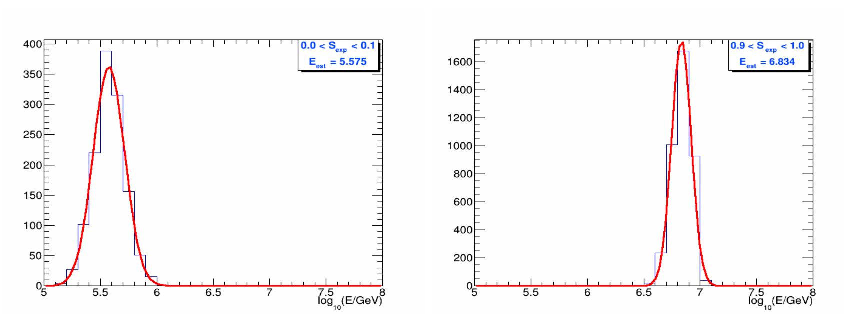

(a) Proton

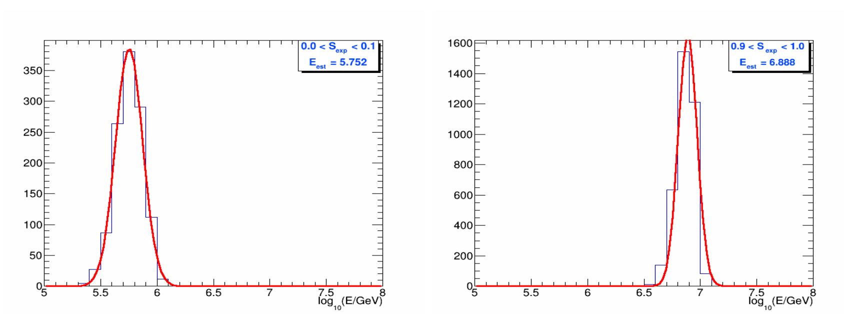

(b) Iron

Figure 5.11: True Energy distributions in two different shower size bins fitted to a Gaussian, for proton (a) and iron showers (b) and in a zenith band $0.9 < \cos(\theta) \leq 1.0$. Distributions for all shower size bins can be found in Appendix B.

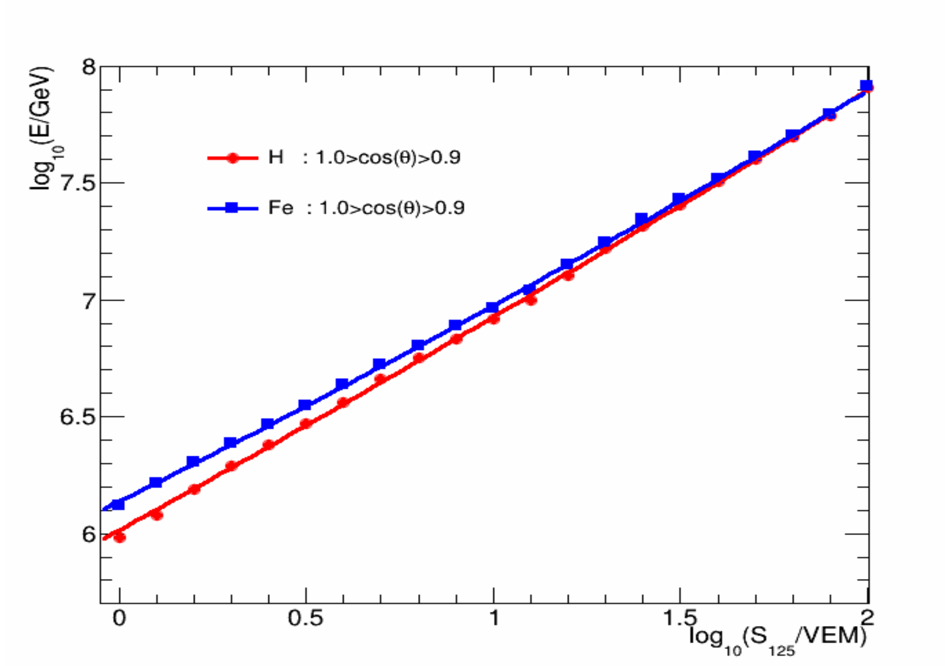

(a)

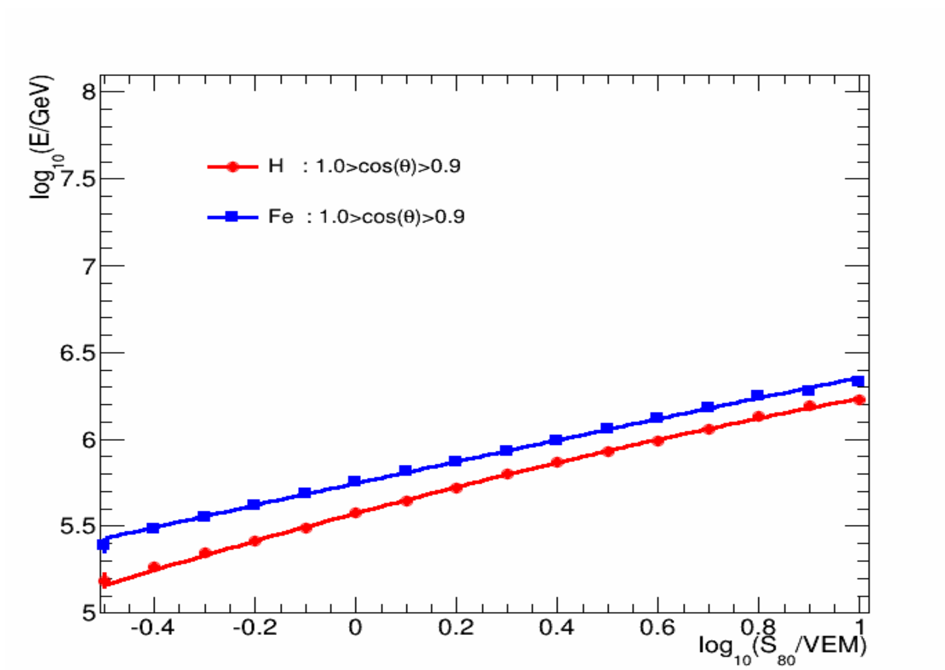

(b)

Figure 5.12: Distribution of the shower size S_{exp} as a function of true primary energy for proton showers compared to the distribution for iron showers, both fitted with a parabola in 0.9 $<\cos\theta$ $<$1.0. For standard (top) and for small showers (bottom).

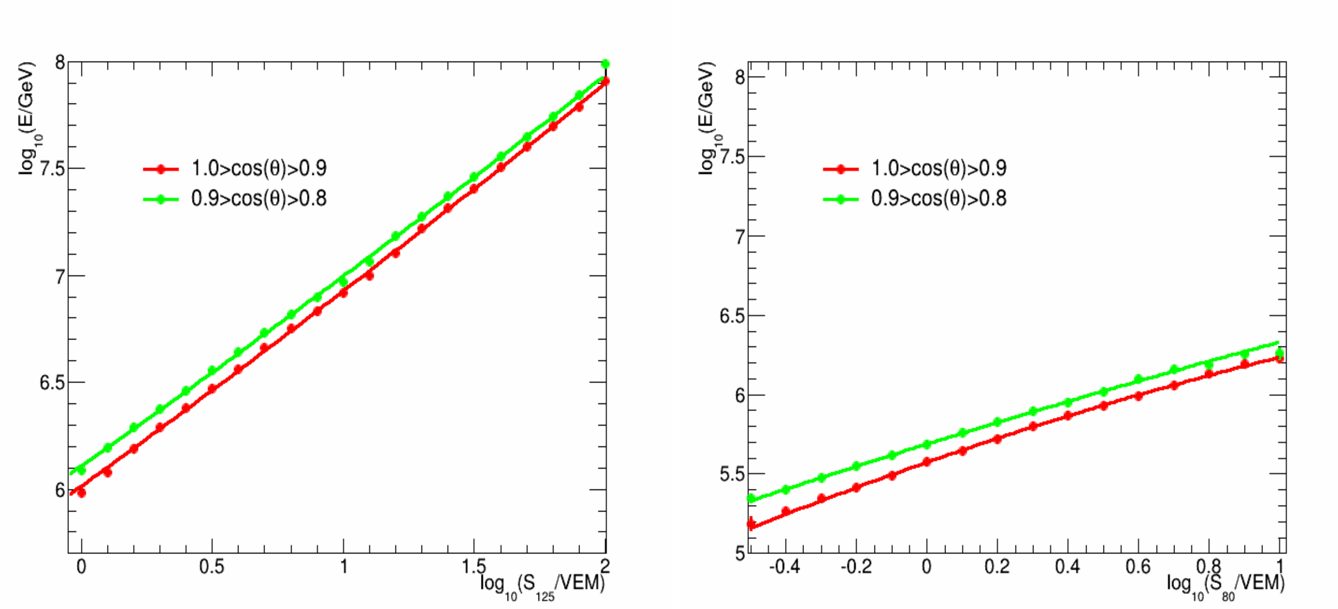

(a) Proton

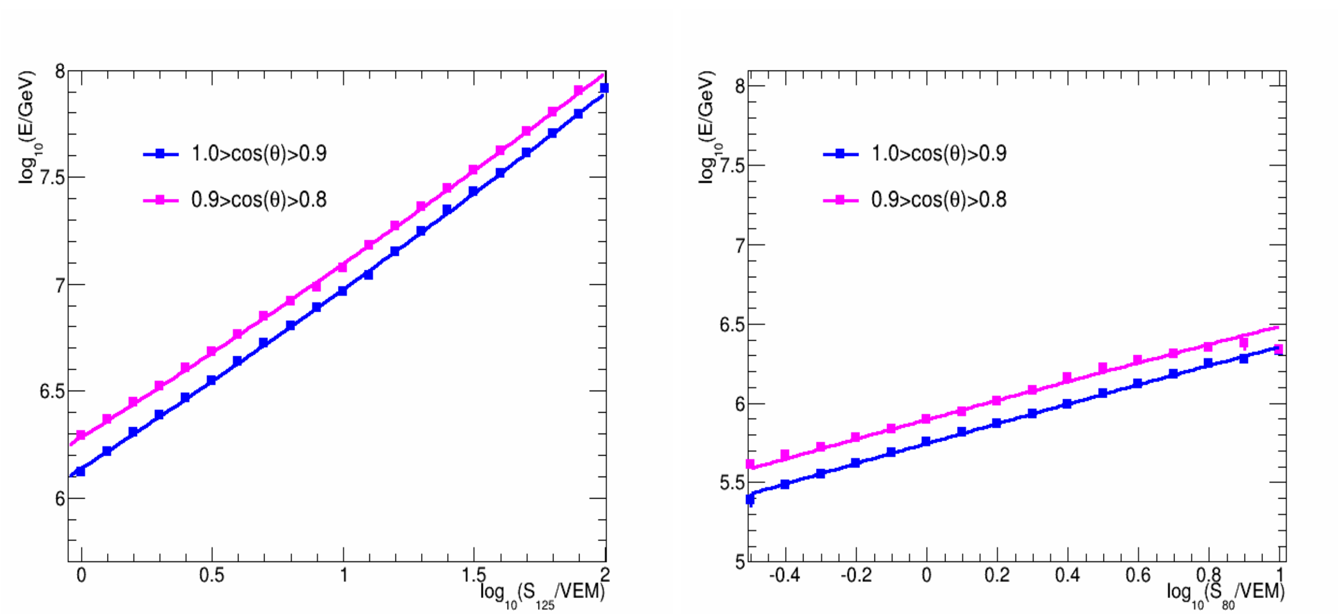

(b) Iron

Figure 5.13: Distribution of the shower size S_{exp} as a function of primary energy for proton (a) and iron (b) showers with a zenith angle ($0.9 < \cos(\theta) < 1.0$ and $0.8 < \cos(\theta) < 0.9$). Left for standard showers and for small showers on the right. All distributions are fitted with a parabolic function.

assumption at high energy. A comparison of the energy conversion for each primary separately is shown in Figure 5.13.

The parameters of the fit function (Equation 5.3) are shown in Table 5.2 and they are used to reconstruct the energy of the standard and the small showers selections. The obtained energy from both selections is combined in one histogram. Therefore, in the following, the reconstructed energy is representing showers from both selections.

5.4.1 Energy Bias and Resolution

The energy bias and resolution are studied using Monte Carlo simulations for proton and iron induced showers. They were checked to decide about the accuracy of the reconstructed energy. The fraction of the reconstructed and true energy is calculated:

$$\log_{10}(\Delta(E)) = \log_{10}\left(\frac{E_{reco}}{E_{true}}\right), \tag{5.4}$$

with E_{true} the true primary energy from Monte Carlo simulations and E_{reco} the reconstructed energy obtained using the fit parameters in Table 5.2. The energy bias is defined as the mean of these distributions, and the energy resolution $\sigma_{\Delta(\log_{10}(E))}$ is the RMS. Figure 5.16 shows a set of these fractional distributions for proton and iron and at different energy bins

The energy bias (shown in Figure 5.14) is very small almost over the entire energy range and much smaller than the energy resolution (Figure 5.15). The energy resolution starts at 10% for energies above 1 PeV ($\log_{10} E = 6.0$) and it becomes less than 5% beyond 10 PeV ($\log_{10} E = 7.0$), The increase of the energy resolution at low energy is due to the bad core and angular resolutions and to the shower-to-shower fluctuation. In the other hand, the energy resolution for air showers in the zenith band $0.9 < \cos(\theta) < 1.0$ (more vertical) is better than the resolution in the zenith band $0.8 < \cos(\theta) < 0.9$ (more inclined). This is due to the better reconstruction and less attenuation in the atmosphere for more vertical air showers.

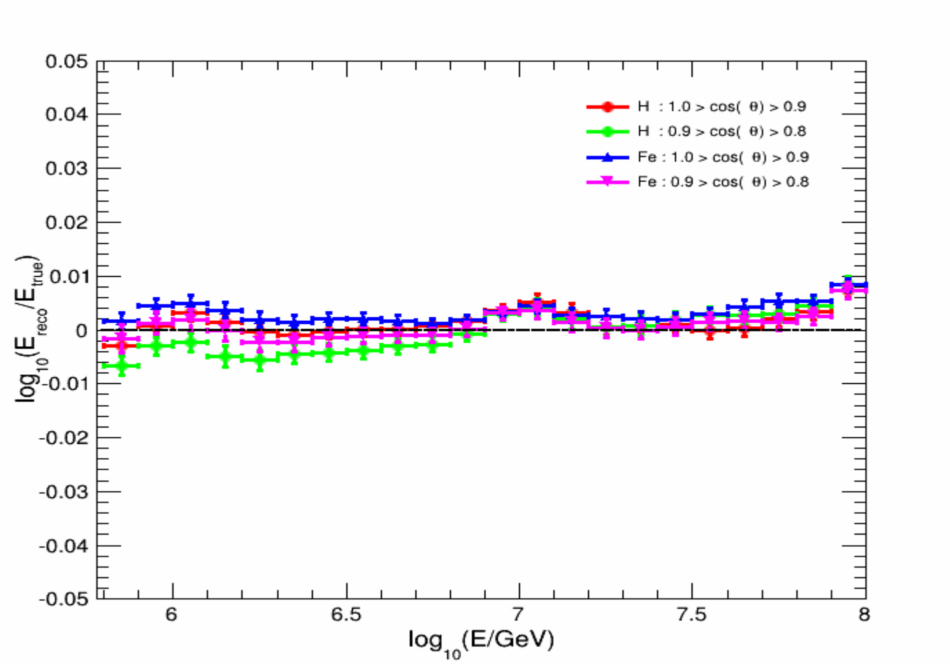

Figure 5.14: The energy bias as a function of reconstructed energy for proton and iron showers in the two studied zenith bands.

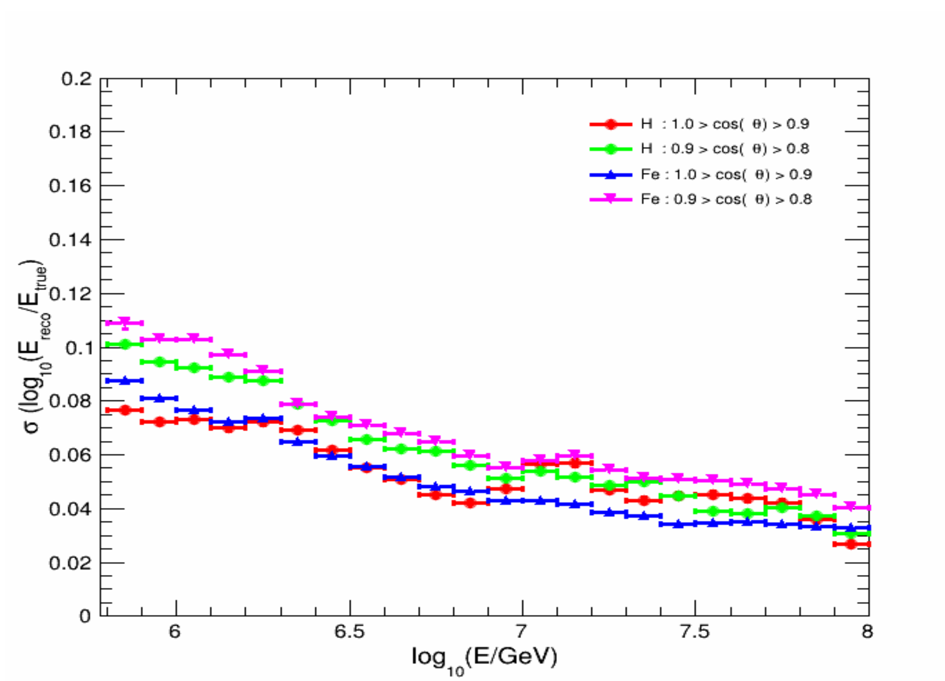

Figure 5.15: The energy resolution as a function of reconstructed energy for proton and iron showers in the two studied zenith bands.

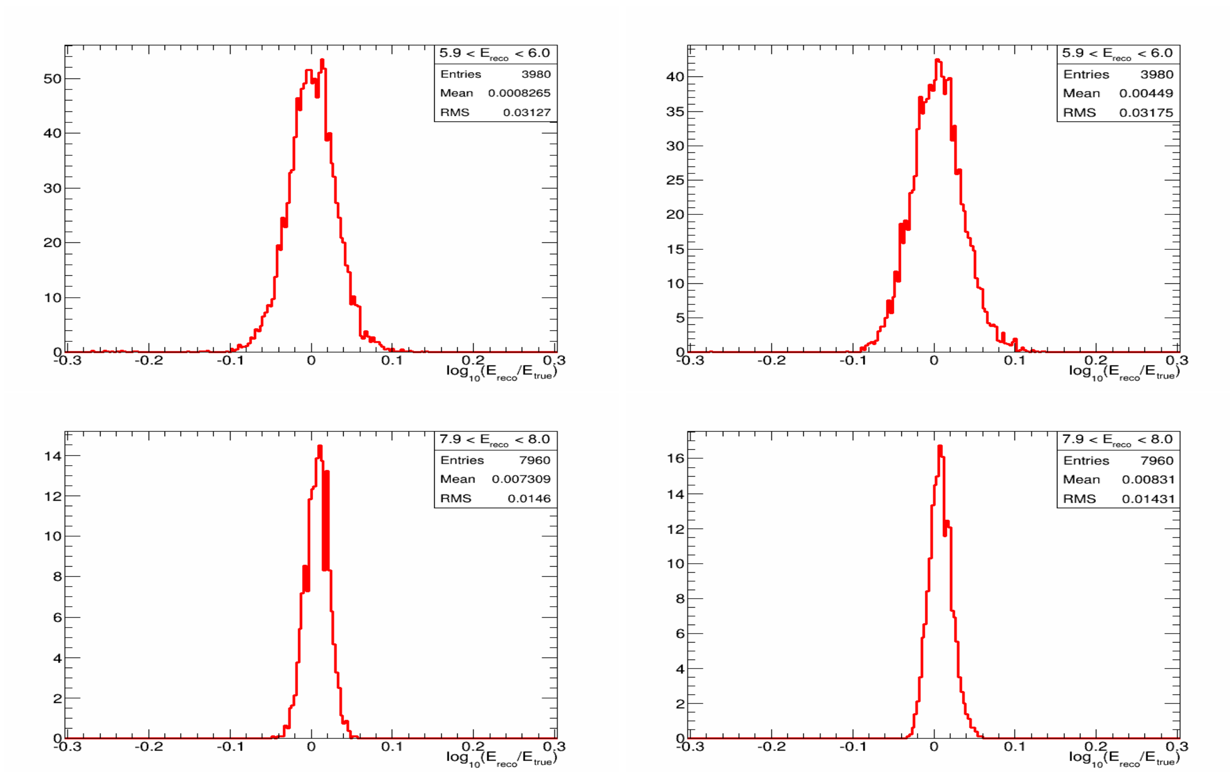

Figure 5.16: Set of fractional distributions of true and reconstructed energy for proton (left) and iron (right) showers with a zenith angle $0.9 < \cos(\theta) \leq 1.0$. The energy bias and resolution are considered as the mean and RMS of these distributions, respectively. Similar distributions for all energy bins can be found in Appendix C.

Chapter 6

Energy Spectrum

The objective of this analysis is to determine the cosmic ray energy spectrum in the energy range between a few hundred TeV and 100 PeV. In the previous chapter, the technique used to derive the primary energy of the cosmic ray particle by converting the expected signal parameter S_{exp} into energy, has been discussed (Figure 5.12).

In this chapter, I will explain the calculation used to derive the energy spectrum, discuss the possible systematics that can affect the measurement and present the results of the cosmic ray energy spectrum with the IceTop detector.

6.1 Flux Determination

The energy spectrum is defined as the number of cosmic ray particles N per unit time t, per unit solid angle Ω, per unit area A, and per unit energy E. The flux is calculated as,

$$J(E) = \frac{1}{t \cdot \Omega \cdot A_{eff} \log(10)} \frac{\mathrm{d}\,N}{\mathrm{d}\log_{10} E} \tag{6.1}$$

where t is the livetime of the detector for the studied data taking period, Ω is the solid angle, A_{eff} is the effective area, and $\frac{\mathrm{d}\,N}{\mathrm{d}\log_{10}E}$ is the number of events per energy bin (E is obtained from Equation 5.3).

To calculate the livetime t of the detector, an exponential function (Equation 6.2) is fitted to the distribution of time differences between successive events (Δt) for each month. The exponential decay constant (1/τ) is the average trigger rate for that month.

$$N(\Delta t) = N_0 \cdot e^{-\Delta t/\tau}, \tag{6.2}$$

Then the livetime is calculated by multiplying τ with the total number of events $t = \tau \cdot N$. The livetime for the selected data taking period (between May 13, 2011 and May 15, 2012) is t = 331.78 ± 0.3 days. The uncertainty in the livetime comes from the error in τ.

The simulated solid angle Ω is the zenith angle distribution caused by the atmospheric attenuation integrated over the solid angle dΩ:

$$\begin{aligned}\Omega &= \int\int \cos(\theta)\sin(\theta)\,\mathrm{d}\,\theta\,\mathrm{d}\,\phi = \int\int \cos(\theta)\,\mathrm{d}\cos(\theta)\,\mathrm{d}\,\phi \\ &= 2\pi \int \cos(\theta)\,\mathrm{d}\cos(\theta),\end{aligned} \tag{6.3}$$

with θ the zenith angle and the term 2π represents the generated azimuth angle ϕ. This results in a solid angle Ω = 1.131 sr for the zenith angle ($0° - 37°$) used in the analysis.

The effective area is obtained from the sigmoid fit function in Equation 5.2 and the parameters of the fit obtained in Table 5.1. A cut on the energy threshold is applied at 500 TeV for proton assumption and at 1 PeV in the case of iron assumption.

The energy spectrum can then be calculated using the energy conversion form Equation 5.3, the effective area from Equation 5.1, and the livetime and solid angles values. Figure 6.2 shows

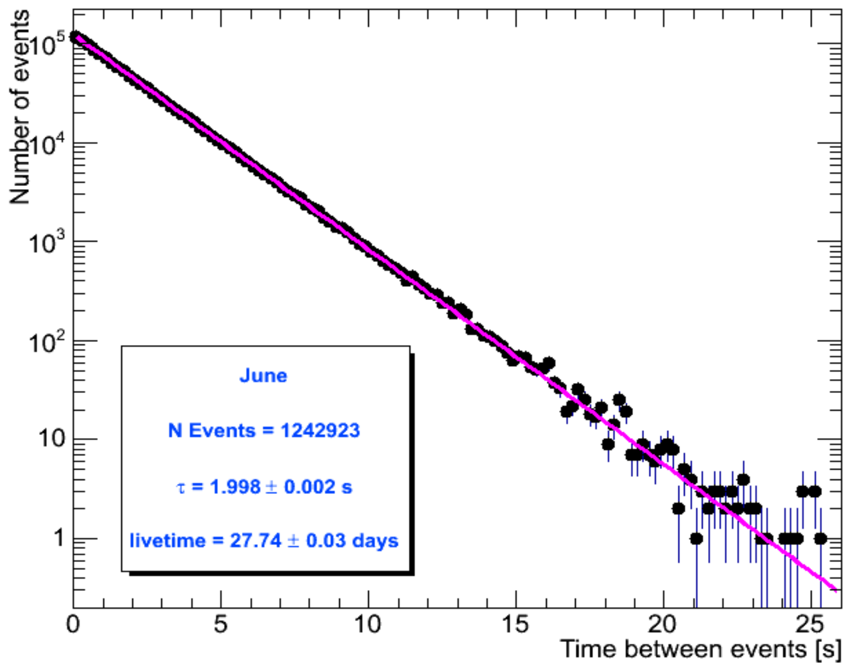

Figure 6.1: An example of the livetime of the detector during June 2011. Plots for all months are given in Appendix D

the cosmic ray energy spectrum measured for different zenith bands ($0.8 \le \cos(\theta) < 0.9$ and $0.9 \le \cos(\theta) \le 1.0$) with proton and iron assumption. Since, cosmic rays come isotropically from all directions of the sky, spectra from different zenith bands should agree. The measured energy spectra from different zenith bands do not agree because of the zenith dependence on the composition assumption used to derive the energy spectrum. The amount of atmosphere that showers need to traverse before detecting them on the IceTop detector is larger for more inclined showers than for more vertical showers. The first interaction in the atmosphere for iron showers is higher than for proton showers. Moreover, the zenith angle effect is different for different composition assumption. In the case of pure proton assumption (Figure 6.2a), the flux in the more vertical zenith band ($0.8 \le \cos(\theta) < 0.9$) is higher than the flux in the more inclined zenith band ($0.9 \le \cos(\theta) \le 1.0$), while the behavior is reversed in the case of pure iron assumption (Figure 6.2b). This dependence on the zenith angle can be used for composition analysis.

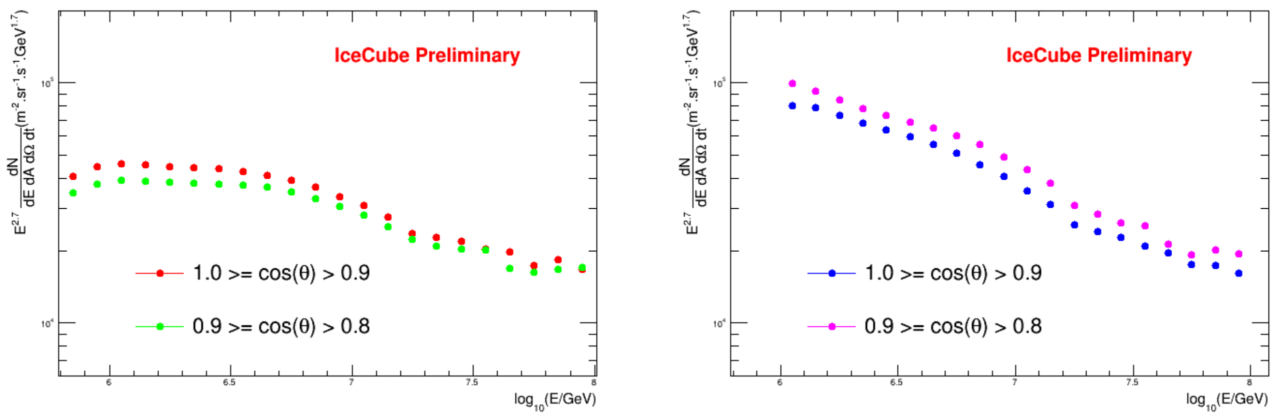

(a) Proton (b) Iron

Figure 6.2: The cosmic ray energy spectrum multiplied with $E^{2.7}$ in the two studied zenith bands. The energy spectrum with proton assumption for the primary mass is shown on the left and with iron assumption on the right.

6.2 Systematic Uncertainties:

There are several systematic uncertainties in this analysis that could affect the measurement of the cosmic ray energy spectrum with IceTop. These systematics are related to Monte Carlo simulations (interaction model used in CORSIKA, atmosphere ...), the detection principle (VEM calibration, Figure 2.10), environmental effects on detector (snow correction Section 4.2), or the method used in the measurement (composition assumption). These systematic uncertainties are discussed below and only the systematics due to snow correction and VEM calibration will be included in the measurement of the energy spectrum for this analysis.

6.2.1 Snow Correction Uncertainty:

Snow has a large effect on the detected signal with IceTop. The signal is attenuated with the amount of snow accumulated on top of IceTop tanks (as explained in Section 2.4.2). The determination of the effective attenuation length λ_{eff} in the snow correction procedure produces a systematic uncertainty on the energy spectrum. This correction does not account for the dependence on the zenith angle of the shower, and for the dependence on the distance from the shower core where the EM and the muonic contribution of the shower are different. This dependence is still under study [100] and will be taken into account in IceTop future analysis.

The attenuation length obtained for the entire year of data is $\lambda = 2.2$ m and we will use a variation of ± 0.2 m on the attenuation length as the systematic uncertainty due to snow. Figure 6.3 shows the effect of the snow attenuation length uncertainty on the energy spectrum.

The effect of snow is minimal at low energy because most of these low energy events are in the new part of the detector and selected with the small shower selection (See section 5.1.1). A main concern in the future is to improve the snow correction procedure [100] and have a better understanding for the effect of snow at low energy.

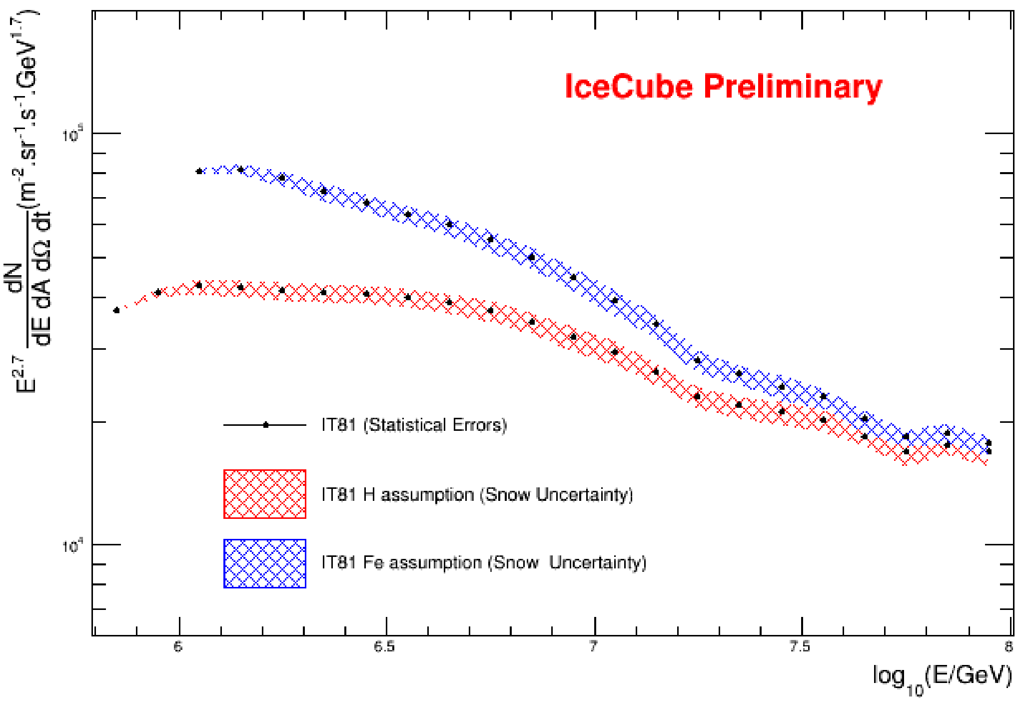

Figure 6.3: The cosmic ray energy spectrum multiplied with $E^{2.7}$ with 0.2 m uncertainty in the snow attenuation length (shown in the band).

6.2.2 VEM Calibration Uncertainty:

The signal measured with IceTop tanks is calibrated with the signal from near vertical muons (see section 2.2.4). The uncertainty in the charge calibration gives an uncertainty in the energy scale. This was studied using Monte Carlo simulations [102] and was found that the VEM spectrum can be generated with an uncertainty of $2-3\%$. This error is translated as a shift in the S_{exp} parameter and therefore produces an uncertainty in the energy spectrum. Figure 6.4 shows the uncertainty in the energy spectrum using $\pm 3\%$ uncertainty in the charge calibration.

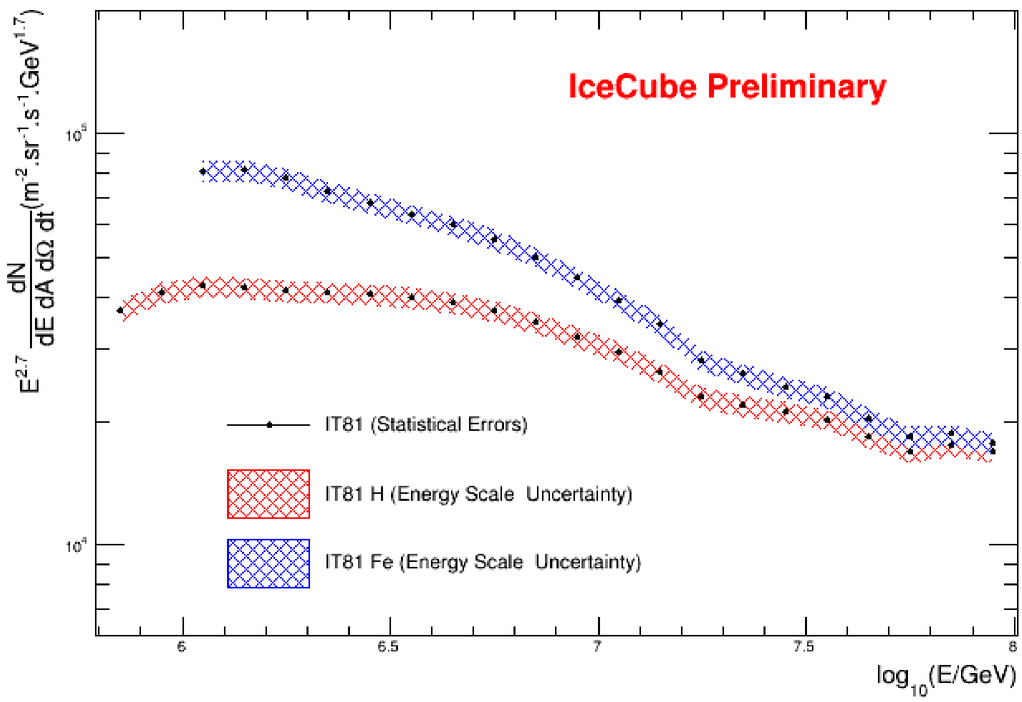

Figure 6.4: The cosmic ray energy spectrum multiplied with $E^{2.7}$ with $\pm 3\%$ uncertainty in the charge calibration (shown in the band).

6.2.3 Interaction Model Uncertainty:

The hadronic interaction model used to produce in the Monte Carlo simulations for this analysis is SYBILL 2.1 [78] (see section 3.1). To determine the uncertainty in the interaction model, one has to produce a sample of air showers with a different interaction model (QGSJET) and see the effect on the energy estimator S_{exp} and consequently on the energy spectrum. This uncertainty was found to be small in previous IceTop measurements (2.3% at 3 PeV [46]) and will be taken into account in a later analysis.

6.2.4 Mass Composition Uncertainty:

Since the composition of the primary cosmic ray particle is unknown and not measured in this analysis, a composition model has to be assumed. Proton and iron are the only available simulated primaries. Therefore, the primary cosmic ray particle in this work is considered to be pure proton or pure iron, the most extreme cases for the composition. It can also be seen from Figure 6.4 that the energy spectrum is different for different composition assumption although this composition dependence becomes very small at high energy.

In order to have a more accurate composition assumption, More primary masses must be simulated and included in the composition assumption. Since CORSIKA can not simulate masses heavier than iron, only primary masses lighter then iron will be simulated (Helium and Oxygen). A composition assumption of four elements (Proton, Helium, Oxygen and Iron) will provide a better description of the primary cosmic ray particle.

6.3 Energy Spectrum Results

Figure 6.5 shows the measured cosmic ray energy spectrum with IceTop for the one year of data taking period mentioned earlier. Since the composition of the primary cosmic ray particle is unknown and is not measured directly in this analysis, the energy spectrum is derived for two extreme mass assumptions, pure proton and pure iron. Due to their early interaction in the atmosphere, the energy threshold for iron showers is higher than for proton showers (as explained in Section 5.2). Therefore, the energy spectrum is shown starting from 500 TeV for proton assumption and 1 PeV for iron assumption. The systematic uncertainties from snow and charge calibration are added in quadrature and the numerical values are given in Appendix E. The results shows that the energy spectrum is not a smooth power law for both proton and iron assumptions. The spectra differ up to a factor of 2 at low energies but the dependence on composition becomes rather small at high energy. A comparison of the results to previous IceTop energy spectrum measurements and energy spectra from different cosmic ray experiments is given in Chapter 7.

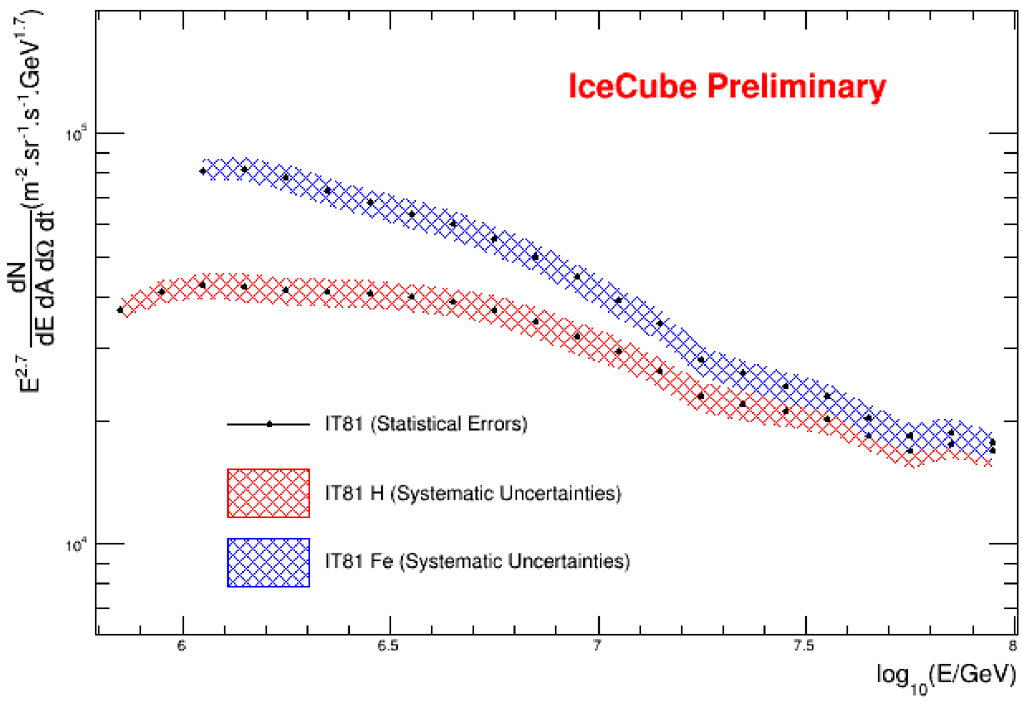

Figure 6.5: The cosmic ray energy spectrum multiplied with $E^{2.7}$. The systematic uncertainties are obtained by adding the uncertainties of snow and charge calibration in quadrature.

The cosmic ray energy spectra obtained in this thesis show a remarkable deviation from a single power law. In order to study the features of the energy spectrum, three power laws were fitted to the spectrum with pure proton assumption in the vertical zenith band ($0.9 \leq \cos(\theta) \leq 1.0$), and in three different energy ranges (Figure 6.6). The first power law is fitted in the energy range 5.9< $\log_{10}$E<6.7 and has a spectral index of γ_1 = -1.57 $\pm$ 0.077. The second power law is fitted in the energy range 6.7< $\log_{10}$E<7.3 and has a spectral index of γ_2 = -2.37 $\pm$ 0.014. The third power law is fitted in the energy range 7.3< $\log_{10}$E<8 and has a spectral index γ = -1.81 $\pm$ 0.017. A first break in the energy spectrum is observed at 6.71 in $\log_{10}$E which corresponds to an energy of 5.1 PeV, found from the intersection point of the first two power laws. A second break is found at 7.32 in $\log_{10}$E which corresponds to an energy of 21 PeV.

The elemental composition of cosmic rays is believed to be dominated by the light components at low energy. Therefore, the energy spectrum with iron assumption was not fitted.

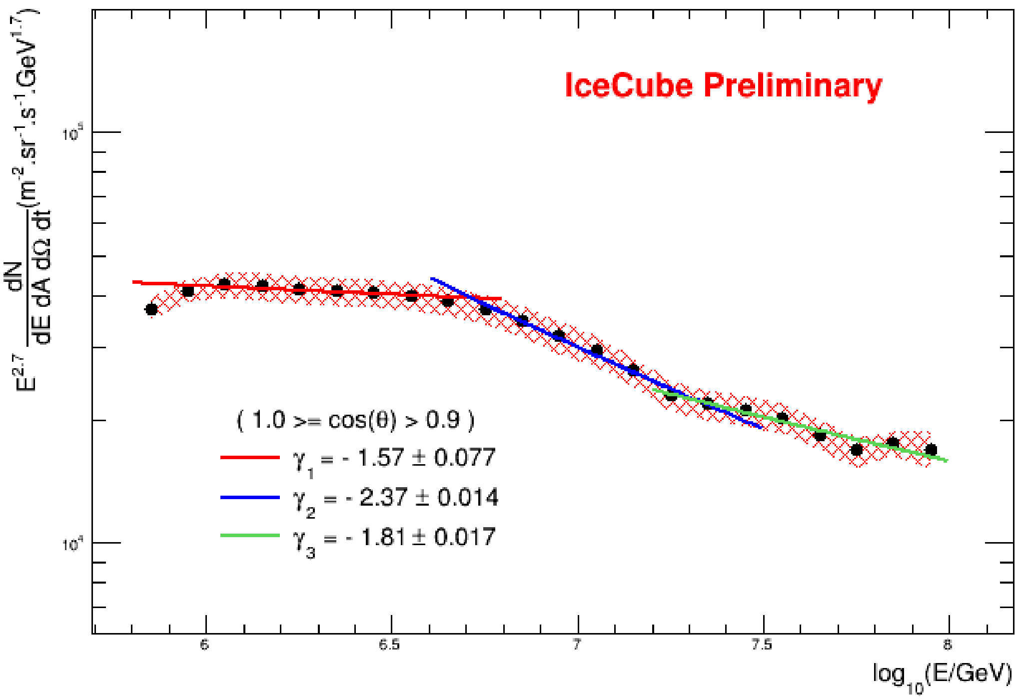

Figure 6.6: The cosmic ray energy spectrum with proton assumption. The spectrum is fitted with three power laws in different energy ranges.

Chapter 7

Discussion and Outlook

7.1 Comparison with Previous IceTop Measurements

The cosmic ray energy spectrum has been measured, with IceTop alone and in combination with IceCube, when the detector was in its 26, 40 and 73 configurations [97, 103, 104, 46, 99]. The IT26 [97] energy spectrum measurement was done with IceTop data only (between June 1, 2007 and October 31, 2007) and used a one dimensional unfolding procedure to estimate the primary energy. The IT-C40 [104] analysis used coincident events that trigger both the IceTop and the IceCube detectors (August 2008). This analysis used a neural network method to measure the energy spectrum and the composition of cosmic rays at the same time. 3 years of data (between June 1, 2010 and May 2, 2013) were analyzed with two independent methods. In the first [105], only IceTop data were used and a composition model (H4a [106]) was assumed in order to measure the all-particle energy spectrum of cosmic rays. The H4a model consists of five elemental groups: H, He, CNO, MgSi and Fe. Each group has three components (Galactic cosmic rays from supernova remnants, Galactic cosmic rays from unknown origin and an extra Galactic component). In the second [105], the coincident data from both IceTop and IceCube were analyzed to measure the energy spectrum and composition of cosmic rays using an neural network approach.

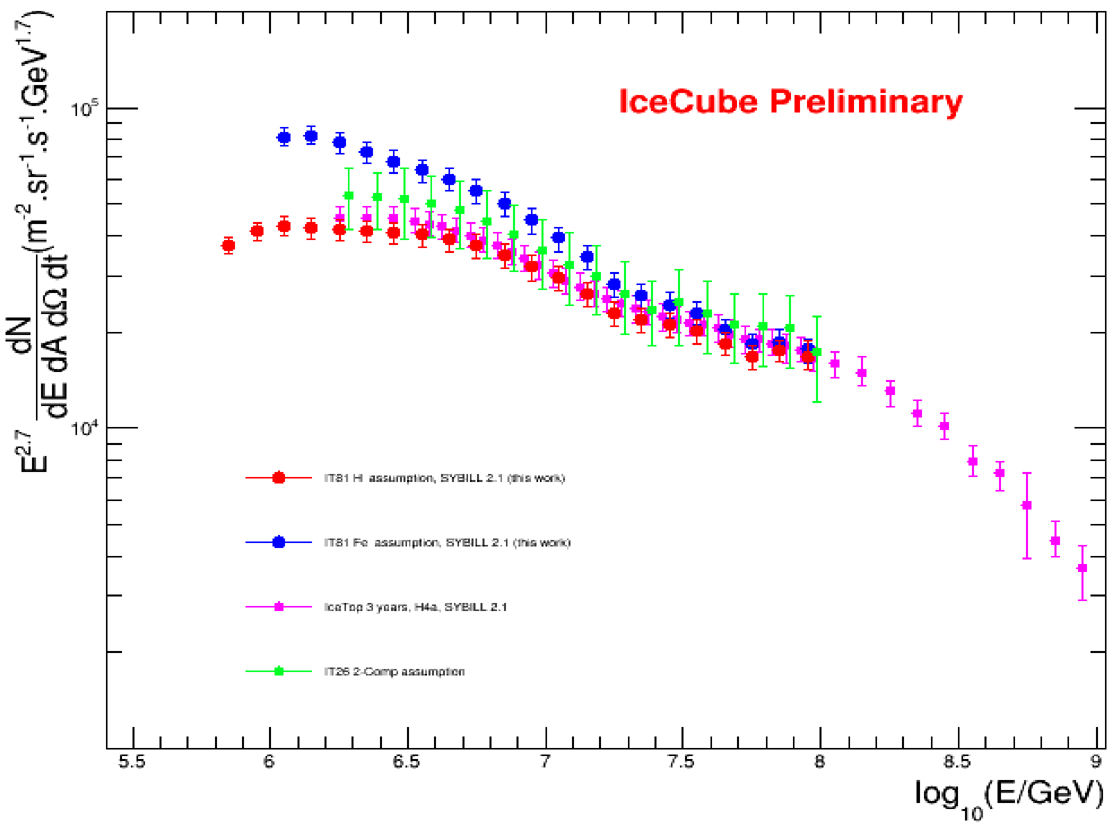

Figure 7.1: The cosmic ray energy spectrum in this analysis compared to previous energy spectrum measurements with IceTop only [97, 105]. Error bars represent the systematic uncertainties for each measurement.

Figure 7.1 shows a comparison of the cosmic ray energy spectra measured in this and previous analyses using the IceTop detector only. A composition model was assumed in previous measurements. The two component model was assumed for the IT26 energy spectrum measurement [97] and the H4a model was assumed for the IT73 energy spectrum [105]. For high energies (beyond 7.5 in $\log_{10}$(E/GeV)), the measured energy spectra with proton and iron assumption are in a good agreement with other IceTop spectra. The effect of the composition assumption becomes stronger at lower energies. However, in the case of a pure proton assumption, the results are consistent with previous measurements within systematics uncertainties, mainly with the IT73 energy spectrum measurement which uses the same technique for the energy reconstruction.

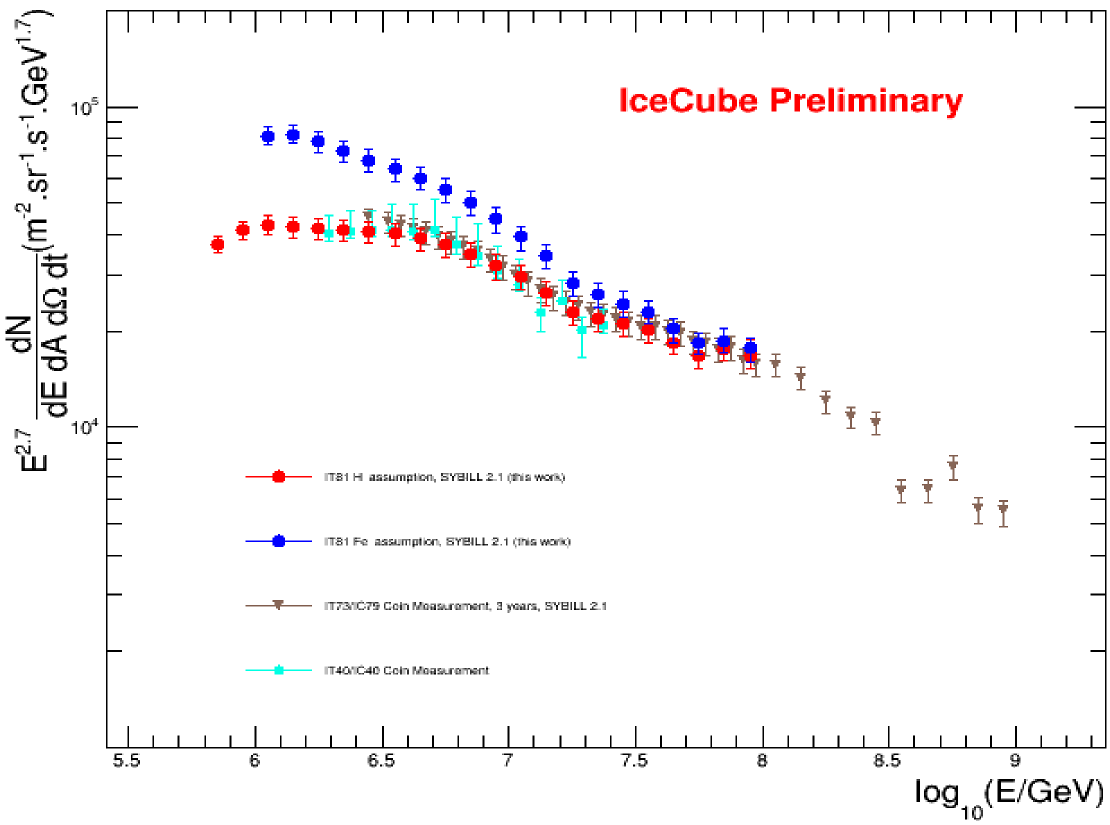

Figure 7.2: The cosmic ray energy spectrum in this analysis compared to previous energy spectrum measurements with IceTop-IceCube coincidence analysis [104, 105]. Error bars represent the systematic uncertainties for each measurement.

In Figure 7.2, the measured energy spectra are compared to measurements of the energy spectrum using coincident events in IceTop and IceCube. The main difference between my analysis and the coincidence analysis is that we assume the primary cosmic ray is pure proton or pure iron, while the mass composition and the all-particle energy spectrum were determined at the same time in the coincidence analysis [104, 105]. The comparison shows that the measured energy spectrum with iron assumption is not comparable at low energy while the spectrum with proton assumption agrees within systematic uncertainties over the entire energy range.

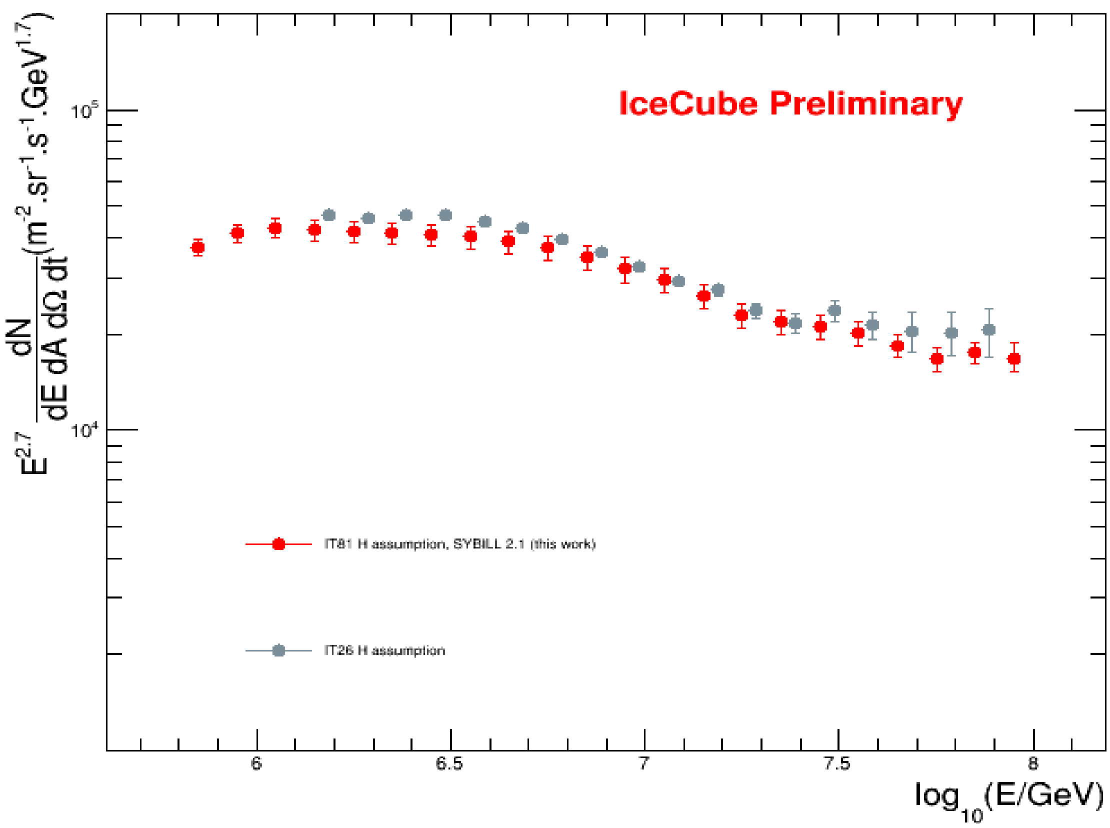

Figure 7.3: The measured cosmic ray energy spectrum with proton assumption compared to the energy spectrum measured with IT26 with proton assumption [97]. Error bars represent the statistical uncertainties for the IT26 energy spectrum and systematic uncertainties for the energy spectrum of this analysis.

The measured energy spectrum with proton assumption can also be compared to the IT26 [97] spectrum with proton assumption (Figure 7.3). The difference between the two spectra can be due to the smaller zenith angle used in the IT26 energy spectrum ($0° - 30°$) which is very sensitive to the assumed composition, as seen in Section 6.1. Another reason could be due to the improvements in the reconstruction and the simulation used in my analysis.

7.2 Comparison with Measurements from Other Experiments

Figure 7.4 shows a comparison of the measured energy spectra in this work under the proton and iron composition assumption with spectra from other cosmic ray experiments. For low energies, the energy spectrum with proton assumption is comparable to the spectrum measured by the Tibet experiment [107] where the dependence on the interaction model and primary mass are minimal, because of the high altitude of the Tibet experiment (4300 m above sea level) where the air showers are dominated by the electromagnetic component and close to their shower maximum at these energies. For higher energies, both spectra (with proton and iron assumption), converge and are slightly higher than the spectrum measured by Tibet which becomes also lower than other measurements. However, the spectrum is in good agreement with the GAMMA [108] and KASCADE-Grande [109] measurements.

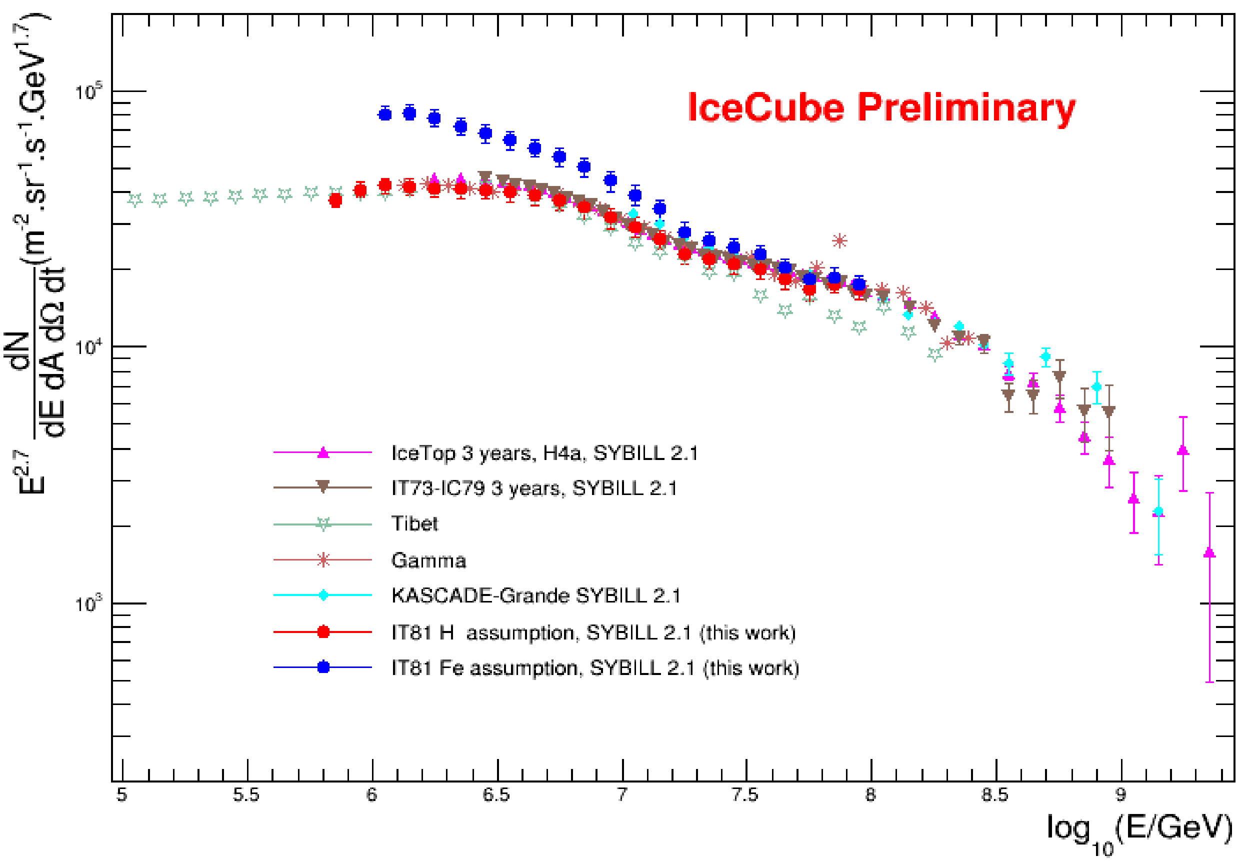

Figure 7.4: The cosmic ray energy spectrum from this analysis compared to other energy spectrum measurements: IceTop 73 [105], IT73-IC79 coincidence analysis [105], Tibet [107], GAMMA [108], KASCADE-Grande [109]. Error bars represent the systematic uncertainties in this measurements, only statistical uncertainties are shown for other measurements.

7.3 Outlook

The main goal of my analysis was to measure the cosmic ray energy spectrum with the completed IceTop detector and investigate the possibility to extend the energy spectrum measurement towards lower energies using the Infill array in the center of the detector. This has been done using one year of data and in a wide energy range from 500 TeV and 1 PeV for proton and iron assumption of primary mass, respectively, up to 100 PeV. The extension of the energy threshold to 500 TeV is very important because at these energies the energy spectrum becomes very close to energy spectra measured with direct cosmic ray experiments.

The energy spectra measured in this analysis show a good agreement with energy spectra from previous IceTop analyses. While the composition of primary cosmic ray is assumed to be pure proton or pure iron, the composition together with the energy spectrum have been measured previously using coincident events between IceTop and IceCube. The comparison of the energy spectra measured using two different methods is very important for a better understanding of the detector. The energy spectrum measurement with proton assumption showed a clear deviation from a single power law.

Energy spectra with proton and iron assumption were studied in two zenith bands ($\Omega_1 = [0° - 26.8°]$ and $\Omega_2 = [26.8° - 36.9°]$). The results led to a disagreement between spectra from different zenith bands. This disagreement is due to the zenith dependence of the primary mass assumed to derive the energy spectrum.

Several steps can be done in order to improve the measurement. Firstly: Snow which will continue to accumulate above the detector tanks in the following years . With an extra layer on top of the IceTop tanks, low energy showers will be attenuated and they will not trigger the tanks anymore. In addition, snow is on of the main sources of systematics in current IceTop analysis. Therefore a better treatment of the snow effect is needed in data and simulation. Secondly: Since the composition is not measured directly in this analysis, simulating more elements will enable us to assume a certain composition model and thereby understand the zenith dependence on primary mass and to extract the all particle energy spectrum.

Appendix A

CORSIKA Steering File

The run number depends on the job number and was chosen to be unique. PRIM is the primary particle produced (H or Fe). ERANG indicates the required energy range (100 TeV to 100 PeV). The SEED depends on both the run and the job numbers. MAGNET is the magnetic field at the South Pole according to the International Geomagnetic Reference Field (IGRF) [110] and it was set to an average value between June and October 2007.

```
RUNNR   {RUNNR}                       Number of run
EVTNR   1                             Number of first shower event
NSHOW   1                             Number of showers to generate
PRMPAR  {PRIM}                        Type of primary particle
ESLOPE  -1.0                          Slope of primary energy spectrum
ERANGE  {Depends on the dataset
         and JOB_NR}
                                      Energy range of primary particle (GeV)
THETAP  0. 65.                        Range of zenith angle (degree)
PHIP    0. 360.                       Range of azimuth angle (degree)
```

```
SEED    {}     0   0          Seed for 1. random number sequence (Hadron sh
SEED    {}     0   0          Seed for 2. random number sequence (EGS4)
OBSLEV  2834.e2               Observation level at South Pole (cm)
ELMFLG  T   T                 EM flags (NKG, EGS)
RADNKG  2.E5                  Outer radius for NKG lateral density.
ARRANG  -119.                 Rotation from CORSIKA to I3 coordinates
FIXHEI  0.  0                 First interaction height
FIXCHI  0.                    Starting altitude (g/cm**2)
MAGNET  16.59 -52.79          Magnetic field at South Pole. (uT)
HADFLG  0  1  0  1  0  2      Flags hadronic interact and fragmentation
SIBYLL  T  0                  Model for high energy hadronic interaction
SIBSIG  T                     Cross sections
ECUTS   .05 .05 .01 .002      Energy cuts for particles (hadrons/mu/e/gamma
MUADDI  T                     Additional info for muons
MUMULT  T                     Muon multiple scattering angle
LONGI   T  20.  T  F          Longitudinal distribution & step size & fit
MAXPRT  1                     Maximum number of printed events
ECTMAP  1.e4                  Cut on gamma factor for printout
STEPFC  1.0                   Mult scattering step length fact.
DEBUG   F  6  F  1000000      Debug flags
DIRECT  .                     Output directory
ATMOD   12                    Atmospheric model (July is used)
EXIT                          Terminates input
```

Appendix B

Energy Calibration

The energy calibration was done using the relationship between the shower size (S_{exp}) and the true primary energy from simulations (Figure 5.9 for proton and Figure 5.10 for iron). For a given zenith band, we plot the logarithm of the true energy distributions in 0.1 intervals of $\log_{10}(S_{exp})$. A Gaussian is fitted for each true energy distribution and the mean of the Gaussian is assigned as the estimated energy for the respective $\log_{10} S_{exp}$ interval. The relationship between $\log_{10}(S_{exp})$ and $\log_{10}(E_{true})$ will be fitted with Equation 5.3 for proton and iron induced showers in two zenith bands.

B.1 Proton:

B.1.1 First Zenith Band ($0.9 < \cos(\theta) \leq 1.0$):

Small Showers:

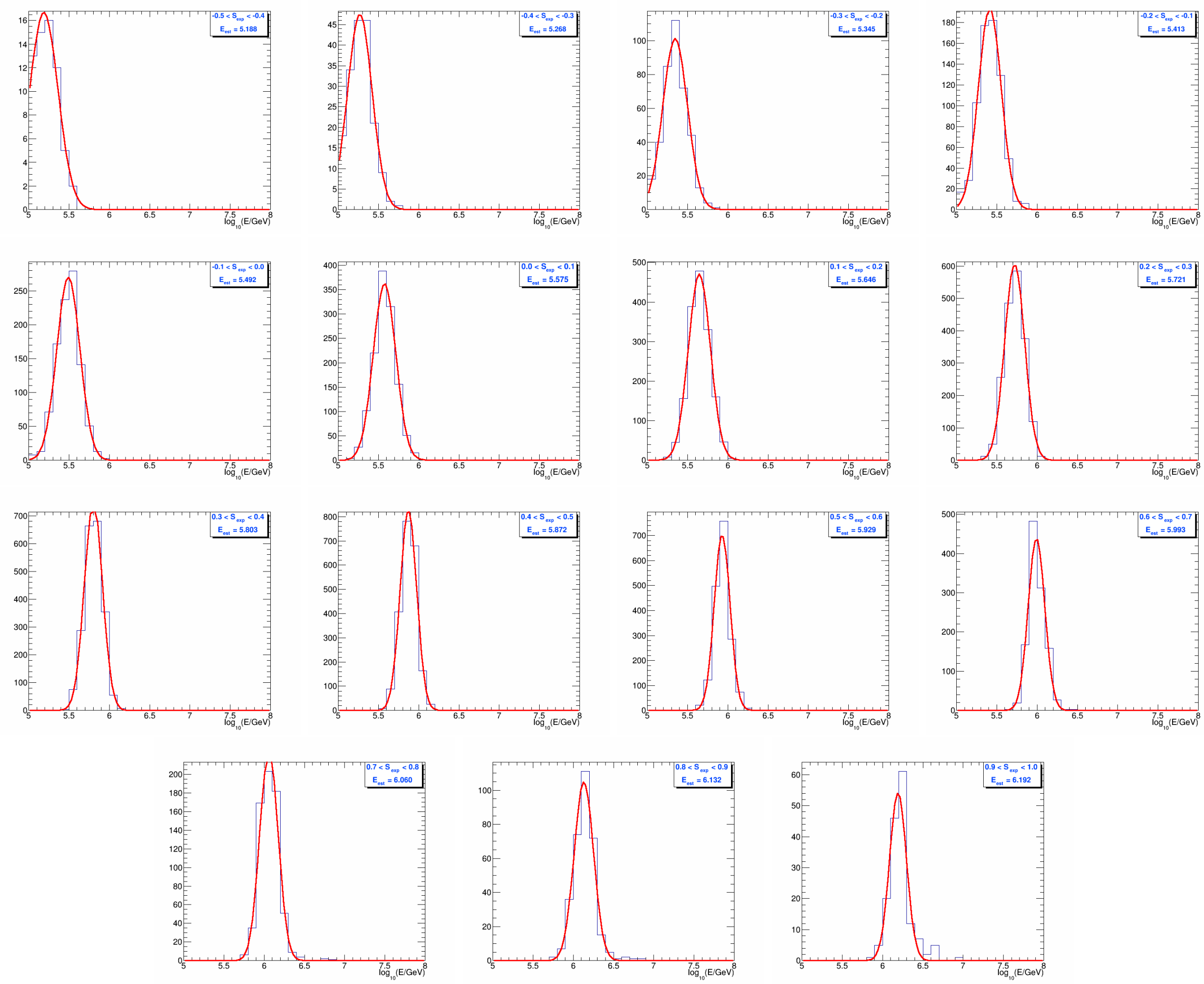

Figure B.1: True energy distributions in $\log_{10}(S_{exp})$ intervals fitted with a Gaussian for proton induced showers and in a zenith band $0.9 < \cos(\theta) \leq 1.0$. Plots are obtained with the small showers selection.

Standard Showers:

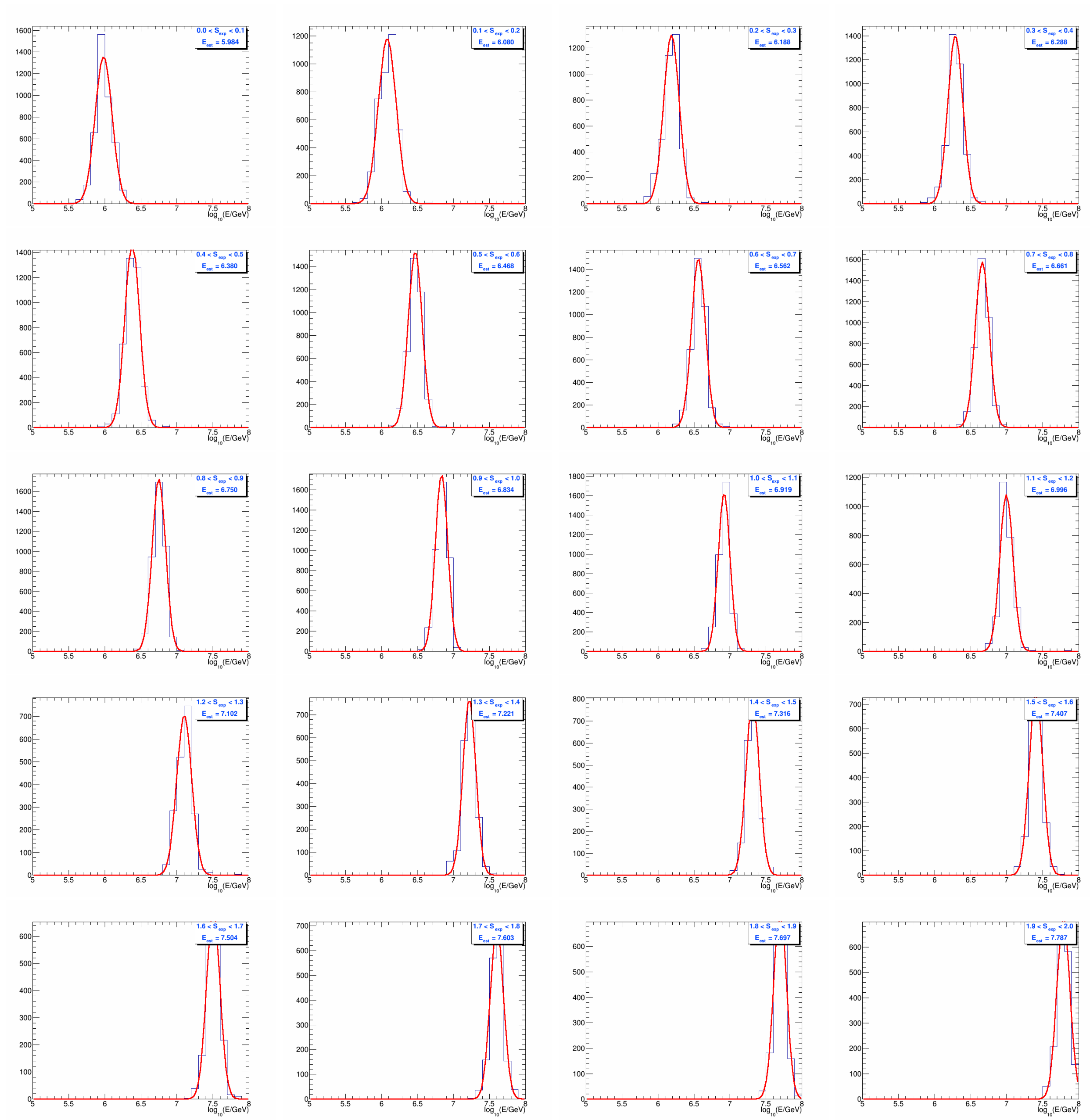

Figure B.2: True energy distributions in $\log_{10}(S_{exp})$ intervals fitted with a Gaussian for proton induced showers and in a zenith band $0.9 < \cos(\theta) \leq 1.0$. Plots are obtained with the standard showers selection.

B.1.2 Second Zenith Band ($0.8 < \cos(\theta) \leq 0.9$):

Small Showers:

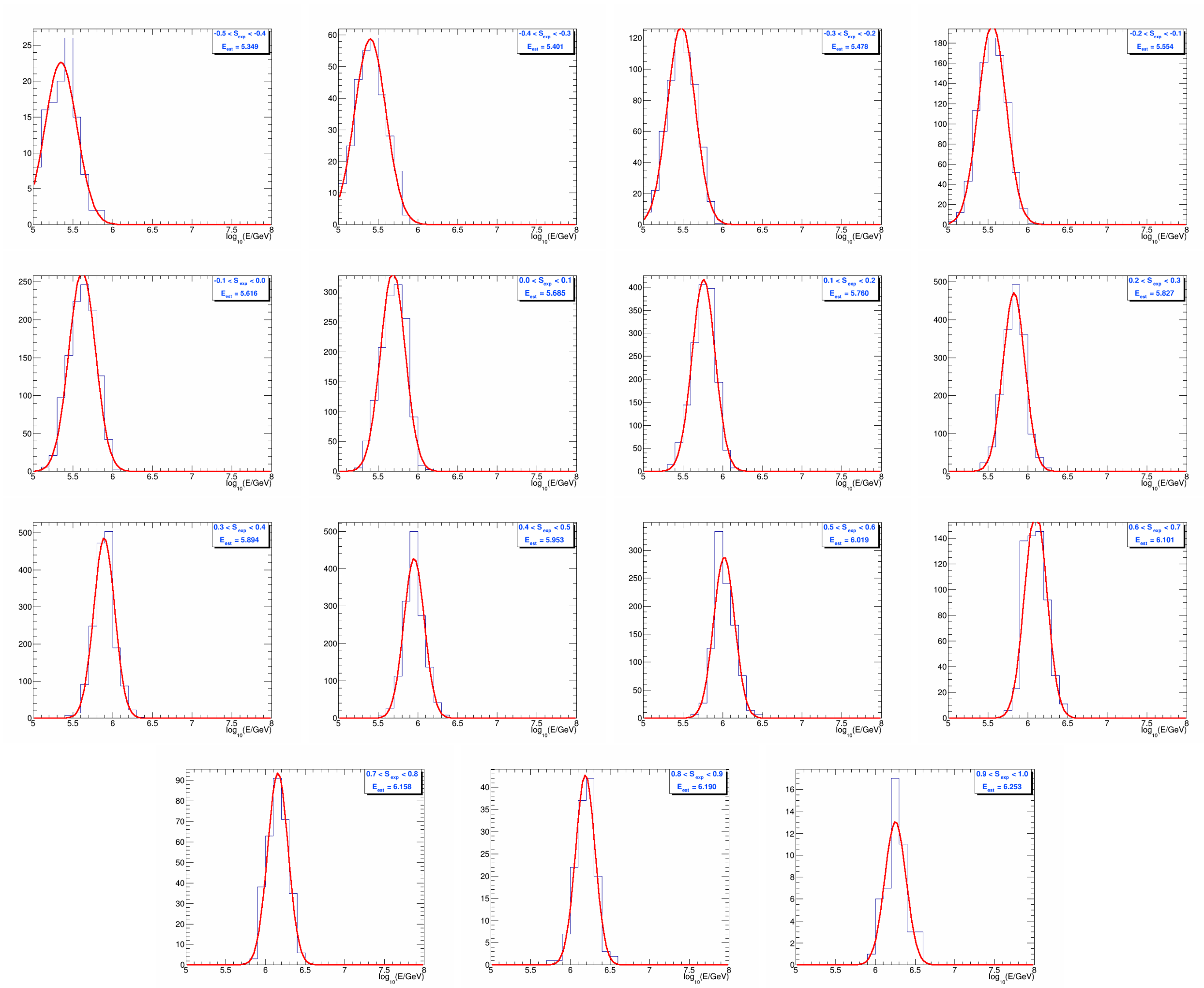

Figure B.3: True energy distributions in $\log_{10}(S_{exp})$ intervals fitted with a Gaussian for proton induced showers and in a zenith band $0.8 < \cos(\theta) \leq 0.9$. Plots are obtained with the small showers selection.

Standard Showers:

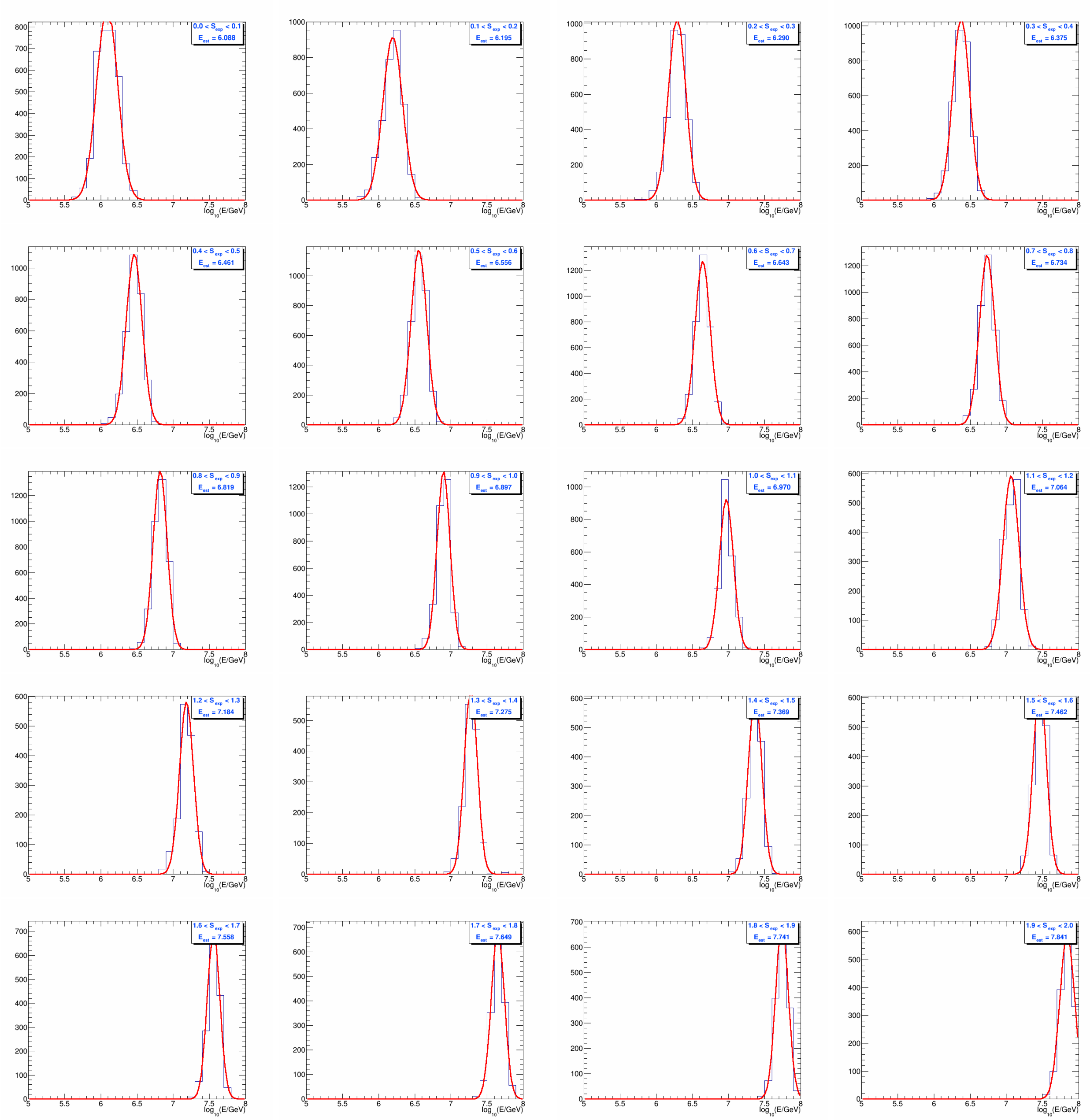

Figure B.4: True energy distributions in $\log_{10}(S_{exp})$ intervals fitted with a Gaussian for proton induced showers and in a zenith band $0.8 < \cos(\theta) \leq 0.9$. Plots are obtained with the standard showers selection.

B.2 Iron:

B.2.1 First Zenith Band ($0.9 < \cos(\theta) \leq 1.0$):

Small Showers:

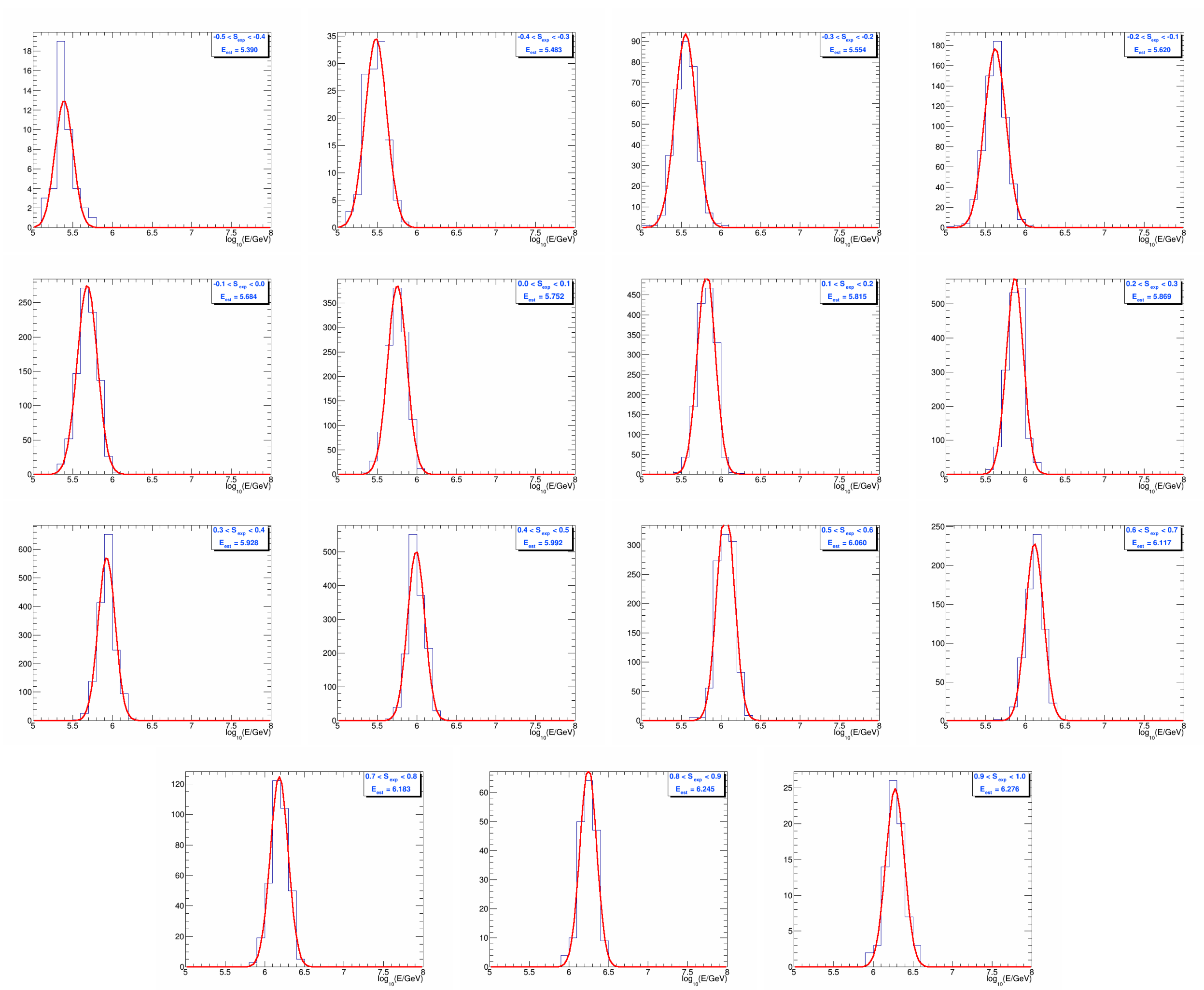

Figure B.5: True energy distributions in $\log_{10}(S_{exp})$ intervals fitted with a Gaussian for iron induced showers and in a zenith band $0.9 < \cos(\theta) \leq 1.0$. Plots are obtained with the small showers selection.

Standard Showers:

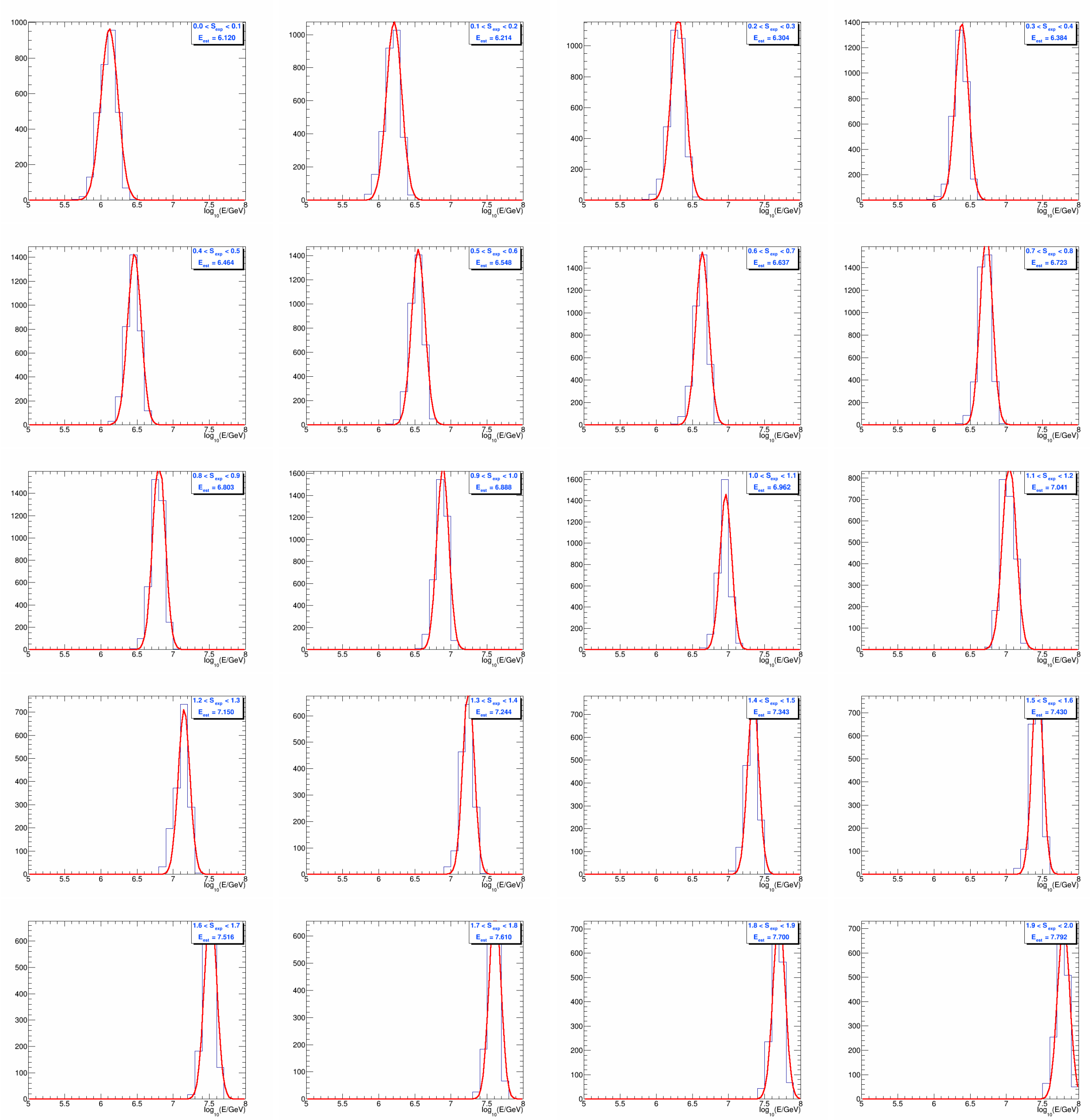

Figure B.6: True energy distributions in $\log_{10}(S_{exp})$ intervals fitted with a Gaussian for iron induced showers and in a zenith band $0.9 < \cos(\theta) \leq 1.0$. Plots are obtained with the standard showers selection.

B.2.2 Second Zenith Band ($0.8 < \cos(\theta) \leq 0.9$):

Small Showers:

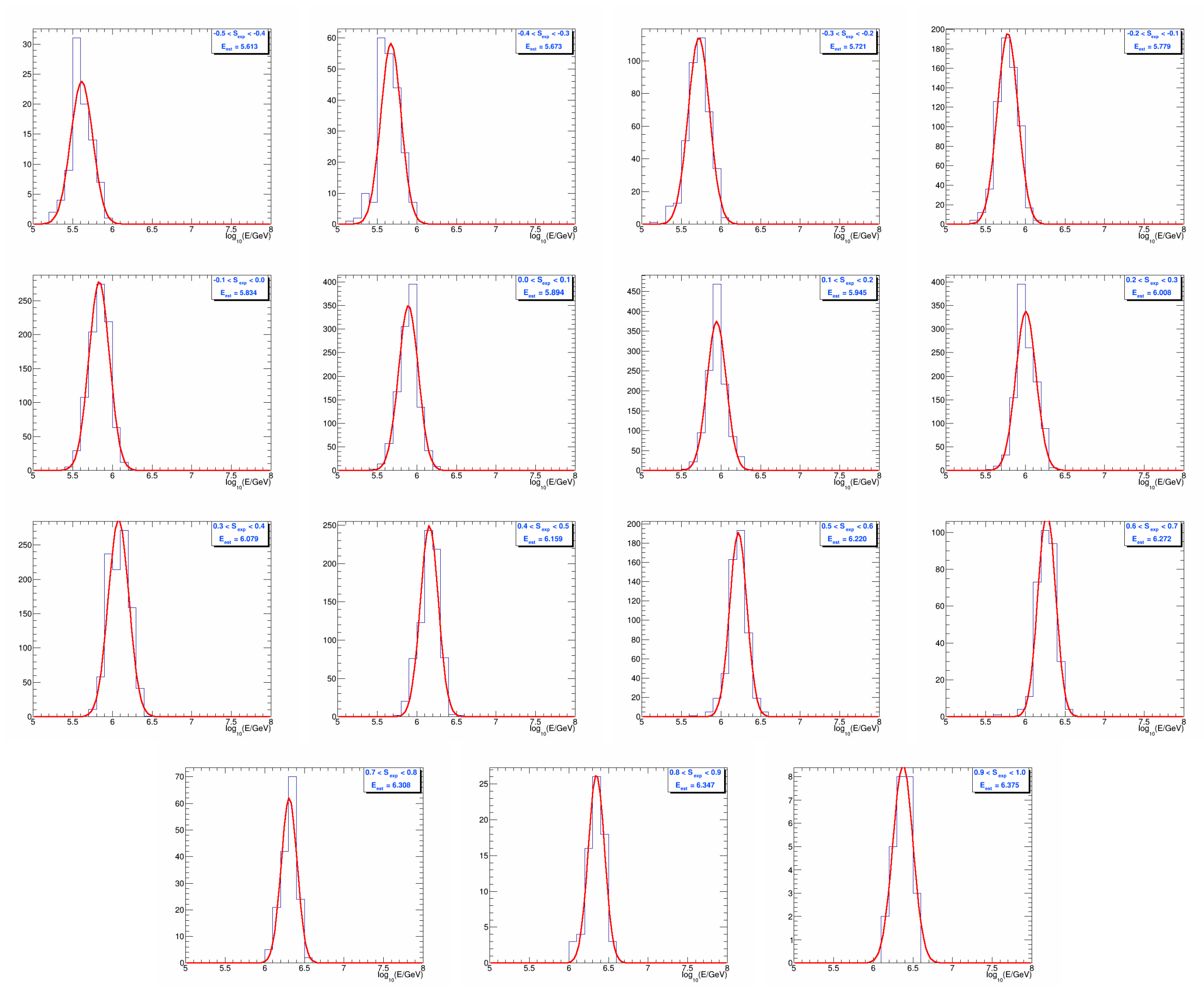

Figure B.7: True energy distributions in $\log_{10}(S_{exp})$ intervals fitted with a Gaussian for iron induced showers and in a zenith band $0.8 < \cos(\theta) \leq 0.9$. Plots are obtained with the small showers selection.

Standard Showers:

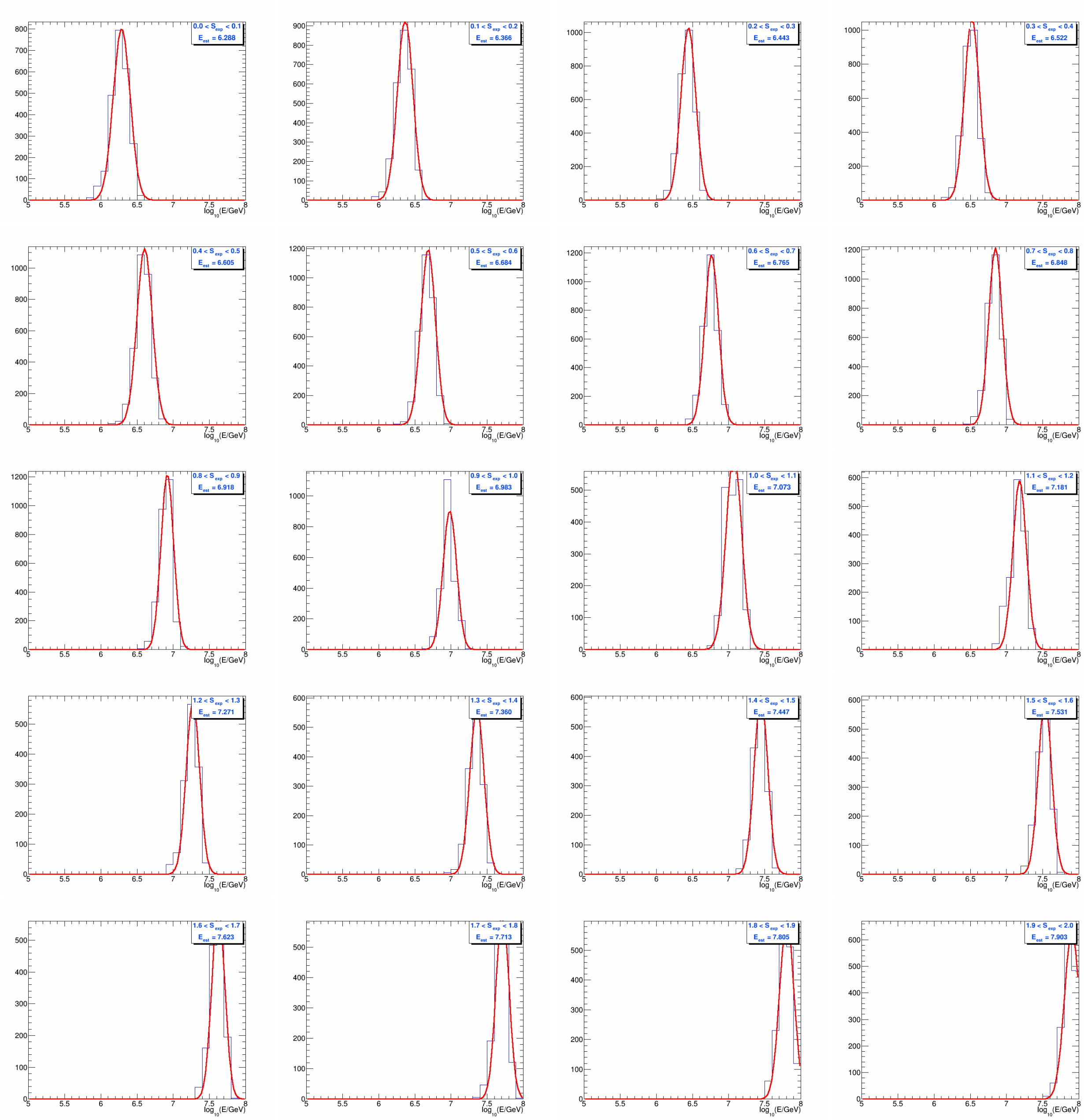

Figure B.8: True energy distributions in $\log_{10}(S_{exp})$ intervals fitted with a Gaussian for iron induced showers and in a zenith band $0.8 < \cos(\theta) \leq 0.9$. Plots are obtained with the standard showers selection.

Appendix C

Energy Bias and Resolution

The energy bias and resolution are obtained from Equation 5.4. The mean of these distributions is used as the energy bias and the RMS as the energy resolution for proton and iron induced showers.

C.1 Proton:

C.1.1 First Zenith Band ($0.9 < \cos(\theta) \leq 1.0$):

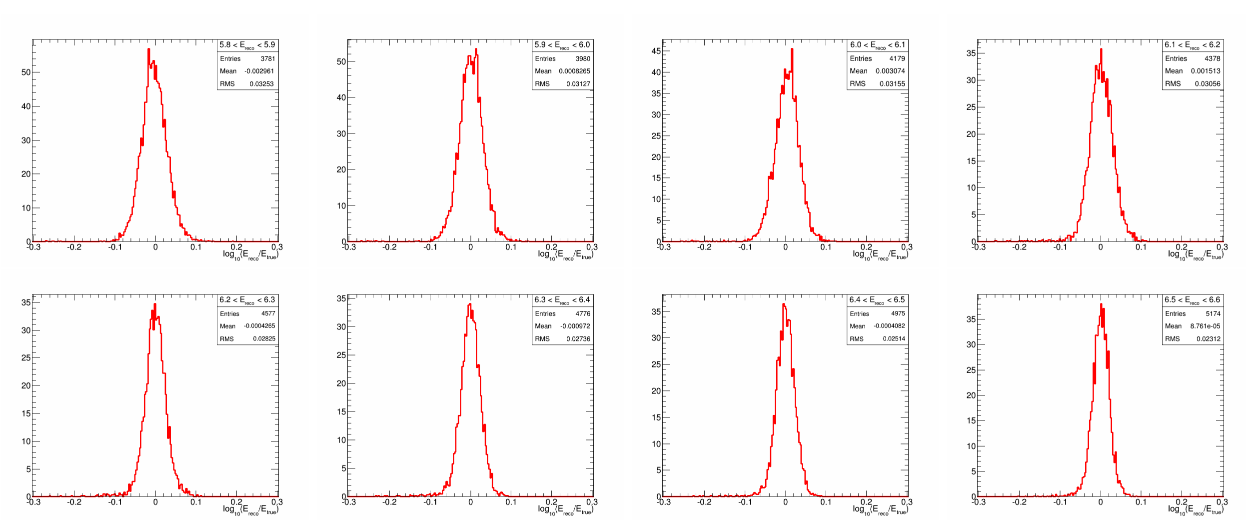

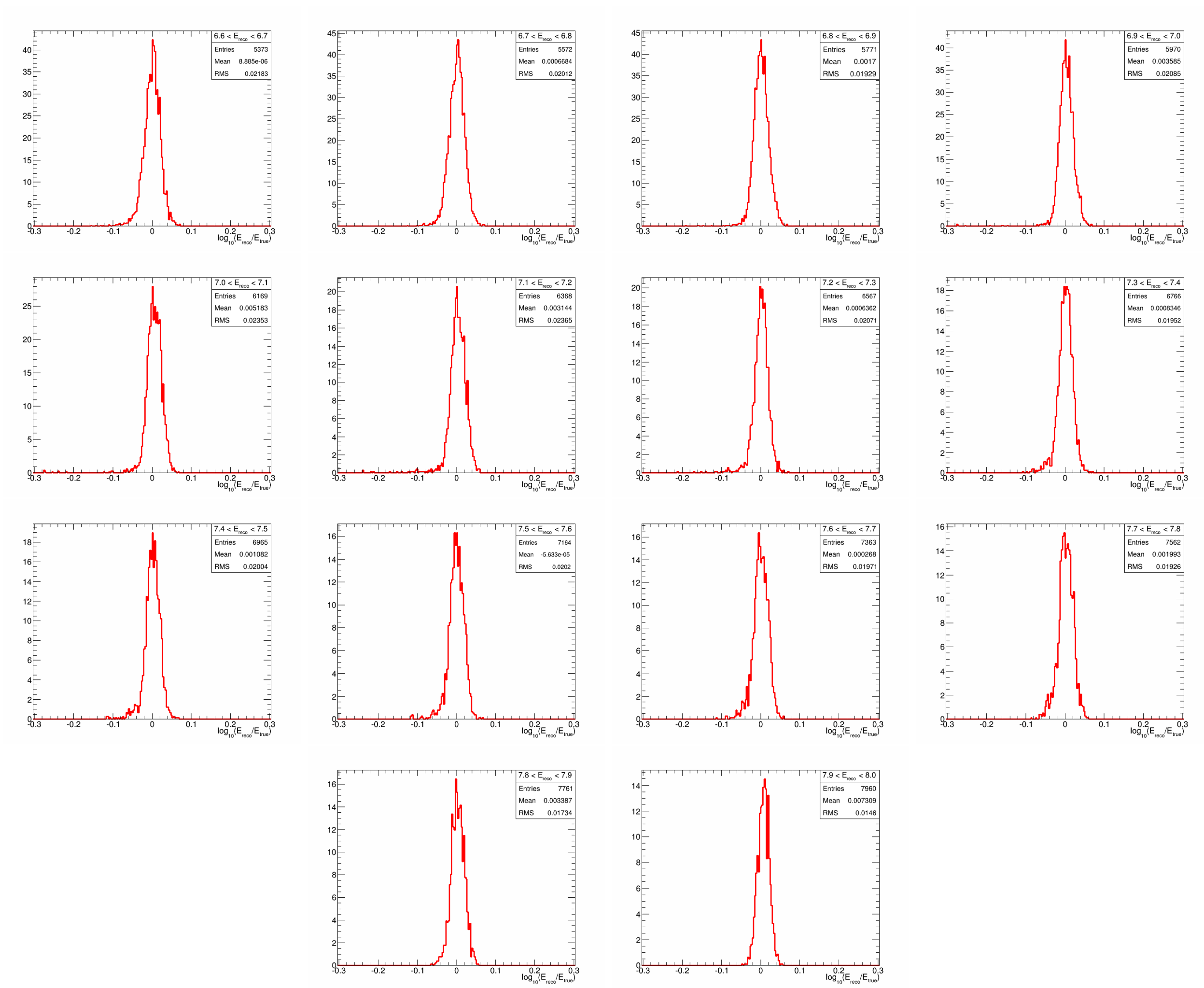

Figure C.1: Fractional distributions of true and reconstructed energy for proton induced showers with a zenith angle $0.9 < \cos(\theta) \leq 1.0$. The energy bias and resolution are considered as the mean and RMS of these distributions, respectively.

C.1.2 Second Zenith Band ($0.8 < \cos(\theta) \leq 0.9$):

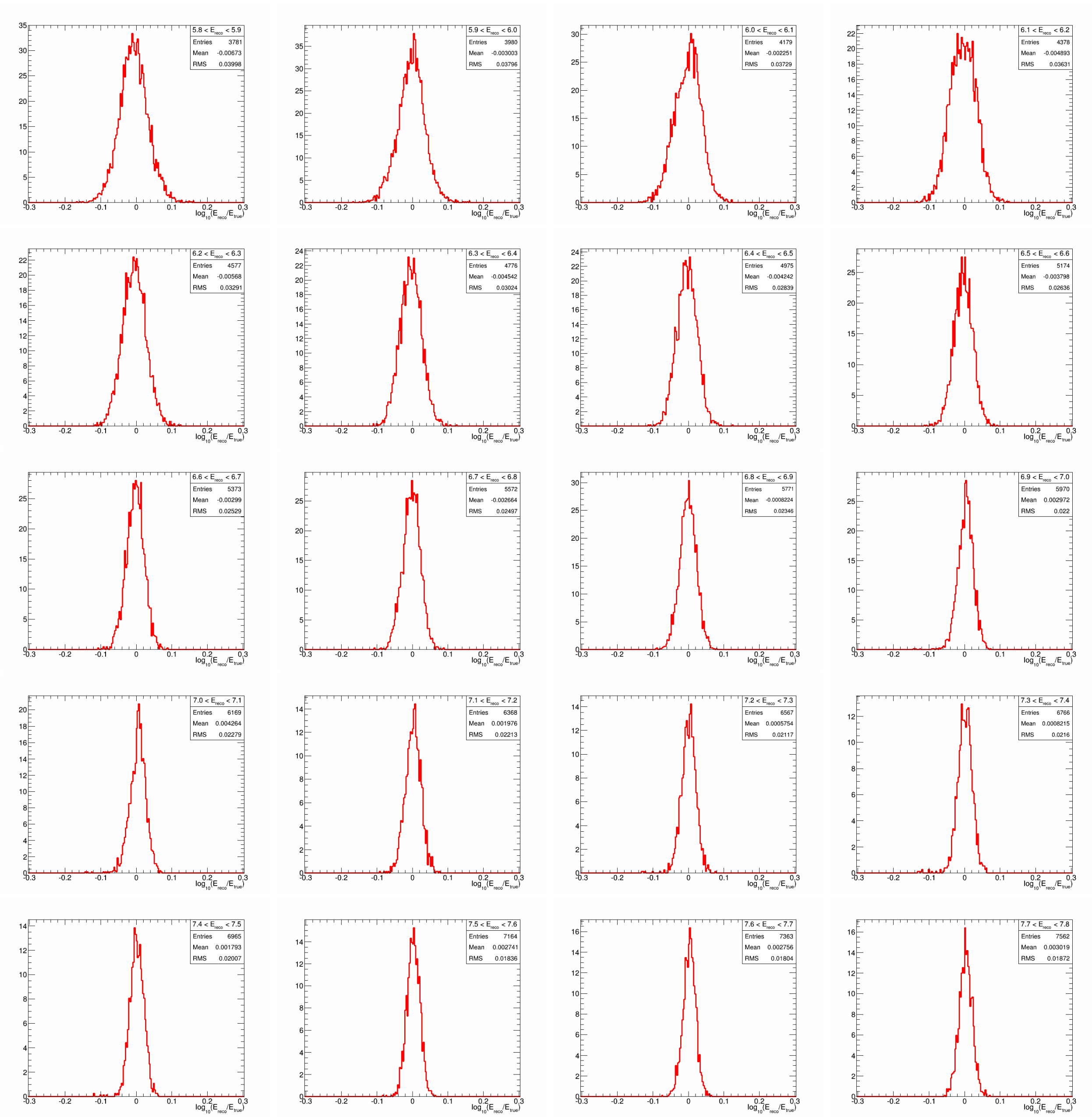

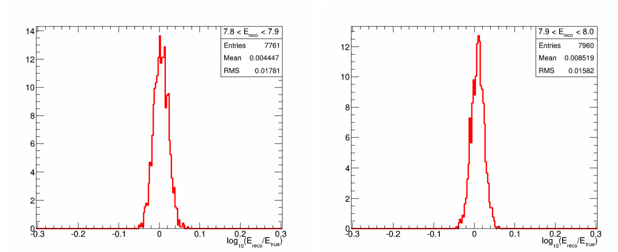

Figure C.2: Fractional distributions of true and reconstructed energy for proton induced showers with a zenith angle $0.8 < \cos(\theta) \leq 0.9$. The energy bias and resolution are considered as the mean and RMS of these distributions, respectively.

C.2 Iron:

C.2.1 First Zenith Band ($0.9 < \cos(\theta) \leq 1.0$):

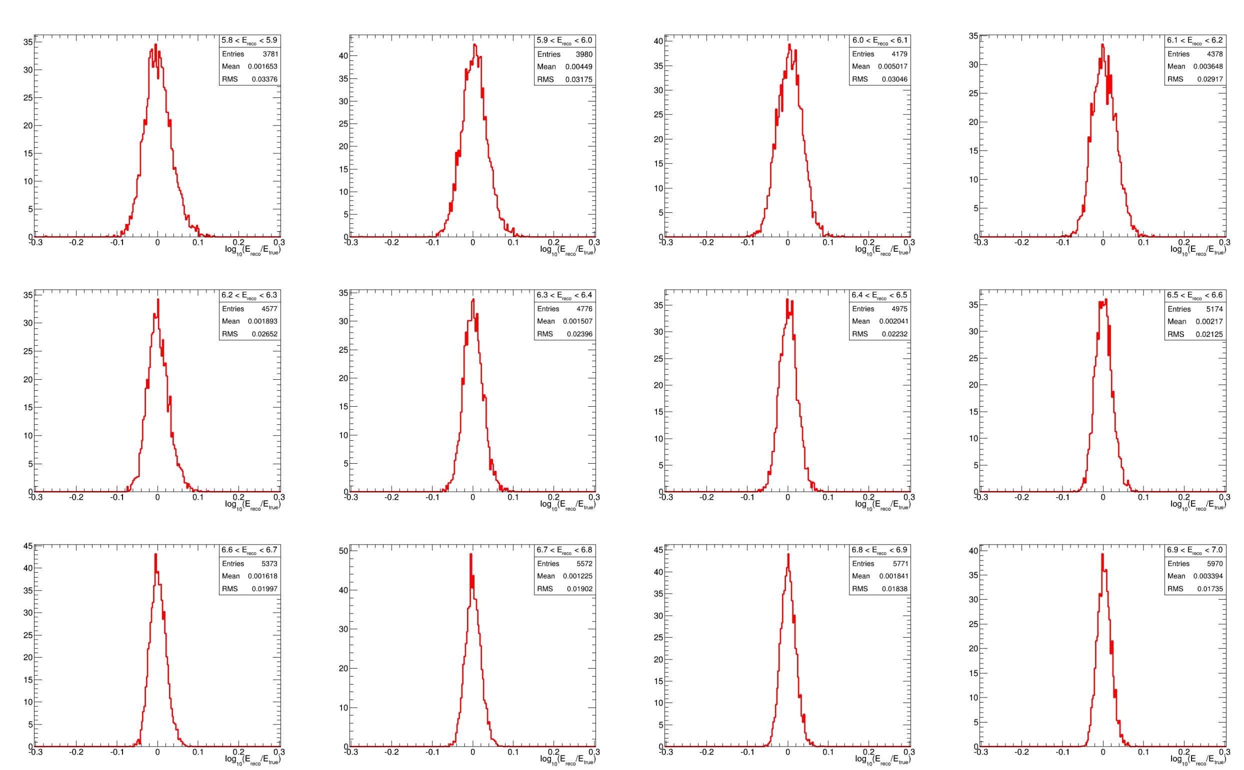

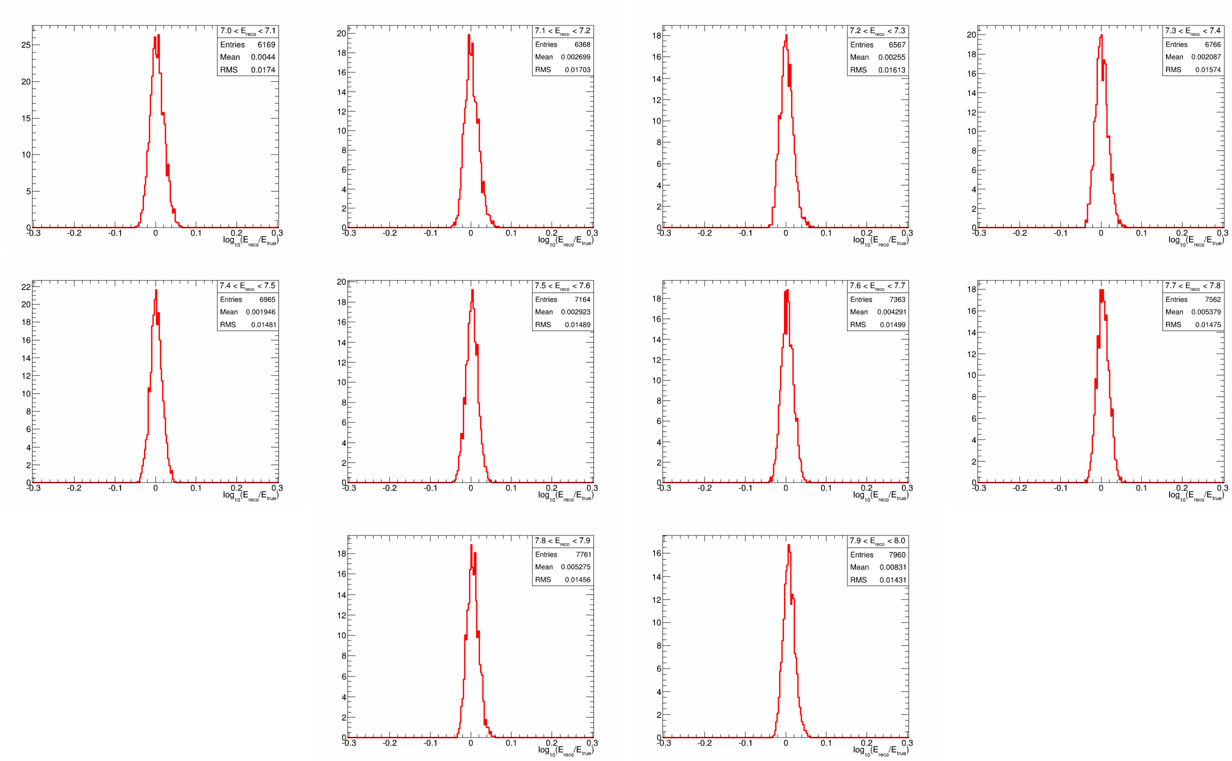

Figure C.3: Fractional distributions of true and reconstructed energy for iron induced showers with a zenith angle $0.9 < \cos(\theta) \leq 1.0$. The energy bias and resolution are considered as the mean and RMS of these distributions, respectively.

C.2.2 Second Zenith Band ($0.8 < \cos(\theta) \leq 0.9$):

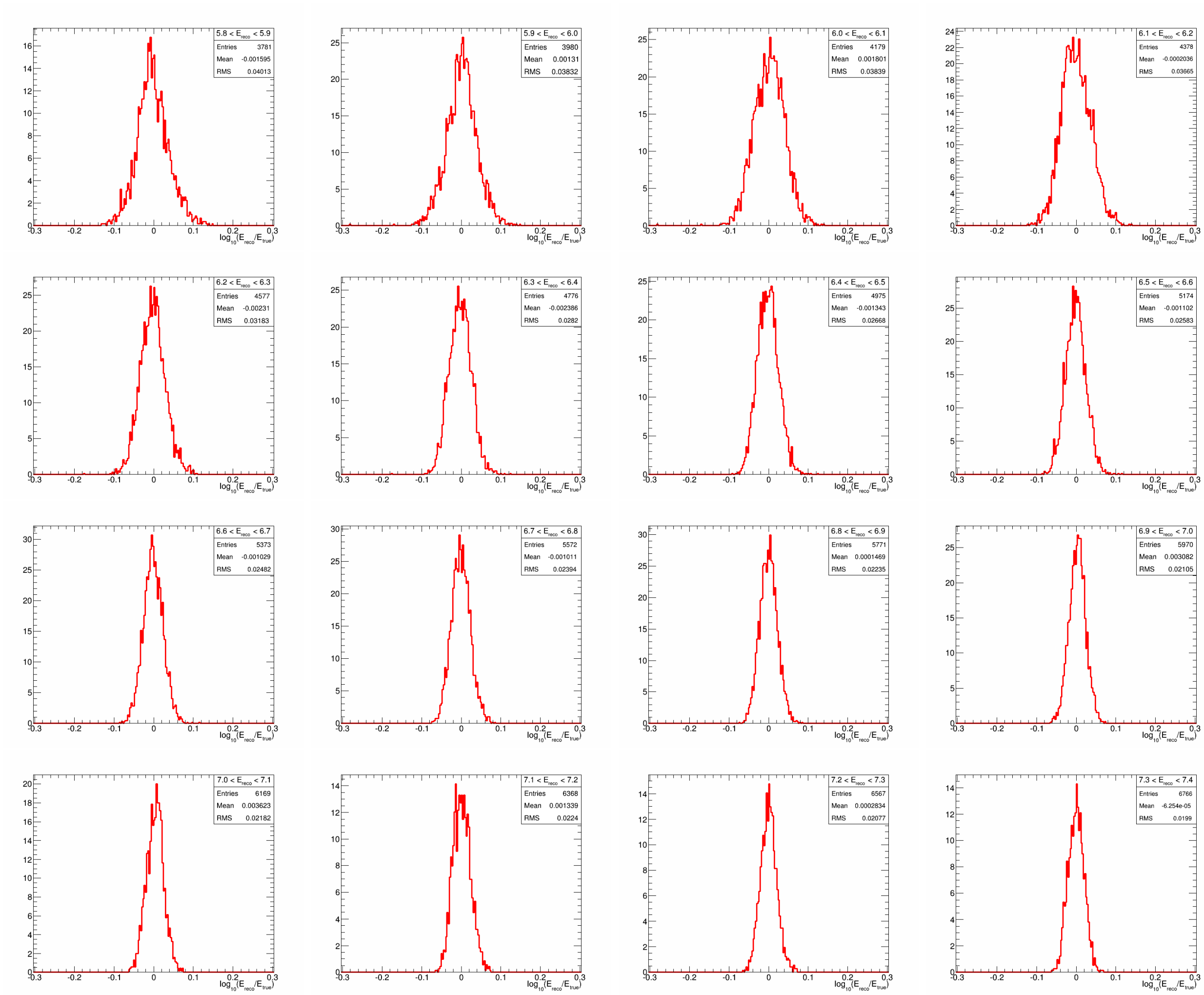

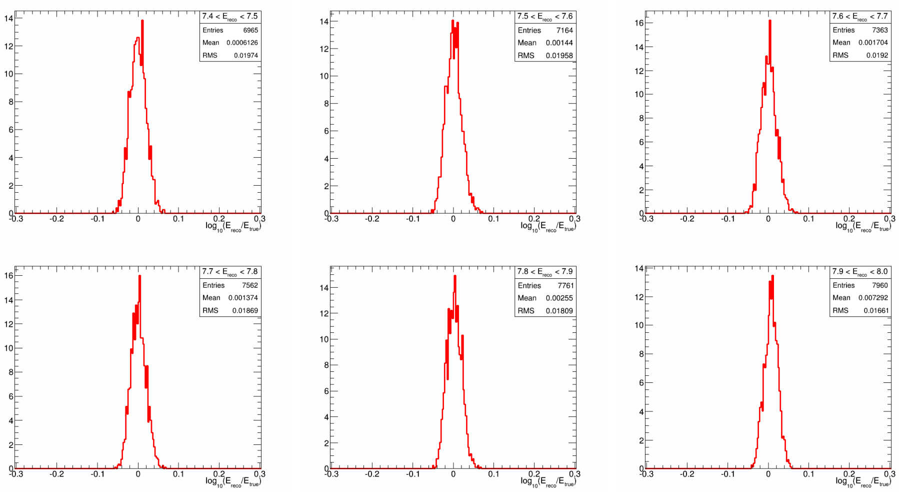

Figure C.4: Fractional distributions of true and reconstructed energy for iron induced showers with a zenith angle $0.8 < \cos(\theta) \leq 0.9$. The energy bias and resolution are considered as the mean and RMS of these distributions, respectively.

Appendix D

Livetime

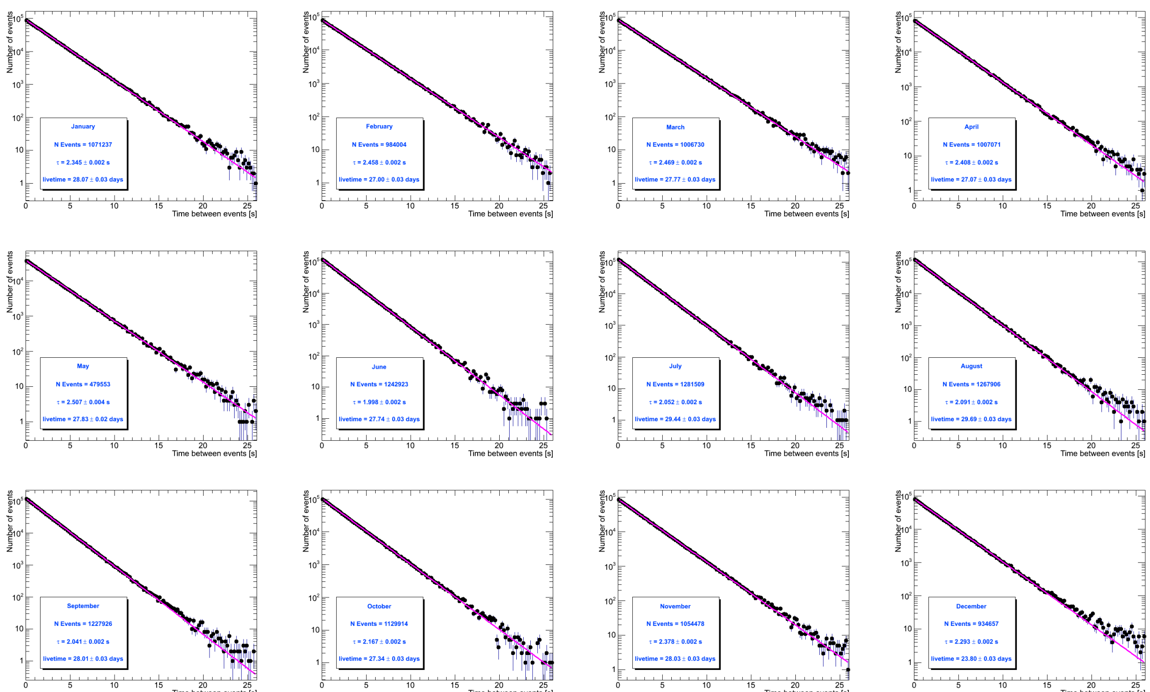

Figure D.1: The livetime of the detector for the selected data taking period for the analysis. The livetime is by multiplying the number of events with the exponential decay constant obtained from Equation 6.2. The livetime is shown month by month.

Appendix E

The Energy Spectrum

The measured cosmic ray flux as a function of energy for air showers with a zenith angle $\theta < 37^\circ$ with pure proton assumption (in Table E.1) and with pure iron assumption (in Table E.2). Systematic uncertainties and statistical errors are also included.

$\log_{10}$(Energy/GeV)	Flux ($\mathrm{m^2 s^{-1} sr^{-1} GeV^{-}1}$)	Stat. Uncertainties	Sys. Uncertainties (+)	Sys. Uncertainties (-)
$5.8 - 5.9$	$5.97498 \cdot 10^{-12}$	$4.53468 \cdot 10^{-14}$	$3.74956 \cdot 10^{-13}$	$3.33605 \cdot 10^{-13}$
$5.9 - 6.0$	$3.53350 \cdot 10^{-12}$	$2.68373 \cdot 10^{-14}$	$2.33447 \cdot 10^{-13}$	$2.11458 \cdot 10^{-13}$
$6.0 - 6.1$	$1.97101 \cdot 10^{-12}$	$1.49885 \cdot 10^{-14}$	$1.40919 \cdot 10^{-13}$	$1.35413 \cdot 10^{-13}$
$6.1 - 6.2$	$1.04819 \cdot 10^{-12}$	$7.98493 \cdot 10^{-15}$	$7.88631 \cdot 10^{-14}$	$7.91313 \cdot 10^{-14}$
$6.2 - 6.3$	$5.54126 \cdot 10^{-13}$	$4.23057 \cdot 10^{-15}$	$4.23101 \cdot 10^{-14}$	$4.32725 \cdot 10^{-14}$
$6.3 - 6.4$	$2.94703 \cdot 10^{-13}$	$2.25598 \cdot 10^{-15}$	$2.27919 \cdot 10^{-14}$	$2.35940 \cdot 10^{-14}$
$6.4 - 6.5$	$1.56904 \cdot 10^{-13}$	$1.20503 \cdot 10^{-15}$	$1.22198 \cdot 10^{-14}$	$1.24781 \cdot 10^{-14}$
$6.5 - 6.6$	$8.28278 \cdot 10^{-14}$	$6.38711 \cdot 10^{-16}$	$6.40773 \cdot 10^{-15}$	$6.73497 \cdot 10^{-15}$
$6.6 - 6.7$	$4.31609 \cdot 10^{-14}$	$3.34540 \cdot 10^{-16}$	$3.39602 \cdot 10^{-15}$	$3.61376 \cdot 10^{-15}$
$6.7 - 6.8$	$2.21727 \cdot 10^{-14}$	$1.72988 \cdot 10^{-16}$	$1.83651 \cdot 10^{-15}$	$1.89678 \cdot 10^{-15}$
$6.8 - 6.9$	$1.11516 \cdot 10^{-14}$	$8.77463 \cdot 10^{-17}$	$9.32987 \cdot 10^{-16}$	$9.78502 \cdot 10^{-16}$
$6.9 - 7.0$	$5.49844 \cdot 10^{-15}$	$4.37476 \cdot 10^{-17}$	$4.61141 \cdot 10^{-16}$	$5.21082 \cdot 10^{-16}$
$7.0 - 7.1$	$2.71485 \cdot 10^{-15}$	$2.19021 \cdot 10^{-17}$	$2.43024 \cdot 10^{-16}$	$2.43238 \cdot 10^{-16}$
$7.1 - 7.2$	$1.30921 \cdot 10^{-15}$	$1.07570 \cdot 10^{-17}$	$9.99257 \cdot 10^{-17}$	$1.24339 \cdot 10^{-16}$
$7.2 - 7.3$	$6.09300 \cdot 10^{-16}$	$5.10744 \cdot 10^{-18}$	$5.36066 \cdot 10^{-17}$	$5.16127 \cdot 10^{-17}$
$7.3 - 7.4$	$3.11783 \cdot 10^{-16}$	$2.67973 \cdot 10^{-18}$	$2.53753 \cdot 10^{-17}$	$2.70445 \cdot 10^{-17}$
$7.4 - 7.5$	$1.61922 \cdot 10^{-16}$	$1.43204 \cdot 10^{-18}$	$1.31855 \cdot 10^{-17}$	$1.50253 \cdot 10^{-17}$
$7.5 - 7.6$	$8.32535 \cdot 10^{-17}$	$7.62630 \cdot 10^{-19}$	$6.93605 \cdot 10^{-18}$	$7.32656 \cdot 10^{-18}$
$7.6 - 7.7$	$4.05406 \cdot 10^{-17}$	$3.86299 \cdot 10^{-19}$	$3.40952 \cdot 10^{-18}$	$3.24155 \cdot 10^{-18}$
$7.7 - 7.8$	$1.99664 \cdot 10^{-17}$	$2.00366 \cdot 10^{-19}$	$1.53970 \cdot 10^{-18}$	$1.92585 \cdot 10^{-18}$
$7.8 - 7.9$	$1.11679 \cdot 10^{-17}$	$1.17409 \cdot 10^{-19}$	$7.64493 \cdot 10^{-19}$	$8.42690 \cdot 10^{-19}$
$7.9 - 8.0$	$5.75480 \cdot 10^{-18}$	$6.46306 \cdot 10^{-20}$	$7.01596 \cdot 10^{-19}$	$5.35943 \cdot 10^{-19}$

Table E.1: Results of the IceTop 81 data with proton assumption.

$\log_{10}$(Energy/GeV)	Flux ($\mathrm{m^2 s^{-1} sr^{-1} GeV^{-}1}$)	Stat. Uncertainties	Sys. Uncertainties (+)	Sys. Uncertainties (-)
$6.0 - 6.1$	$3.74716 \cdot 10^{-12}$	$2.64838 \cdot 10^{-14}$	$2.39457 \cdot 10^{-13}$	$2.14481 \cdot 10^{-13}$
$6.1 - 6.2$	$2.03809 \cdot 10^{-12}$	$1.44216 \cdot 10^{-14}$	$1.40537 \cdot 10^{-13}$	$1.31555 \cdot 10^{-13}$
$6.2 - 6.3$	$1.04144 \cdot 10^{-12}$	$7.38282 \cdot 10^{-15}$	$7.69926 \cdot 10^{-14}$	$7.65030 \cdot 10^{-14}$
$6.3 - 6.4$	$5.20114 \cdot 10^{-13}$	$3.69624 \cdot 10^{-15}$	$3.97858 \cdot 10^{-14}$	$4.05975 \cdot 10^{-14}$
$6.4 - 6.5$	$2.61961 \cdot 10^{-13}$	$1.86738 \cdot 10^{-15}$	$2.02583 \cdot 10^{-14}$	$2.07718 \cdot 10^{-14}$
$6.5 - 6.6$	$1.32007 \cdot 10^{-13}$	$9.44637 \cdot 10^{-16}$	$1.02613 \cdot 10^{-14}$	$1.06926 \cdot 10^{-14}$
$6.6 - 6.7$	$6.64694 \cdot 10^{-14}$	$4.77951 \cdot 10^{-16}$	$5.22968 \cdot 10^{-15}$	$5.34987 \cdot 10^{-15}$
$6.7 - 6.8$	$3.29040 \cdot 10^{-14}$	$2.38089 \cdot 10^{-16}$	$2.63081 \cdot 10^{-15}$	$2.83420 \cdot 10^{-15}$
$6.8 - 6.9$	$1.60606 \cdot 10^{-14}$	$1.17165 \cdot 10^{-16}$	$1.31559 \cdot 10^{-15}$	$1.38182 \cdot 10^{-15}$
$6.9 - 7.0$	$7.65759 \cdot 10^{-15}$	$5.64749 \cdot 10^{-17}$	$6.53304 \cdot 10^{-16}$	$7.01011 \cdot 10^{-16}$
$7.0 - 7.1$	$3.61519 \cdot 10^{-15}$	$2.70427 \cdot 10^{-17}$	$3.02225 \cdot 10^{-16}$	$3.36798 \cdot 10^{-16}$
$7.1 - 7.2$	$1.70379 \cdot 10^{-15}$	$1.29785 \cdot 10^{-17}$	$1.46368 \cdot 10^{-16}$	$1.58823 \cdot 10^{-16}$
$7.2 - 7.3$	$7.47047 \cdot 10^{-16}$	$5.81717 \cdot 10^{-18}$	$6.20641 \cdot 10^{-17}$	$6.59827 \cdot 10^{-17}$
$7.3 - 7.4$	$3.71979 \cdot 10^{-16}$	$2.97350 \cdot 10^{-18}$	$3.04260 \cdot 10^{-17}$	$3.17421 \cdot 10^{-17}$
$7.4 - 7.5$	$1.86657 \cdot 10^{-16}$	$1.53898 \cdot 10^{-18}$	$1.64014 \cdot 10^{-17}$	$1.77634 \cdot 10^{-17}$
$7.5 - 7.6$	$9.45478 \cdot 10^{-17}$	$8.08746 \cdot 10^{-19}$	$7.57468 \cdot 10^{-18}$	$7.76908 \cdot 10^{-18}$
$7.6 - 7.7$	$4.50514 \cdot 10^{-17}$	$4.02012 \cdot 10^{-19}$	$3.53943 \cdot 10^{-18}$	$4.34545 \cdot 10^{-18}$
$7.7 - 7.8$	$2.17480 \cdot 10^{-17}$	$2.05139 \cdot 10^{-19}$	$1.65506 \cdot 10^{-18}$	$1.68467 \cdot 10^{-18}$
$7.8 - 7.9$	$1.18885 \cdot 10^{-17}$	$1.18030 \cdot 10^{-19}$	$1.05005 \cdot 10^{-18}$	$9.20934 \cdot 10^{-19}$
$7.9 - 8.0$	$6.04282 \cdot 10^{-18}$	$6.43874 \cdot 10^{-20}$	$4.46466 \cdot 10^{-19}$	$5.52271 \cdot 10^{-19}$

Table E.2: Results of the IceTop 81 data with iron assumption.

Glossary

- **CMB**: Cosmic Microwave Background.
- **ISM**: Interstellar Matter.
- **QCD**: Quantum Chromodynamics.
- **SNR**: Supernova Remnant.
- **GCR**: Galactic Cosmic Rays.
- **AGN**: Active Galactic Nuclei.
- **GRB**: Gamma Ray Burst.
- **UHECRs**: Ultra High Energy Cosmci Rays.
- **EAS**: Extensive Air Showers.
- **EM**: Electromagnetic.
- **UV**: Ultra Violet.
- **DOM**: Digital Optical Module.
- **HG**: High Gain.
- **LG**: Low Gain.

- **HV**: High Voltage.
- **PE**: Photo-electron.
- **PMT**: Photomultiplier Tube.
- **ICL**: IceCube Laboratory.
- **FADC**: Fast Analog to Digital Converter.
- **FCU**: Freeze Control Unit.
- **FPGA**: Field Programmable Gate Array.
- **LED**: Light Emitting Diode.
- **MPE**: Multiple Photo electron.
- **SPE**: Single Photo electron.
- **ATWD**: Analog Transient Waveform Digitizer.
- **VEM**: Vertical Equivalent Muon.
- **AMRC**: Antarctic Meteorological Research Center.
- **COG**: Center of Gravity.
- **DLP**: Double Logarithmic Parabola.
- **LDF**: Lateral Distribution Function.
- **LHC**: Large Hadron Collider.
- **MB**: Main Board.
- **TA**: Telescope Array.

- **HLC**: Hard Local Coincidence.
- **SLC**: Soft Local Coincidence.
- **VEMCal**: VEM Calibration.
- **MC**: Monte Carlo.
- **CORSIKA**: Cosmic Ray Simulation for KASKADE.
- **GRT**: Gribov's Reggeon Field Theory.
- **NN**: Artificial Neural Network.
- **IT26**: 26 IceTop stations
- **IC40**: 40 IceTop stations and 40 IceCube strings
- **IT73**: 73 IceTop stations
- **IT73-IC79**: 73 IceTop stations and 79 IceCube strings

Samenvatting

Kosmische straling zijn hoog-energische subatomaire deeltjes die bijna tegen de licht snelheid kunnen reizen. Ze komen uit de ruimte en bombarderen de aarde van uit alle richtingen. Ze bestaan hoofdzakelijk uit 86% waterstof kernen, 11% helium 2% zwaardere kernen en 1% electronen.

Kosmische straling is ontdekt in 1912 door een Oostenrijkse fysicus genaamd Victor Hess. Hoewel dat de ontdekking van de kosmische straling meer dan eeuw geleden was, zijn veel fundamentele vragen over hun oorsprong, voortplanting and versnellingsmechanismen in het universum nog niet beantwoord. De kosmische straling met energieen van minder dan 10^{14} eV kunnen bestudeerd worden met directe observaties, door middel van satellieten en ballon experimenten. De intensiteit van kosmische straling vermindert sterk met de energie van het primaire deeltje en dus wordt het heel moeilijk om kosmische straling met een hogere energie direct te detecteren. Daarom wordt kosmische straling met een energie meer dan 10^{14} eV indirect gedetecteerd. Dit door het detecteren van de, deelteslawines of ”Extinsive Air Showers (EAS)” gecreëerd door de interactie van de kosmische straling met luchtmoleculen, op het aardoppervlak.

In Hoofdstuk 1 werd een overzicht over de gescheidenis van kosmische straling sinds hun ontdekking gegeven. De fysica achter de kosmische straling, tezamen met de gerelateerde vragen over de oorsprong, voortplanting en versnellingsmechanisme,n werd besproken. Verder werden ook de EAS geintroduceerd en hun detectiemethoden besproken.

Het IceCube Neutrino Observatorium werd in detail beschreven in Hoofdstuk 2. Een beschrijving van de verschilende componenten van de detector, de plaatsing, de data acquisitie en de doelen werd gegeven. We focussen hierbij in detail op IceTop, de detectiemodules op het oppervlak, aangezien enkel IceTop gebruikt werd in dit werk.

Hoofdstuk 3 beschreef de Monte Carlo simulatie die in de analyse gebruikt werd. De simulatie speelt een belangrijke rol bij de meting van het energiespectrum van kosmische straling. Gedetailleerde informatie over de simulatie van deze EAS in de atmosfeer en de detector simulatie werd in dit hoofdstuk besproken.

Hoofdstuk 4 behandelde de reconstructie procedure voor de simulatie en de gemeten data. Dit reconstructie proces werd toegepast om de belangrijkste observabelen gemeten door IceTop te kunnen reconstructueren: de positie, de richting en de groote van de EAS.

Na de reconstructie van de EAS, werd de selectie van evenementen (één evenement is één EAS) beschreven in hoofdstuk 5. De methode die in de analyse gebruikt werd om de energie van het primaire kosmische stralingdeeltje te bepalen, de efficientie en de kwaliteit werd ook in dit hoofdstuk besproken (Hoofdstuk 5).

De eindresultaten voor de meting van het energie spectrum van kosmische straling werd gepresenteerd en besproken in Hoofdstuk 6.

Uiteindelijk vergeleken we het in dit proefschrift gemeten energie spectrum met andere analyses door middel van de IceTop detector, alsook met gemeten energie spectra door andere experimenten. Een samenvatting en conclusie werd ook getrokken aan het eind van dit proefschrift, tezamen met enkele ideeen voor de toekomst (Hoofdstuk 7).

List of Figures

List of Tables

Bibliography

[1] M. S. Longair. High Energy Cosmic Astrophysics. *Cambridge University Press*, 1992.

[2] P. Auger. Extensive Aire Showers. *Rev. Mod. Phys.*, 11:288–291, 1939.

[3] E. S. Seo. Direct measurements of cosmic rays using balloon borne experiments. *Atropart. Phys*, 39 - 40:76 – 87, 2012.

[4] G. Kulikov and G. Kristiansen. On the size spectrum of extensive air showers. *Exp. Theor. Phys.*, 8:441–444, 1959.

[5] M. Boezio and E. Mocchiutti. Chemical composition of galactic cosmic rays with space experiments. *Atropart. Phys.*, 39 - 40:95 – 108, 2012.

[6] J. R. Horandel. Models of the knee in the energy spectrum of cosmic rays. *Atropart. Phys*, 21:241 – 265, 2004.

[7] T. Abo-Zayyad et al. Measurement of the cosmic ray energy spectrum and composition from 10^{17} eV to $10^{18.3}$ eV using a hybrid fluorescence technique. *Astrophys. J*, 557:686–699, 2001.

[8] M. Ave et al. Mass composition of cosmic rays in the range $2 \times 10^{17} - 3 \times 1018$ eV measured with the Haverah Park array. *Astropart. Phys.*, 19:61–75, 2003.

[9] A. P. Knurenko et al. Characteristics of EAS and primary particle mass composition in the

energy region of $10^{17} - 3 \times 10^{19}$ eV by Yakutsk data. *Nuc. Phys. Proc. Suppl*, 151:92–95, 2006.

[10] M. Takeda et al. Energy determination in the Akeno Giant Air Shower Array experiment. *Astropart. Phys.*, 19:447–463, 2003.

[11] M. Nagano et al. Energy spectrum of primary cosmic rays above 10^{17} eV determined from the extensive air shower experiment at Akeno. *J. Phys.*, G18:423–442, 1992.

[12] J. Linsley. Volcano Ranch Evidence on The Cosmic Ray Energy Spectrum: A Preliminary Re-evaluation. In *Proc., 13th ICRC*, volume 5, pages 3207–3211. Denver, Colorado, 1973.

[13] A. Aloisio, V. Berezinsky, and A. Gazizov. Transition from galactic to extragalactic cosmic rays. *AstroPart. Phys.*, 39 - 40:129 – 143, 2012.

[14] P. Abreu et al. The Pierre Auger Observatory: Studies of Cosmic Ray Composition and Hadronic Interaction models. In *Proc., 32th ICRC*. Beijing, China, 2011.

[15] K. Greisen. End to the cosmic ray spectrum? *Phys. Rev. Lett.*, 16:748–750, 1966.

[16] G. T. Zatsepin and V. A. Kuzmin. Upper limit of the spectrum of cosmic rays. *JETP Lett.*, 4:78–80, 1966.

[17] R. U. Abbasi et al. First observation of the Greisen-Zatsepin-Kuzmin suppression. *Phys.Rev.Lett.*, 100:101101, 2008.

[18] J. Abraham et al. Observation of the suppression of the flux of cosmic rays above 4×10^{19}eV. *Phys.Rev.Lett.*, 101:061101, 2008.

[19] D. H. Perkins. Particle Astrophysics. *Oxford University Press*, 2003.

[20] J. Z. Wang, E. S Seo, et al. Measurement of Cosmic Ray Hydrogen and Helium and Their Isotopic Composition with the BESS Experiment. *Astro. phys. J.*, 564:244 – 259, 2002.

[21] E. C. Stone et al. The Solar Isotope Spectrometer for the Advanced Composition Explorer. *Space. Sci. Rev.*, 86:285 – 356, 1998.

[22] W. R. Binns et al. In Cosmic Abundance of Matter. *Amer. Instit. Phys.*, CP183:147 – 167, 1989.

[23] M. E. Weidenbeck, W. R Binns, et al. An Overwiew of the Origin of Galactic Cosmic Rays as Inferred from Observations of Heavy Ion Composition and Spectra. *Space. Sci. Rev.*, 130:415 – 429, 2007.

[24] K. H Kampert and M. Unger. Measurements of the cosmic ray composition with air shower experiments. *Astropart. Phys.*, 35(10):660 – 678, 2012.

[25] A. M. Hillas. The Origin of Ultra High Energy Cosmic Rays. *Annu. Rev. Astr. Astrophy.*, 22:425–444, 1984.

[26] J. M. Santander. *Observation of Cosmic Ray Anisotropy at TeV and PeV Energies in the Southern Sky*. PhD thesis, University of Wisconsin Madison, 2013.

[27] L. O'C. Drury. Origin of cosmic rays. *AstroPart. Phys.*, 39 - 40:52 – 60, 2012.

[28] W. Baade and F. Zwicky. Cosmic Rays and Super-Novae. In *Proceedings of the National Academy of Science*, volume 20, pages 259–263, 1934.

[29] J. Abraham et al. Properties and performance of the prototype instrument for the Pierre Auger Observatory. *Nucl. Instrum. Meth.*, A523:50–95, 2004.

[30] M. P. Veron-Cetty and P. Veron. A catalogue of quasars and active nuclei: 12th edition. *A. A*, 455:773–777, 2006.

[31] J. Abraham et al. Correlation of the Highest-Energy Cosmic Rays with Nearby Extragalactic Objects. *Science*, 318:938–943, 2007.

[32] P. W. Klebesadel, I. P. Strong, and R. A. Olson. Observations of Gamma-Ray Bursts of Cosmic Origin. *Astrophys. J.*, 182:85–88, 1973.

[33] R. Abbasi et al. An absence of neutrinos associated with cosmic ray acceleration in gamma ray bursts. *Nature*, 484:351–354, 2012.

[34] X ray: NASA/CXC/ASU/J. Hester et al.

[35] Optical: NASA/STScI.

[36] Infrared: NASA/JPL-Caltech/Steward/O. Krause et al.

[37] R. X-Ray: NASA/CXC/CfA/Kraft et al.

[38] A. Submillimeter: MPIfR/ESO/APEX/Weiss et al.

[39] E. Fermi. On the Origin of the Cosmic Radiation. *Phys. Rev.*, 75:1169–1174, 1949.

[40] T. K. Gaisser. Cosmic rays and particle physics. *Cambridge University Press*, 1990.

[41] P. O. Lagage and C. J. Cesarsky. The maximum energy of cosmic rays accelerated by supernova shocks. *Astron. Astrophys.*, 125:249–257, 1983.

[42] A. W. Strong, I. V. Moskalenko, and Vladimir S. Ptuskin. Cosmic-Ray Propagation and Interactions in the Galaxy. *Annual Review of Nuclear and Particle Science*, 57(1):285–327, 2007.

[43] H. Rebel and O. Sima. Information about high-energy hadronic interaction processes from extensive air shower observations. *Rom. J. Phys.*, 57:472–492, 2012.

[44] J. Matthews. A Heitler model of extensive air showers. *Astropart. Phys.*, 22:387 – 397, 2005.

[45] T. Stanev. High energy cosmic rays. *Springer-Praxis*, 2004.

[46] T. Feusels. *Measurement of cosmic ray composition and energy spectrum between 1 PeV and 1 EeV with IceTop and IceCube*. PhD thesis, Gent University, 2013.

[47] K. Andeen. *First Measurements of Cosmic Ray Composition from 1 - 50 PeV using New Techniques on Coincident Data from the IceCube Neutrino Observatory*. PhD thesis, University of Wisconsin Madison, 2011.

[48] P. K. F Grieder. Extensive Air Showers. *Springer-Praxis*, 2004.

[49] N. M. Budnev, D. V. Chernov, O. A. Gress, N. N. Kalmykov, V. A. Kozhin, et al. The tunka experiment: towards a 1-km^2 eas Cerenkov light array in the tunka valley. In *Proc. 29th ICRC*. Pune, Italy, 2005.

[50] A. N. Bunner. *Cosmic Ray Detection by Atmospheric Fluoresence*. PhD thesis, Cornell University, 1967.

[51] H. Kawai et al. Telescope Array Experiment. *Nucl. Phys. B. Procc. Supp*, 175 - 176(0):221 – 226, 2008. Proceedings of the {XIV} International Symposium on Very High Energy Cosmic Ray Interactions.

[52] J. Maller. Radio detection of extensive air showers at the Pierre Auger Observatory. *Nucl. Instrum. Meth.*, 742(0):232 – 236, 2014.

[53] J. Auffenberg, D. Besson, T. Gaisser, K Helbing, T Karg, and A Karle. A radio air shower detector as an extension for IceCube and IceTop. *Nucl. Instrum. Meth.*, 604:S53 – S56, 2009.

[54] R. Abbasi et al. IceTop: The surface component of IceCube. *Nucl. Instrum. Meth.*, A700:188–220, 2013.

[55] T. Antoni et al. The Cosmic ray experiment KASCADE. *Nucl. Instrum. Meth.*, A513:490–510, 2003.

[56] D. Heck et al. www-ik.fzk.de/corsika/physics_description/corsika_phys.html.

[57] E. S. Seo et al. Cosmic Ray Energetics And Mass for the International Space Station (ISS-CREAM). *Advances in Space Research*, 53:1451 – 1455, 2014.

[58] Y. S. Yoon et al. Cosmic Ray Proton and Helium Spectra from the First CREAM Flight. *Astrophysical Journal*, 728:122, 2011.

[59] G. Navarra et al. KASCADE-Grande: a large acceptance, high-resolution cosmic-ray detector up to 10^{18} eV. *Nucl. Instrum. Meth.*, 518:207–209, 2004.

[60] G. Rodriguez. Measurement of the ultra high energy cosmic ray energy spectrum with the Pierre Auger Observatory. *Nucl.Instrum.Meth.*, A742:261–264, 2014.

[61] J. R. T. de Mello Neto. Measurements of cosmic rays at the highest energies with the Pierre Auger Observatory. *Advances in Space Research*, 53:1476 – 1482, 2014.

[62] A. Achterberg et al. First Year Performance of the IceCube Neutrino Telescope. *Astropart. Phys.*, 26:155–173, 2006.

[63] J. Ahrens et al. IceCube Preliminary Design Document. *Rev 1.24*, Oct.11 2001. http://www.icecube.wisc.edu/science/publications/pdd/pdd.pdf.

[64] R. Abbasi et al. The Design and Performance of IceCube DeepCore. *Astropart. Phys.*, 35, 2013.

[65] R. Abbasi et al. The IceCube Data Acquisition System: Signal Capture, Digitization, and Timestamping. *Nucl. Instrum. Meth.*, A601:294–316, 2009.

[66] R. Abbasi et al. First Observation of PeV-Energy Neutrinos With IceCube. *Phys.Rev.Lett.*, 111:615–624, 2012.

[67] M. A. Lawrence, R. J. O. Reid, and A. A. Watson. The Cosmic ray energy spectrum above 4 $\times$ 10^{17}eV as measured by the Haverah Park array. *J. Phys.*, 17:733–757, 1991.

[68] R. Abbasi et al. Calibration and Characterization of the IceCube Photomultiplier Tube. *Nucl. Instrum. Meth.*, A618(1-3):139–152, 2010.

[69] T. Waldenmaier. IceTop configuration. *IceCube Internal Report*, 2010. `https://wiki.icecube.wisc.edu/index.php/IceTop_Configurations`.

[70] R. Brun and F. Rademakers. ROOT - An Object Oriented Data Analysis Framework. *Nucl. Instrum. Meth.*, A389:81–86, 1997.

[71] L. Dimirors et al for the IceCube Collaboration. IceTop tank response to muons. In *Proc. 30rd ICRC*, volume 5, pages 1261–1264. Merida, Mexico, 2007.

[72] R. Abbasi et al. Solar energetic particle spectrum on 2006 December 13 determined by IceTop. *Astrophysical Journal Letters*, 689:L65–L68, 2008.

[73] J. Auffenberg et al. IceTop as a veto in astrophysical neutrino searches for IceCube. In *Proc. 33rd ICRC*. Rio De Janeiro, Brazil, 2013.

[74] R. Abbasi et al. Lateral distribution of muons in IceCube cosmic ray events. *Phys.Rev.D.*, 87, 2013.

[75] D. Soldin. Composition from high p_T muons in IceCube. In *Proc., 18thISVHECRI*. CERN, 2014.

[76] S. De Ridder. Influence of South Pole atmosphere on cosmic rays observed by IceCube. Master's thesis, Gent University, 2012.

[77] AMRC and AWS. The Antarctic Meteorological Research Center (AMRC) and Automatic

Weather Station Project (AWS). ftp://amrc.ssec.wisc.edu/pub/southpole/surface_observations/.

[78] E. Ahn, R. Engel, T. Gaisser, P. Lipari, and T. Stanev. Cosmic ray interaction event generator SIBYLL 2.1. *Phys. Rev. D*, 80:094003, 2009.

[79] G. Battistoni et al. The FLUKA code: Description and benchmarking. *AIP Conference Proceeding*, 896:31–49, 2007.

[80] W. R. Nelson, H. Hirayama, and D. W. O. Rogers. The EGS4 Code System. *Technical Report*, SLAC 265, 1985. Stanford Linear Accelerator Center, http://www.slac.stanford.edu/pubs/slacreports/slac-r-265.html.

[81] D. Heck and J. Knapp. Upgrade of the Monte Carlo Code CORSIKA to Simulate Extensive Air Showers with Energies $> 10^{20}$ eV. *FZKA 6097*, 1998. http://www-ik.fzk.de/~heck/publications.

[82] E. Hedin. Extension of the MSIS Thermosphere Model into the Middle and Lower Atmosphere. *Journal of Geophysical Research-Space Physics*, A2:1159–1172, 1991.

[83] D. Heck, J. Knapp, J. N. Capdevielle, G. Schatz, and T. Thouw. CORSIKA, A Monte Carlo Code to Simulate Extensive Air Showers. *FZKA 6019*, 1998. http://www-ik.fzk.de/~heck/publications.

[84] The Large Hadron Collider. http://home.web.cern.ch/topics/large-hadron-collider.

[85] A. Capella, U. Sukhatme, C. Tan, and J. Tran Thanh Van. Dual Parton Model. *Phys. Rep*, 236:225–329, 1994.

[86] T. Sjostrand. Status of Fragmentation Models. *Mod. Phys*, 3:751–823, 1988.

[87] T. Gaisser and F. Halzen. ”Soft” Hard Scattering in the Teraelectronvolt Range. *Phys. Rev. Lett*, 54:1754–1756, 1985.

[88] S. Ostapchenko. Studies of Very High Energy Cosmic Rays: Status, Puzzles, and the Impact of LHC Data. *Progr. Theor. Phys. Suppl.*, 193:204–211, 2012.

[89] V. N. Gribov. A Reggeon Diagram Technique. *Sov. Phys., JETP*, 26(2):414–423, 1968.

[90] K. Warner. Strings, Pomerons and the VENUS Model of Hadronic-Interactions at Ultrarelavistic Energies. *Phys. Rep*, 232:87–299, 1993.

[91] H. J. Drescher. Parton-based Gribov-Regge theory. *Phys. Rep*, 350:2–4, 2001.

[92] K. Werner, F.-M. Liu, and T. Pierog. Parton ladder splitting and the rapidity dependence of transverse momentum spectra in deuteron-gold collisions at the BNL Relativistic Heavy Ion Collider. *Phys. Rev. C*, 74:044902, 2006.

[93] S. Agostinelli et al. GEANT4 — a simulation toolkit. *Nucl. Instrum. Meth.*, 506:250–303, 2003.

[94] C. Roucelle. DOMSimulator user guide for IceSim release V02-00-00 and more. *IceCube Internal Report*, 2007. `http://internal.icecube.wisc.edu/reports/data/icecube/2007/09/002/icecube_200709002_v2.pdf`.

[95] F. Kislat, S. Klepser, and A. Van Overloop. A Lateral Distribution Function and Fluctuation Parametrisation for IceTop. *IceCube Internal Report*, 2007. `http://internal.icecube.wisc.edu/reports/data/icecube/2007/02/001/icecube_200702001_v6.pdf`.

[96] J. Gonzalez et al. Inclined Cosmic Ray Air Showers in IceCube. In *Proc. 33rd ICRC*. Rio De Janeiro, Brazil, 2013.

[97] R. Abbasi et al. All-particle cosmic ray energy spectrum measured with 26 IceTop stations. *Astropart. Phys.*, 44:40–58, 2013.

[98] F. Kislat. *Measurement of the Energy Spectrum of Cosmic Rays with the 26 Station Configuration of the IceTop Detector*. PhD thesis, Berlin University, 2011.

[99] M. G. Aartsen et al. Measurement of the cosmic ray energy spectrum with IceTop-73. *Phys. Rev. D*, 88:042004, 2013.

[100] K. Rawlins et al. The Effect of Snow Accumulation on Signals in IceTop. In *Proc. 33rd ICRC*. Rio De Janeiro, Brazil, 2013.

[101] A. Haj Ismail et al. Low Energy Air Showers With IceTop. In *Proc. 33rd ICRC*. Rio De Janeiro, Brazil, 2013.

[102] A. Van Overloop et al. Simulation of IceTop VEM calibration and the dependency on the snow layer. In *Proc. 32nd ICRC*. Beijing, China, 2011.

[103] F. Klepser. *Reconstruction of Extensive Air Showers and Measurement of the Cosmic Ray Energy Spectrum in the Range of 1 - 80 PeV at the South Pole*. PhD thesis, Berlin University, 2008.

[104] R. Abbasi et al. Cosmic ray composition and energy spectrum from 1-30 PeV using the 40-string configuration of IceTop and IceCube. *Astropart. Phys.*, 42:15–32, 2013.

[105] G. Gonzalez. Cosmic Ray Energy Spectrum and Composition from IceCube. *UHECR*, 2014. `http://uhecr2014.telescopearray.org/gonzalez/gonzalez_IceTop_spectrum.pdf`.

[106] T. K. Gaisser. Spectrum of cosmic ray nucleons, kaon production, and the atmospheric muon charge ratio. *Astropart. Phys.*, 35:801–806, 2012.

[107] M. Amenomori et al. The All-Particle Spectrum of Primary Cosmic Rays in the Wide Energy Range from 10^14 to 10^17 eV Observed with the Tibet-III Air-Shower Array. *Astrophys. J.*, 678:1165–1179, 2008.

[108] A. P. Garyaka, R. M. Martirosov, S. V. Ter-Antonyan, A. D. Erlykin, N. M. Nikolskaya, Y. A. Gallant, L. W. Jones, and J. Procureur. An all-particle primary energy spectrum in the 3-200 PeV energy range. *J. Phys. G.*, 35:115201, 2008.

[109] W. Apel et al. The KASCADE-Grande energy spectrum of cosmic rays and the role of hadronic interaction models. *Adv. Spa. Res*, 53:1456–1469, 2014.

[110] C. C. Finaly et al. International Geomagnetic Reference Field: the eleventh generation. *Geophysical Journal International*, 183:1216–1230, 2010.